CORROSION FATIGUE CRACK PROPAGATION IN PRESSURE VESSEL STEEL.

ROY DERRICK ACHILLES

A dissertation submitted to the Faculty of Engineering, University of the Witwatersrand, Johannesburg, in fulfilment of the requirements for the degree of Master of Science in Engineering.

Johannesburg 1986

DECLARATION

I declare that this dissertation is my own unaided work, except where due reference is made to others. It is being submitted for the Degree of Master of Science in Engineering at the University of the Witwatersrand Johannesburg. It has not been submitted before for any degree or examination in any other University.

R D A H I L L

ROY DERRICK ACHILL

4 th day of April 1986

ABSTRACT

This dissertation reports on the results of an experimental test programme which investigated the effect of certain start up transients on the rate of fatigue crack propagation in SA508 Grade B Class III RPV steel. These included examining the effects of environment, frequency, waveform and variable amplitude loading at low temperature and pressure. Results indicated a marked frequency effect in simulated Pressurized Water Reactor (PWR) environment at the low frequencies. Positive sawtooth loading produced crack growth rates which were consistently higher than those for sinusoidal loading. Tests conducted using the spectrum loading sequence produced no evidence of retardation or delayed retardation of the fatigue crack growth rate. At low frequencies in a PWR water environment the 0.9 R-ratio component contributed significantly to the crack extension. Fractographic observations agreed well with the observed macrocrack growth behaviour. Hydrogen assisted cracking was shown to be the most acceptable model for explaining both the crack growth behaviour as well as the fractographic observations found in all the tests conducted in this study.

ACKNOWLEDGEMENTS

The experience, enthusiasm and constant help with this project of my supervisor, Dr J H Bulloch, is gratefully acknowledged.

The interest and helpful suggestions of Professor G C Garrett and Dr R B Tait is also gratefully acknowledged.

The assistance of Mr P D Hicks with certain of the experimental details is acknowledged with thanks.

The financial support of the Atomic Energy Commission and the assistance of Dr K Bogie is greatly appreciated.

The assistance of Mike Cottle with the computer programming is acknowledged with thanks.

I also want to thank Lawna Sinnett for her patience in word processing this dissertation.

Finally, I would like to thank my colleagues of the Fracture Group for their encouragement and stimulating discussions.

CONTENTS

		Page
DECLARATION		(ii)
ABSTRACT		(iii)
ACKNOWLEDGEMENTS		(iv)
CONTENTS		(v)
1	INTRODUCTION	1
1.1	**Background and Motivation**	1
1.2	**Objectives**	2
2	LITERATURE REVIEW	4
2.1	**Introduction**	4
2.2	**Factors Affecting the Rate of Fatigue Crack Propagation**	6
2.2.1	Environment	6
2.2.1.1	Anodic Dissolution Mechanism	9
2.2.1.2	Hydrogen Embrittlement Mechanism	11
2.2.2	Frequency	13
2.2.2.1	True Corrosion Fatigue	14
2.2.2.2	Low Stress Intensity Levels	15
2.2.2.3	Stress Corrosion Fatigue	16
2.2.3	Waveform	17
2.2.4	Non-Metallic Inclusions	21
2.3	**Variable Amplitude Loading**	24
2.3.1	Retardation	25
2.3.2	Crack Closure Mechanisms	27
2.3.2.1	Plasticity Induced Crack Closure	27
2.3.2.2	Oxide Induced Crack Closure	28
2.3.2.3	Roughness Induced Crack Closure	29
2.4	**Summary**	30
3	EXPERIMENTAL SYSTEMS	43
3.1	**Testing System**	43
3.1.1	E.S.H. Servo-hydraulic Testing Machine	43

3.1.2	Computer Control	44
3.1.3	Microcomputer Interface Unit	44
3.2	**Environmental Circuit**	48
3.2.1	PWR Water Circuit	48
3.2.2	Water Conditioning	49
3.2.3	Recirculating System	51
3.2.4	Analytical Equipment	51
3.3	**Environmental Cell**	55
3.4	**Crack Length Measurement**	56
3.4.1	Power Supply	57
3.4.2	Recording System	57
3.5	**Argon Environmental System**	58
3.6	**Summary**	61
4	EXPERIMENTAL PROCEDURES	72
4.1	**Material Specification**	72
4.2	**Test Programme**	73
4.3	**Water Chemistry Control**	74
4.4	**Fatigue Testing**	75
4.4.1	Prefatigue Cracking	75
4.4.2	Visual Crack Length Measurement	75
4.4.3	Crack Curvature Correction	76
4.4.4	Calibration of the Potential Drop Technique	76
4.5	**Computer Control and Data Logging**	77
4.6	**Data Reduction Technique**	79
4.7	**Variable Amplitude Loading**	81
4.8	**Argon System**	82
4.9	**Summary**	83
5	RESULTS	90
5.1	**Crack Growth Rate Data**	90
5.1.1	Constant Amplitude	90
5.1.1.1	Environment	90
5.1.1.2	Frequency	91
5.1.1.3	Waveform	92
5.1.1.4	High R-Ratio Tests	93
5.1.2	Variable Amplitude Loading	95

5.1.2.1	3 Hz Argon Tests	95
5.1.2.2	3 Hz PWR Water Tests	95
5.1.2.3	0.3 Hz PWR Water Tests	96
5.2	**Fractography**	96
5.2.1	Constant Amplitude	97
5.2.1.1	10 Hz Tests	97
5.2.1.2	1 Hz Positive Sawtooth Tests	97
5.2.1.3	1 Hz Sine Wave Tests	98
5.2.1.4	0.1 Hz Sine Wave Tests	99
5.2.1.5	High R-Ratio Tests	99
5.2.2	Variable Amplitude Loading	101
5.2.2.1	3 Hz Argon Tests	101
5.2.2.2	3 Hz PWR Water Tests	101
5.2.2.3	0.3 Hz PWR Water Tests	102
6	**DISCUSSION**	158
6.1	**Constant Amplitude**	158
6.1.1	Environment	158
6.1.1.1	Argon Environment	158
6.1.1.2	PWR Water	160
6.1.2	Frequency	163
6.1.3	Waveform	167
6.1.4	High R-Ratio Tests	169
6.2	**Variable Amplitude Loading**	177
6.2.1	Argon Tests	177
6.2.2	PWR Water Tests	180
7	**CONCLUSIONS**	188
7.1	**Constant Amplitude**	188
7.1.1	Environment	188
7.1.2	Frequency	188
7.1.3	Waveform	189
7.1.4	High R-Ratio Tests	190
7.2	**Variable Amplitude Loading**	191
7.2.1	Argon Tests	191
7.2.2	PWR Water Tests	191
7.3	**Mechanisms**	192

5.1.2.1	3 Hz Argon Tests	95
5.1.2.2	3 Hz PWR Water Tests	95
5.1.2.3	0.3 Hz PWR Water Tests	96
5.2	**Fractography**	96
5.2.1	Constant Amplitude	97
5.2.1.1	10 Hz Tests	97
5.2.1.2	1 Hz Positive Sawtooth Tests	97
5.2.1.3	1 Hz Sine Wave Tests	98
5.2.1.4	0.1 Hz Sine Wave Tests	99
5.2.1.5	High R-Ratio Tests	99
5.2.2	Variable Amplitude Loading	101
5.2.2.1	3 Hz Argon Tests	101
5.2.2.2	3 Hz PWR Water Tests	101
5.2.2.3	0.3 Hz PWR Water Tests	102
6	**DISCUSSION**	158
6.1	**Constant Amplitude**	158
6.1.1	Environment	158
6.1.1.1	Argon Environment	158
6.1.1.2	PWR Water	160
6.1.2	Frequency	163
6.1.3	Waveform	167
6.1.4	High R-Ratio Tests	169
6.2	**Variable Amplitude Loading**	177
6.2.1	Argon Tests	177
6.2.2	PWR Water Tests	180
7	**CONCLUSIONS**	188
7.1	**Constant Amplitude**	188
7.1.1	Environment	188
7.1.2	Frequency	188
7.1.3	Waveform	189
7.1.4	High R-Ratio Tests	190
7.2	**Variable Amplitude Loading**	191
7.2.1	Argon Tests	191
7.2.2	PWR Water Tests	191
7.3	**Mechanisms**	192

8 RECOMMENDATIONS 193

REFERENCES 195

APPENDIX 204

1 INTRODUCTION

1.1 Background and Motivation

The safety of nuclear power plants is of paramount importance in the generation of nuclear energy. Recently some unfortunate cases of failure have been experienced, such as Three Mile Island and the discovery, in the Japanese Power Demonstration Reactor, of cracks - some of which penetrated through the liner reaching the base metal. These failures have focussed attention even more acutely on the need for safe operation of nuclear power plants. This safety depends mainly on the integrity of both the reactor pressure vessel and the primary coolant circuit of the reactor system.

During the operation of modern nuclear reactor plants, stringent pressure and temperature limitations for heat up and cool down of the reactor coolant system are imposed to provide adequate safety margins against the possibility of failure of the ferritic pressure vessel materials. Fracture mechanics is the best available science that can quantitatively account for the factors that influence the true factor of safety or degree of reliability of a structure. This is based on the so-called defect tolerant approach, in which the prime consideration in dictating the lifetime of a component is taken as the time or number of cycles required to propagate a subcritical crack from an assumed initial defect size (often taken as the limit of the non-destructive test method used) to the critical size where total failure occurs catastrophically. This approach has been applied in a widely used procedure for the quantitative evaluation of defect growth in both a stable and an unstable manner during service viz., the ASME Boiler and Pressure Vessel Code, Section XI. The ASME-XI standard gives code requirements for in-service inspection, and Appendix A of section XI requires that defects revealed during inspection be evaluated for accident loading conditions as well as for fatigue.

The commencement of power generation at the Koeberg nuclear power plant has necessitated a greater understanding in South Africa of the various factors affecting fatigue crack propagation in reactor pressure vessel steels. This understanding will contribute to both the safe operation and the efficient use of the nuclear power station in that the premature closing down of such an installation for repair can be extremely costly. This thesis reports on the results of an experimental test programme, sponsored by the Atomic Energy Commission, with the aim of investigating the effect of certain start up transients on the rate of fatigue crack propagation in the reactor pressure vessel steel. These include examining some of the effects of environment, frequency, waveform and variable amplitude loading at low temperature and pressure.

1.2 Objectives

The aim of the present study was to develop a testing facility to quantify the rate of corrosion fatigue crack propagation in reactor pressure vessel steels, under specific conditions that simulate reactor start up transients in the low temperature and low pressure regime. This necessitated the development of the following techniques and systems:

(i) the construction of an environmental cell capable of maintaining simulated PWR water at temperatures up to 90°C while simultaneously accommodating fatigue loading of a one inch thick compact tension (1T CT) specimen under leakproof conditions,

(ii) facilities for remote yet reliable and accurate crack length monitoring within such a cell,

(iii) development of a simulated PWR water environment system. (This was done by P Hicks [1]);

(iv) computer control of the mechanical variables in order to run the fatigue tests based on applied load and measured crack length. The computer would thus facilitate test control as well as data logging.

2 LITERATURE REVIEW

2.1 Introduction

During recent years systematic studies of corrosion fatigue crack propagation in steels have led to an improved understanding of the relative effects of those mechanical and environmental variables which control the rate of corrosion fatigue damage. Such an understanding has been developed quantitatively through the use of fracture mechanics.

It is well known that fatigue crack growth itself (i.e. pure mechanical fatigue effects) can be described in fracture mechanics terms since the rate of fatigue crack growth per cycle, da/dN, is uniquely governed by the cyclic range of stress intensity, ΔK, see Ritchie [2] for example. The typical sigmoidal fatigue crack growth behaviour exhibiting essentially three separate regions is illustrated schematically in Figure 2.1 where the principal features are:

(a) the existence of a threshold stress intensity range ΔK_{th}, below which cracks do not measurably propagate during many fatigue cycles, typically 10^7 cycles,

(b) the termination of stable fatigue crack growth when K_{max} in the cycle reaches K_{1c} i.e. the onset of unstable fast fracture,

(c) a substantial region of behaviour between the extremes of (a) and (b) which may be described by the Paris - Erdogan [3] growth law,

$$\frac{da}{dN} = C(\Delta K)^m$$

where C and m are material constants.

The enhancement of fatigue crack growth rate due to the environment has received much attention (see for example the NACE conference on Corrosion Fatigue, 1972). Complex frequency and temperature dependent crack growth behaviour has been found for aqueous environments resulting in changes in both C and m in the Paris-Erdogan equation.

Stress corrosion crack growth in a statically loaded structure is caused by the conjoint action of the chemical and mechanical processes at the crack tip in a susceptible microstructure. The highest stress intensity factor value at which subcritical (stable crack growth before the onset of fast failure) crack growth does not occur in a material loaded statically in an aggressive environment is designated K_{Iscc} which represent a threshold stress intensity value for stress corrosion cracking (SCC). This threshold stress intensity for stress corrosion, K_{Iscc} provides an important separation point between what are now known to be distinctly different forms of corrosion fatigue behaviour [4-8]. It is convenient to refer to these as "True Corrosion Fatigue" and "Stress Corrosion Fatigue" and these may be defined thus:

True Corrosion Fatigue (TCF) : identifies the behaviour where fatigue crack growth rates are enhanced by the presence of an aggressive environment through a synergistic action of corrosion and cyclic loading. This is "below K_{Iscc}" behaviour and applies to materials where the peak crack tip stress intensity K_{max} does not exceed K_{Iscc}.

Stress Corrosion Fatigue (SCF) : describes corrosion under fatigue conditions which occurs whenever the stress intensity in the cycle is above K_{Iscc}; i.e. "above K_{Iscc}" behaviour.

The differences between true corrosion fatigue and fatigue in an inert environment may be characterised by different values of the intercept C and exponent m of the Paris-Erdogan equation. The slope m may be such that the straight line portions of the inert and aggressive curves may converge, diverge or be parallel (Figure 2.2a). Stress corrosion fatigue behaviour for materials

which do not exhibit environmental enhancement until K_{Iscc} is reached is shown in Figure 2.2b. This may be characterised by the formation of a growth rate plateau, i.e. crack growth rate is insensitive to ΔK level. The most common type of behaviour pertains to material-environment systems which exhibit stress corrosion fatigue above the K_{Iscc} and also true corrosion fatigue at all stress intensity values. Such behaviour is shown in Figure 2.2c.

2.2 Factors Affecting the Rate of Fatigue Crack Propagation

2.2.1. Environment

Corrosion fatigue is a generic term that describes the response of a material to the combined actions of cyclic loading and environmental effects. Previously, corrosion fatigue was most often used to describe the failure of materials under cyclic loading in overtly corrosive environments, such as salt water, high temperature gases and those prevalent in chemical processing applications. Corrosion fatigue can be extended to fatigue in ordinary air, where, although overt corrosion is considered to be of little consequence, there is still a measurable effect of the environment.

Environments employed in the laboratory can be listed in three groups:

a) Non-aggressive dry environments (vacuum, argon, nitrogen).

b) Mildly-aggressive environments (humid air, distilled water)

c) Significantly aggressive electrolytic conditions (salt water)

In an aggressive environment fatigue crack growth should be expected to consist of at least the environment attack, which is time-dependent, and the fatigue damage which is cycle dependent.

Dependence on time implies a frequency effect. This effect was clearly demonstrated for mildly aggressive environments [9,10,11,12,13]. An example is shown in Figure 2.3 which portrays the crack growth rate as a function of the water vapour pressure and suggests a sigmoidal relation with a saturation at higher pressure levels. Furthermore the abrupt transition in fatigue crack growth rate is clearly dependent on frequency.

Environmental effects on fatigue crack growth exhibit a tendency to diminish and ultimately vanish at high ΔK-values. It is generally supposed that fatigue crack growth at high ΔK-values is primarily a matter of (cyclic) plasticity and consequently environmental conditions should therefore be less significant.

Recently more attention has been focussed on the environmental fatigue crack growth behaviour of reactor pressure vessel (RPV) steels in light water reactor (LWR) environments [14,15,16,17]. Dufresne [17] has studied the effects of accidental deterioration of the high purity water used in reactors. A bibliography of incidents affecting the chemical characteristics of the reactor coolant in a PWR environment indicated that the frequency of these incidents was very low, because unlike the secondary system, the primary coolant system does not have the risk of a raw water intake to the condensers since its pressure is much higher. The only pollution occurring in practice is produced by the demineralisation system and is generally caused by chlorides [17].

Extrapolating from an analysis of the abnormal occurrences encountered during operation in PWR plants, the following out of specification incursions for the reactor coolant were anticipated for the 25 year-service of a PWR power plant:

- 4 chloride incursions with a maximum level of 0.80 ppm mainly during power operation,

- 2 oxygen incursions with a maximum level of 2.5 ppm during startup periods (temp <120°C),

- 1 oxygen incursion with a maximum level of 0.2 ppm during operation outside startup periods,
- 2 incursions due to pollution other than chlorides or oxygen, mainly due to fluorides or sodium during a startup period.

A crack growth test programme was performed by Dufresne [17] under the following conditions:

- non-polluted water,
- 10 ppm chloride,
- 10 ppm sodium,
- 3 ppm oxygen,
- 1 ppm oxygen and 10 ppm chloride,
- 3 ppm oxygen and 14 ppm chloride.

This programme produced the following main results (Figure 2.4). In the absence of oxygen, sodium or chloride concentrations of about 10 ppm do not significantly affect fatigue crack growth behaviour in the PWR environment. Oxygen concentrations of 3 ppm led to an increase in the crack growth rate (compared to the nominal environment) by about an order of magnitude at low values of ΔK (~20 MPa$\sqrt{m}$); with increasing ΔK level the extent of increased crack growth is reduced. The simultaneous presence of chloride and oxygen (Cl concentration : 10 to 14 ppm, O_2 concentration: 1 to 3 ppm) led to fatigue crack growth rates similar to those recorded in oxygenated PWR water.

Two mechanisms, dissolution-controlled and hydrogen-induced, have been suggested to explain environmentally enhanced crack growth in simulated light water reactor environments [18 - 25]. In the first mechanism the crack growth is controlled by anodic dissolution of the metal at the crack tip, while in the second the physical separation of the metal matrix at the crack tip is

assisted by hydrogen embrittlement. Both depend on the same rate determining parameter viz., rupture of the oxide film at the crack tip, and this makes it difficult to differentiate between them experimentally [18].

2.2.1.1 Anodic Dissolution Mechanism

In a dissolution mechanism (Figure 2.5) the environmental contribution to cracking involves metal dissolution at the crack tip which is anodic in nature. This mechanism has been explained by a number of models, viz.,

i) Slip Step Dissolution Model In this model, crack growth by anodic metal dissolution at the crack tip occurs as a result of the rupture of an otherwise protective surface film by the emergent dislocations.

ii) Stress Sorption Model Here, there is adsorption of the surface active species onto the exposed surface at the crack tip and this results in a reduction of the fracture stress.

iii) Brittle Film Rupture Model In this particular case crack growth is caused by the repeated formation and rupture of the brittle film which is growing into the metal at the crack tip.

Doig and Flewitt [19] stressed the importance of the local environment chemistry and mechanical conditions which prevail locally at the crack tip. Localized corrosion in crevices and pits result in the development of chemical and electrochemical differences between the occluded corrosion cell and the bulk environment. The tip of a growing corrosion fatigue crack is electrochemically different from the crack and bulk material surfaces in that localized plasticity presents a film free surface to the environment which introduces a galvanic contribution to the overall corrosion cell.

Crack geometry and length are important in controlling the localization of the chemical environment within the crack and

thereby the electrochemical conditions at the crack tip which determine the environmental contribution to the overall crack growth kinetics. Here the crack velocity decreases with increasing crack length for a constant applied stress intensity as the crack tip region becomes more remote from the influence of the free surface and bulk environment. The main difference between the static and cyclic load conditions, as far as solution chemistry is concerned, is that cyclic loading may produce solution mixing and renewal by the pumping action of the crack. Also the electrode reactions, particularly crack tip dissolution, may occur only during part of the fatigue cycle such that the steady state conditions are not established.

Enhanced crack tip dissolution occurs when the local dynamic strain and electrochemical conditions are sufficient to maintain the crack tip region free from a protective oxide film. During fatigue loading the dynamic strain conditions for enhanced anodic dissolution may be reproduced by the fatigue loading cycle. Thus, enhanced growth may be promoted in other environments and at stress intensity levels below those required for stress corrosion cracking but only during that part of the load cycle for which critical local strain rate and environment conditions exist. Thus the proportion of the loading cycle over which these conditions are satisfied will depend on load frequency, amplitude, mean load and cycle shape. At higher frequencies the corrosion reactions at a crack tip have little time to contribute to the mechanical crack advance which occurs with each fatigue cycle and environmental enhancement of crack growth under these conditions is negligible. This is particularly true for high R values where the solution chemistry within the crack achieves a pseudo-equilibrium with sufficient time for diffusional processes to smooth any composition or potential differences resulting from crack tip electrochemical reactions. As the test frequency and strain rates decrease, both the corrosion and the diffusional processes become more significant with longer operational time. Thus, environmental changes may occur at the crack tip during the fatigue cycle which, in turn, influence the range of strain rates over which enhanced anodic dissolution may occur.

thereby the electrochemical conditions at the crack tip which determine the environmental contribution to the overall crack growth kinetics. Here the crack velocity decreases with increasing crack length for a constant applied stress intensity as the crack tip region becomes more remote from the influence of the free surface and bulk environment. The main difference between the static and cyclic load conditions, as far as solution chemistry is concerned, is that cyclic loading may produce solution mixing and renewal by the pumping action of the crack. Also the electrode reactions, particularly crack tip dissolution, may occur only during part of the fatigue cycle such that the steady state conditions are not established.

Enhanced crack tip dissolution occurs when the local dynamic strain and electrochemical conditions are sufficient to maintain the crack tip region free from a protective oxide film. During fatigue loading the dynamic strain conditions for enhanced anodic dissolution may be reproduced by the fatigue loading cycle. Thus, enhanced growth may be promoted in other environments and at stress intensity levels below those required for stress corrosion cracking but only during that part of the load cycle for which critical local strain rate and environment conditions exist. Thus the proportion of the loading cycle over which these conditions are satisfied will depend on load frequency, amplitude, mean load and cycle shape. At higher frequencies the corrosion reactions at a crack tip have little time to contribute to the mechanical crack advance which occurs with each fatigue cycle and environmental enhancement of crack growth under these conditions is negligible. This is particularly true for high R values where the solution chemistry within the crack achieves a pseudo-equilibrium with sufficient time for diffusional processes to smooth any composition or potential differences resulting from crack tip electrochemical reactions. As the test frequency and strain rates decrease, both the corrosion and the diffusional processes become more significant with longer operational time. Thus, environmental changes may occur at the crack tip during the fatigue cycle which, in turn, influence the range of strain rates over which enhanced anodic dissolution may occur.

2.2.1.2 Hydrogen Embrittlement Mechanism

In the hydrogen embrittlement mechanism, (Figure 2.6), the environmental contribution to cracking involves hydrogen atoms inside the metal thereby leading to some form of material degradation. Hydrogen may enter the material from external environments such as hydrogen permeation from physi- and chemisorption of gaseous hydrogen, or cathodic production of hydrogen atoms in aqueous environments. Several models have been proposed to explain this mechanism viz;

i) Pressure Model This is as a result of the pressure build up in internal voids of molecular hydrogen.

ii) Decohesion Model Here hydrogen causes a decohesion of the metal lattice

iii) Stress Sorption Model Adsorption of hydrogen reduces the surface energy and hence the fracture stress is much reduced.

iv) Hydrogen-rich Phase (i.e. Hydride) In this model hydrogen reacts with some compositional elements to form a brittle hydrogen rich phase.

v) Hydrogen affected plastic deformation This involves the transportation of hydrogen to the areas of maximum stress triaxiality and maximum dilation.

The most important issue, insofar as it relates to phenomenological understanding of load-environment interactions, appears to be the identification of the rate controlling process for environment assisted crack growth. The possible sequential processes involved in environment assisted crack growth are illustrated schematically in Figure 2.7 for a ferrous alloy exposed to a hydrogenous gas [29].

Unlike the anodic dissolution mechanism, fractography has in many cases produced definite evidence to indicate that the hydrogen embrittlement mechanism is operative. Corrosion fatigue

and stress corrosion cracking specimens under cathodic polarisation exhibited similar features such as fan shaped facets that were usually associated with manganese sulphide inclusions. Bulloch and Buchanan [15] in their study showed that the appearance of these fan-shaped facets at low ΔK levels can be associated with the initial environmental acceleration in cyclic crack growth rate. Also, such features were markedly reduced at the plateau velocity and at post plateau growth rates. The correlation of these fan-shaped features with environmentally assisted growth behaviour has been recently reported by a number of investigators [15,20,21,23] but the fact that they are usually associated with manganese sulphide inclusions shows that the inclusion level could be an important factor in corrosion fatigue behaviour. Wilson [25] showed that the type II MnS inclusions increased the fatigue crack growth behaviour of SA 533 B steel in air. Since these inclusion formations act as planes of weakness due to the decohesion at the steel-inclusion interfaces, this decohesion appeared to take place without much difficulty or resistance at the interface at all ΔK levels.

It has recently been demonstrated [20] that in a PWR environment manganese sulphides readily dissolve to form soluble sulphide species (H_2S, HS^-, S^{2-}) and therefore inclusions can have a greater effect on fatigue behaviour in a water environment than in air [24]. The fractographic results presented by Bulloch and Buchanan [15] suggest that the fan-shaped facets do not result from a simple mechanical effect associated with inclusions, but that a more likely reason is the local alteration in the water chemistry at the crack tip that results from the dissolution of the MnS inclusions in a water environment. This localized change in crack tip water chemistry results in an environment which is aggressive enough at the start of the test to cause fan-shaped facets due to H_2S preventing the recombination of atomic hydrogen and thus more hydrogen can enter the metal matrix. However, as the test progresses the crack tip water chemistry becomes less aggressive, as a result of the pumping action of the crack, and the extent of environmentally enhanced crack growth is much reduced.

Recent workers [26] have observed that when enhanced growth rates were observed the fractography changes from a mainly ductile striated structure containing some microvoids to one of almost entirely microvoid coalescence. It was suggested that the transition from the mainly ductile striated surface to one of almost entirely dimpled rupture (microvoids) was related to a local variation in test conditions and/or the onset of stage III growth. However, it is possible that the occurrence of microvoids and concomitant environmentally assisted fatigue crack growth, could result from a hydrogen assisted cracking mechanism similar to that discussed by Beachem [27].

2.2.2 Frequency

The effects of frequency on fatigue crack growth behaviour have been investigated over a wide range of frequencies in several environments and in various materials, viz., high and medium strength steels [9,10,14,28,29,30], aluminium alloys [6,31], stainless steels [32] and titanium alloys, [6,7]. It was reported that acceleration of the fatigue crack growth rate occurred and that the magnitude of this acceleration is frequency, environment, material and stress intensity dependent. That is, the magnitude of the environmental acceleration can be increased or decreased substantially by changing one of these parameters. The effect of frequency will now be discussed under the following headings;

(i) True Corrosion Fatigue,

(ii) Low Stress Intensity Levels and

(iii) Stress Corrosion Fatigue.

2.2.2.1 True Corrosion Fatigue

It is generally accepted that for steels and at medium frequencies (i.e. 1-200 Hz), the fatigue crack growth rate is

independent of frequency in air. An upper bound growth law, for SA 533 B-1 collected both in air and reactor water environment at various frequencies, is presented in Appendix A to Section XI of the ASME Code (Figure 2.8). This curve is intended as a reference curve for the estimation of the growth which a flaw detected during inspection would experience during the forthcoming period of service.

In an "aggressive" environment, however, there is an increase in the rate of fatigue crack growth with a decrease in frequency. Also, at higher frequencies the crack growth rate is essentially the same as in air, thus the environment has a negligible effect on the fatigue crack growth rate. This can be explained in terms of the idea proposed by Barsom [4] that corrosion fatigue crack propagation below K_{Iscc} is an unstable equilibrium process due to a balance between two opposing mechanisms. One process is due to environmental attack, which enhances fatigue crack propagation rates compared to an inert environment, but which disappears at very high frequencies or fast loading rates when there is insufficient time for environmental attack. The other competing process viz., oxide layer formation, which results in a reduction in the environmental component of crack propagation, controls the crack growth rate at very low frequencies. The magnitude of the effect of cyclic frequency depends strongly on the environmental-material system.

Atkinson and Lindley [10] observed that under constant ΔK and K_{max} conditions, there was a very pronounced peak in the da/dN vs. frequency plot for En 56C and SA 533 B-1 (Figure 2.9). There existed a critical frequency (f_{crit}) at which maximum environmental attack occurred, i.e. between 0.01 and 0.1 Hz, while below f_{crit} the fatigue crack propagation rate decreased as the testing frequency was lowered. Data on En56C revealed that the critical frequency increased with increasing temperature. Gerber et al [14] testing SA 508-cl2 found that lowering the frequency from 0.37 to 0.037 cpm (0.00617 to 0.000617 Hz) in a Boiling Water Reactor (BWR) environment caused only a small increase in the growth rate. This result suggests that, in this case, the effect of frequency may saturate at low frequency levels. Bamford [33] found that the crack growth rate

increases with decreasing cyclic frequency, reaching a maximum acceleration at a frequency between 0.1 and 1.0 cpm (0.00167 and 0.0167 Hz).

2.2.2.2 Low Stress Intensity Levels (Near ΔK_{th} levels)

Fatigue crack growth data for SA 533 B 1 presented by Paris et al [34] in Figure 2.10, seems to suggest that the threshold stress intensity factor, ΔK_{th}, is unaffected by an aqueous environment. Similarly data by Speidel et al [6] suggests that ΔK_{th}, for aluminium and magnesium alloys, is also essentially unaffected by various aqueous environments. However, to establish ΔK_{th} within a reasonable test time, these data were obtained at fairly high cyclic frequencies. Since at high frequencies the environment has significantly less effect on the rate of fatigue crack growth below K_{Iscc}, the invariance of ΔK_{th} at high cyclic frequencies in aggressive environments is not surprising.

Limited data relating to the effect of cyclic frequency on ΔK_{th} in aqueous environments has been obtained for various steels with somewhat surprising results. Contrary to what might be expected, viz., a lowering of ΔK_{th} with a lowering of frequency, Barsom [35] found that for A514 steels tested at 0.2 Hz in 3% sodium chloride solution, the ΔK_{th} level was about 12 MPa$\sqrt{m}$ which was about double the ΔK_{th} value recorded in air at ambient temperatures. Bucci and Donald [36] observed that the "environmental" ΔK_{th} in a 200 grade maraging steel forging was higher than that in air and concluded that salt water appeared to produce an inhibiting effect on fatigue cracking at very low ΔK levels. Paris et al [34] also observed that the threshold stress intensity of SA 533 Grade B Class 1 steel in distilled water was greater than that established in air at ambient temperature. Atkinson and Lindley [10] found that at low ΔK (20 MPa$\sqrt{m}$) and low frequency (1 Hz) the crack retardation effect illustrated in Figure 2.11 was observed in SA533 B-1 during a constant ΔK step. The fatigue crack growth rate was initially faster than an equivalent test in air, but gradually slowed down and eventually crack arrest occurred after about 1mm of fatigue crack growth. In an air environment for the various steels tested, the threshold

(ΔK_{th}), is independent of cyclic frequency. Since aggressive environmental effects on fatigue crack growth decrease with increasing frequency, the corrosion fatigue ΔK_{th} at very high frequencies would have a value close to that of fatigue in air. A K_{Iscc} test can therefore be loosely considered as a corrosion fatigue test at extremely low frequency because with decreasing test frequency the actual threshold condition approaches the K_{Iscc} value.

Hence, the value of the environmentally assisted ΔK_{th} at intermediate cyclic frequencies must be greater than ΔK_{th} for air and less than the value of K_{Iscc} for the environment-material system under consideration. Based on the preceding observations, a schematic representation of the corrosion fatigue behaviour of steels subjected to different frequencies has been constructed, as shown in Figure 2.12 [37].

2.2.2.3 Stress Corrosion Fatigue

The rate of corrosion fatigue crack growth above K_{Iscc} must be greater than the rate below K_{Iscc} because whenever the magnitude of the maximum stress intensity factor in a given cycle becomes greater than K_{Iscc}, the rate of corrosion fatigue crack growth should be accelerated by stress corrosion cracking. Based on the assumption that above K_{Iscc} the fatigue crack growth in an aggressive environment is enhanced by the same magnitude as that for crack growth under sustained loads, Wei and Landes [38] developed a linear summation model to predict the corrosion behaviour above K_{Iscc} for high strength steels.

This model can be used for making quantitative estimates of the effects of cyclic loading variables (such as frequency, waveform and stress ratio) on environment-enhanced fatigue crack growth for certain alloy-environment systems.

$$\left[\frac{da}{dN}\right]_T = \left[\frac{da}{dN}\right]_{fat} + \left[\frac{da}{dN}\right]_{sc}$$

$$= \left[\frac{da}{dN}\right]_{fat} + \int \frac{da}{dN}\, K(t)\, dt$$

In this model, the total corrosion fatigue crack growth rate $(da/dN)_T$, is considered to be the sum of two components, viz., one representing the rate of fatigue crack growth in an inert environment, $(da/dN)_{fat}$, and another concerning the stress corrosion fatigue crack growth rate component, where $(da/dN)_{sc}$ is the stress corrosion crack growth rate computed by integration of the rate of sustained load crack growth, (da/dt), corresponding to the load profile, K(t), over one cycle of loading. The effects of frequency and other loading variables are incorporated through the load profile, K(t) (i.e. the variation of the crack tip stress intensity factor K over one loading cycle).

Following the original formulation of the model, comparisons were made with available experimental data on an 18 Ni(250) maraging steel tested in dry (dehumidified) hydrogen, and the same medium carbon, low alloy, high strength steels tested in distilled water and in dehumidified gaseous environments [38]. As shown in Figure 2.13 these comparisons showed that this superposition model essentially predicted the effect of frequency. Thus, it can be seen from Figure 2.13 that as the frequency decreases the rate of crack propagation increased. Caution has to be exercised when using the model since there are definite limitations. Such limitations include the fact that it is only applicable for stress corrosion fatigue since it is assumed that the environmental contribution to cracking arises solely from sustained load stress corrosion cracking.

2.2.3 Waveform

Available data indicates that the environmental effects on the rate of fatigue crack growth in corrosion fatigue below K_{Iscc} is highly dependent on the shape of the cyclic stress wave [8,10,39,40,41]. This dependence, as shown by Barsom [39], is

illustrated by the difference between the fatigue crack growth rate data for 12Ni-5Cr-3Mo maraging steel in an ambient air environment (Figure 2.14) and in a 3% solution of sodium chloride (Figure 2.15) under sinusoidal loading, triangular loading, and square loading at a frequency of 6 cpm (0.1 Hz). All the corrosion fatigue tests were conducted on identical specimens, in the same bulk environment, and at the same maximum and minimum loads, and thus, the effect of the cyclic waveform on corrosion fatigue behaviour below K_{Iscc} was obtained by direct comparison between the crack growth rates per cycle.

The data presented in Figure 2.14 shows that the fatigue crack growth behaviour in a room temperature air environment is identical under the various stress fluctuations and is essentially independent of frequency. Also the data in Figure 2.15 illustrates that crack growth rates in the sodium chloride environment under sinusoidal and triangular stress fluctuations are almost identical, viz., at constant frequency, the environment increased the crack growth rate by the same amount under sinusoidal stress fluctuations as under triangular stress fluctuations. However, these particular data also show that environmental effects were negligible when the steel was subjected to a square wave stress fluctuation. Corrosion fatigue crack growth behaviour, under square wave loading tested in a sodium chloride environment, was essentially similar to that in the absence of environmental effects.

The apparent immunity of the 12Ni-5Cr-3Mo steel to the environment under square wave stress fluctuation does not reflect an inherent immunity of this alloy to the environment, since crack growth rates in this particular alloy increased for both the sinusoidal and trianglar waveforms. Thus, such immunity to environmental affects must reflect significant differences in the manner to which the stress changes in each cycle. By establishing the sinusoidal cyclic frequency that would result in the same environmental effects on the rate of fatigue crack growth, Barsom [39] showed that the environmental effects on fluctuations occur primarily while the material at the crack tip is being plastically deformed. Corrosion fatigue data obtained below K_{Iscc}, using square waves with different dwell times at

maximum and minimum loads, exhibited no environmental effects at constant tensile stresses.

The differences between environmental effects during increasing tensile load and decreasing tensile load are clearly understood when the corrosion fatigue data obtained under triangular loading are compared with the appropriate data obtained under positive and negative sawtooth waves (these are the first and second halves of the triangular waveform). True comparisons in corrosion fatigue behaviour are those made between cyclic stress fluctuations with transient stresses that are equal in rate and duration.

The data showed that the corrosion fatigue crack growth rates determined with both negative sawtooth and square waveforms were the same as the fatigue crack growth rate determined in air. The environmental effect in this particular case depends on the waveform, with the negative sawtooth and the square waveform tests exhibiting no environmental effects. The corrosion fatigue crack growth rates determined with sinusoidal, triangular and positive sawtooth cyclic stress fluctuations were identical, but were three times higher than fatigue crack growth data determined in air; thus the environment significantly affected fatigue crack growth behaviour. Furthermore, because the environmental effect increased the rate of fatigue crack growth below K_{Iscc} by the same amount for both the triangular and positive sawtooth waveforms, the corrosive processes were only operative during the tensile portion of the fatigue cycle.

It is interesting to note that while these phenomena were found for the 12Ni-5Cr-3Mo - sodium chloride solution system they do not necessarily apply to all material-environment systems. This was demonstrated by fatigue crack growth data for 7075-T6 aluminium alloys tested in salt water at 0.1 Hz under sinusoidal, square wave, positive sawtooth, and negative sawtooth loading which showed crack growth behaviour very similar to that presented for the 12Ni-5Cr-3Mo maraging steel in salt water [42].

Atkinson and Lindley [10] working on SA533-B1 in 3.5% NaCl solution and distilled water found similar results to those

observed by Barsom [39]. They also found that at very slow strain rates below a critical frequency, f_{crit}, the passive film formation reaction is thought to inhibit the corrosion process involved in stress corrosion cracking, and at very fast strain rates only pure mechanical fatigue effects are observed. It was also pointed out that constant load (increasing ΔK) tests may lead to different crack growth rates from constant ΔK conditions, particularly at low testing frequencies, when the crack tip profile may progressively change during a test due to dissolution controlled blunting, which may differ between constant and steadily increasing K conditions.

Austen and Walker [8] investigating the effects of cyclic waveform on true corrosion fatigue at stress ratio, R = 0.1, and stress corrosion fatigue at R = 0.8 found a significant waveform effect. This study was performed in 3.5% NaCl solution at a frequency of 4 Hz. However, fatigue crack growth data for 7075-T651 aluminium alloy tested at 1.75 Hz in distilled water showed no significant difference in the crack growth behaviour under positive and negative loadings [43]. In true corrosion fatigue, sinusoidal and positive sawtooth waveforms produced rates of growth 50% faster than those obtained in air. A triangular waveform produced identical rates to those in air whilst square waves and negative sawtooth waveforms gave crack growth rates that were 20% slower than those obtained in air. The stress corrosion fatigue data also fall into two groups. In this case square wave, sine wave and negative sawtooth data exhibit good commonality inasmuch as they show plateau growth rates of about 2.2×10^{-4} mm/cycle whereas positive sawtooth and triangular waveforms both give plateau rates that are about 50% slower.

The fact that the rates of crack growth in 3.5% NaCl solution for square wave and negative sawtooth were less than those in air but for a triangular waveform are the same as in air is attributed to crack tip blunting by general corrosive attack. In stress corrosion fatigue the behaviour for triangular, positive sawtooth and negative sawtooth waveforms would be expected to be identical. However, the results are again attributed to blunting, probably as a consequence of microbranching.

Amzallag et al [41] conducted tests on SA533 B1 and SA508 cl3 steels (sulphur levels 0.013 and 0.009 respectively) in two PWR environments viz., 288°C (83 bar pressure) and 300°C (140 bar pressure) at R-ratios of 0.2 and 0.6. In the case of the material containing 0.013% sulphur with R = 0.2 a significant difference appeared between the results of the tests carried out with the triangular and sinusoidal waveforms. The triangular waveform gave a typical straight line Paris law type fatigue behaviour while the sinusoidal waveform gave environmentally assisted plateau behaviour i.e., an initial rapid increase of the growth rate with ΔK level followed by a plateau where growth rate is insensitive to ΔK level. In the case of the tests carried out on the material containing 0.009% sulphur with R = 0.6, the results obtained with sinusoidal and triangular waveforms are similar yielding Paris law type behaviour i.e. no environmentally assisted crack growth.

It is interesting to note that Bulloch and Buchanan [15] performed almost identical tests in terms of material, environment, waveform, R-ratio and sulphur content and obtained identical results for the low R-ratio tests at the same frequencies. However, at high R-ratio in PWR environment these workers observed significant environmental enhancement for sinusoidal waveform. Both Amzallag et al [41] and Bulloch and Buchanan [15] interpret their results in terms of sulphur content in the steel. Amzallag attributed his findings to the bulk sulphur content saying that the sinusoidal waveform is more detrimental than triangular waveform for the material having the highest sulphur content. Bulloch, however, explained his findings in terms of size, type and distribution of MnS inclusions and has recently presented strong fractographic evidence [15] in support of his argument.

2.2.4 Non-Metallic Inclusions

In his review paper, Ritchie [2], discussed the effect of non-metallic inclusion content on near-threshold fatigue behaviour of a medium strength pearlitic rail steel. It was found that, whereas decreasing the volume fraction of inclusions (sulphide

stringers and oxide type) led to marked increases in the fatigue or endurance limit, no systematic effect was observed on the value of the threshold ΔK_{th}. However, other studies [25] on the influence of steelmaking practice on the somewhat higher fatigue crack propagation rates in a nuclear pressure vessel steel, SA 533 B, have shown that the absence of elongated type II MnS inclusions and "galaxies" of alumina inclusions by calcium treating or electroslag remelting resulted in a significant improvement in the isotropy of fatigue crack growth behaviour and lower overall growth rates.

Craig [23] noted in a recent study of the resistance of tempered 4130 type steels to hydrogen assisted cracking that certain characteristic features were present on the fracture surface. The fracture surface displayed numerous regions of flat fracture in which was centrally located one or more non-metallic inclusions. These inclusions were either singular compounds such as MnS or Al_2O_3, or a complex composition. Other features common to these flat fracture regions are ridges radiating from the inclusion toward the periphery of the zone and the smooth brittle appearance of the zone itself at higher magnification. It was concluded [23] that hydrogen trapped at inclusion sites will aid in crack propagation when a crack is initiated at or in an inclusion, once sufficient strains have been realised. Hydrogen concentrated around the inclusion near the crack tip could then induce brittle crack growth by promoting loss of cohesion.

Other workers [44] investigated the effect of inclusion volume fraction and orientation on hydrogen assisted cracking in two medium carbon steels of similar chemical compositions, but containing different sulphur contents. The crack growth behaviour of the lower sulphur steel (S = 0.038%) indicated that all of the orientations exhibited the growth behaviour characteristic of hydrogen assisted cracking, namely a K independent stage II and a steeply falling stage I. The results of the higher sulphur steel (S = 0.15%) tested at the same strength and in the same environment revealed the same trends as the low sulphur steel but with a wider spread in stage II growth rates and more pronounced anisotropy in threshold values.

Fractographic examination revealed evidence of decohesion of the inclusion matrix interfaces. It was also noted that the mechanism of matrix separation was changed to a predominantly quasi-cleavage mode, and that the potential for environmental attack is greatest when the inclusions have the major axes oriented parallel to the direction of crack growth. Clearly an elongated sulphide inclusion oriented at right angles to the crack front will cause a more pronounced change in the local water chemistry than one lying perpendicular to the crack front. The inclusion initiated secondary cracks were observed to develop at distances from the crack tip which were considerably in excess of the plain strain plastic zone size. These secondary cracks were only observed to be associated with clusters of closely spaced inclusions. The stress fields from the adjacent inclusions can interact to produce an extensive area of stress intensification. As the internal pressure continues to increase sudden bursts of crack growth occur. Thus hydrogen assisted cracking occurs if there is; (i) a sufficient availability of hydrogen at high activity and (ii) if inclusions are sufficiently closely spaced. Clearly therefore, it does not necessarily depend on the volume fraction of sulphur. These conclusions were in direct contrast to those of Amzallag et al [41] who conducted fatigue tests on two casts of SA 533B with differing bulk sulphur levels and found that the crack growth rate in a PWR environment was greater in the higher sulphur steel. They therefore concluded that the increased crack growth rate may be attributed to the bulk sulphur content.

Bulloch and Buchanan, [15] while studying the crack growth behaviour of SA 533 in PWR water also observed environmentally enhanced crack growth. Fractographic evidence produced by these workers indicated that the incidence of brittle fan-shaped facets which are usually associated with non-metallic MnS inclusions can be related to local environmentally enhanced crack growth.

2.3 Variable Amplitude Loading

Since the majority of engineering components in service are

subjected to variable amplitude, spectrum or random loading rather than constant amplitude loading, an appreciation of the influence of periodic overloads and block loading sequences on fatigue crack propagation is clearly of practical significance.

Classically, the approach taken for variable amplitude loading in fatigue design is to use the Palmgren-Miner relationship, where for a body subjected to n_i number of cycles of different stress amplitude $\Delta\sigma_i$, with i= 1 to k,

$$\sum_{i=1}^{k} \frac{n_i}{N_i} = 1$$

where N_i is the number of cycles to failure had all the stress amplitudes been of magnitude $\Delta\sigma_i$. This approach, which is utilized for total life prediction and thus includes both crack initiation and crack propagation stages, predicts that the cycles to failure will be decreased if a single large positive overload is applied during constant amplitude cycling. However, as shown schematically in Figure 2.16, the effect of such an overload on Mode I crack propagation rates is to initially retard crack growth, sometimes to the point of arrest, and thus to increase the propagation life. Hence it is apparent that the practical application of Miner's rule to crack propagation behaviour under variable loading may be inappropriate.

For crack growth studies, however, the above approach can be used for narrow band random loading where each cycle does not differ significantly from its predecessor. Here interaction effects can be considered small and it is reasonable to assume that each cycle causes the same amount of crack extension as if it were applied as part of a sequence of constant amplitude loads. For broad band loading, on the other hand, cyclic crack extension has been estimated on the basis that the load, or stress intensity, ranges are constant at their root mean square value. Thus the average fatigue crack growth rate per cycle is given by;

$$\frac{da}{dN} = A\,(\Delta K_{rms})^{n}$$

where A and n are constants and

$$\Delta K_{rms} = \sqrt{\frac{\sum_{i=1}^{k} \Delta K_i^2}{n}}$$

However, since loading sequence interaction effects are more relevant for broad band loading, this procedure often yields conservative predictions for Mode I crack advance.

2.3.1 Retardation

Several investigators [45-48] have observed that the application of a single positive overload of sufficient magnitude (generally 50% of the baseline load range) can result in significantly retarded crack growth over a crack length increment which is of the order of, or greater than the overload plastic zone size, whereupon crack growth rates return to their original baseline level. It has been shown [45,49] that cracks overloaded in this fashion may totally arrest where the effective stress intensity range actually experienced at the crack tip is reduced below ΔK_{th}. However, the onset of the retardation or crack arrest often does not coincide with the actual overload cycle but is delayed until the crack has grown some distance into the overload plastic zone (so-called delayed retardation) [46,47,48,50].

For fully reversed overload cycles, the application of an underload prior to a single overload does not appear to have much effect on subsequent retardation, whereas an underload following an overload tends to mitigate the retardation effect [49]. Block loading sequences [48,49,51] are also known to produce large transient effects on fatigue crack growth behaviour. For example, high-low block loading sequences, where the stress or stress intensity range is reduced from one constant level to a lower one, can result in an initial retardation (or crack arrest) which is significantly greater than for an equivalent single overload.

Several models have been advanced to explain the phenomenon of crack growth retardation. In general, these models attribute the delay behaviour to residual stresses [52], crack tip blunting [53] or fatigue crack closure concepts [53]. Of the various hypothetical mechanisms introduced, none as yet has been conclusively shown to yield a true mechanistic rationale to the observed fatigue crack growth behaviour following an overload.

However, several of these mechanisms have been successfully used to empirically model retarded crack growth behaviour. Suresh et al [54] in a recent analysis of the post-overload retardation effect suggested that during the overload cycle, the crack tip profile becomes blunted often with one or two 45° branch cracks subsequently emanating from the tip (on the plane of maximum shear stress). The reduction in effective stress intensity range resulting from this blunted and branched crack, coupled with the fact that the crack is now propagating into the compressive residual stress field from the overload plastic zone, acts to retard crack growth to near-threshold levels and in certain cases causes arrest. Furthermore, the retardation can be enhanced during the initial post-overload region because the crack is experiencing effective stress intensity ranges in the near-threshold regime such that the process of crack advance becomes influenced by additional crack closure mechanisms. Specifically, the branched morphology of the overloaded crack together with the single shear faceted nature of the subsequent crack growth can promote significant roughness induced crack closure, evident by severe abrasion between the crack faces in the post overloaded zone. It was also noted that the stretch zone created at the application of the overload was free from abrasion marks, which suggested that the initial blunting of the crack tip minimized the effect of plasticity induced crack closure in the subsequent retardation in crack growth. Similar arguments involving crack tip blunting and branching, residual compressive stress, and crack closure mechanisms have been advanced to rationalise transient crack growth behaviour following spectrum and block loading sequences.

2.3.2 Crack Closure Mechanisms

Implicit in the analyses of fatigue crack propagation so far, is the assumption that the full range of ΔK, computed on the basis of K_{max} - K_{min} from applied loads and crack length measurements, is available as the nominal driving force for crack tip extension. However, should physical contact between the mating crack surfaces occur at positive loads during the fatigue cycle as a result of the local deformation and fracture processes, this driving force would be effectively limited at the crack tip. Elber [53] was one of the first in developing this concept in his proposal of fatigue crack closure.

2.3.2.1 Plasticity Induced Crack Closure

Plasticity induced crack closure can be considered to occur from interference between crack surfaces in the wake of the crack tip, arising from the constraint of surrounding elastic material on the residual stretch in material elements previously plastically strained at the tip. This process is aided by the fact that the crack is growing into a reversed plastic zone in which a state of residual compressive stress exists (Figure 2.17). Since the crack cannot propagate whilst it remains closed, the net effect of this closure is to reduce the nominal stress intensity range, ΔK, to some lower effective value ΔK_{eff} actually experienced at the crack tip, i.e.,

$$\Delta K = K_{max} - K_{min} \text{ (no closure)}$$

$$\Delta K_{eff} = K_{max} - K_{cl} \text{ (with closure)}$$

where K_{cl} is the stress intensity to close the crack i.e. crack tip no longer under tensile stress ($>K_{min}$)

This phenomenon was effectively demonstrated by Elber [53] for crack propagation at high stress intensities in aluminium alloys by mounting surface strain gauges of very small gauge length at the tips of fatigue cracks. The resulting elastic compliance

curves as schematically illustrated in Figure 2.18 where it is apparent that a specimen containing a fatigue crack of length, a, initially "behaves" as if no crack were present before following the expected compliance slope for a physically open flaw of the same length. The transition point in this curve thus defines the physical closing (or opening) load and hence the value of K_{cl}. Subsequently, other experimental measurements of closure loads have been performed using crack mouth opening gauges [55-57], strain gauges [58-60] and electric potential measurements [57], although the data are not always totally consistent when compared between different procedures.

One of the more serious objections [61] to this concept is that the magnitude of plasticity induced closure is highest under essentially plane stress conditions, yet in thin sheet specimens where such conditions of plane stress often exist, mean stress effects are generally minimal. Furthermore, the major influence of mean stress is usually found at the ultra low growth rates associated with near threshold fatigue, where invariably plane strain conditions are present. Recently experimental compliance measurements [61] on near-threshold cracks have confirmed that very significant effects of closure are present in plane strain, although it is difficult to explain these effects solely in terms of the plasticity arguments of Elber [53]. Accordingly, several other mechanisms of crack closure have been identified based on the role of crack surface corrosion deposits and fracture surface roughness. These closure mechanisms are specifically relevant to the near-threshold regime, since it is principally here that the size-scales of the debris and the roughness of the fracture surface is comparable to the crack tip opening displacements.

2.3.2.2 Oxide Induced Crack Closure

The origin of oxide induced crack closure arises from the fact that during near threshold fatigue crack propagation at low load ratios in moist environments, corrosion deposits of a thickness comparable with the size of crack tip opening displacements can build up near the crack tip, thus providing a mechanism for enhanced closure such that the crack becomes "wedged" closed at

stress intensities above K_{min}. Such oxide films are thickened at the low load ratios by a mechanism of "fretting oxidation" [54], i.e. a continual breaking and reforming of the oxide scale behind the crack tip due to the "smashing" together of the crack surfaces as a result of plasticity induced closure. For example, in lower strength steels tested in moist air at R = 0.05, oxide films have been observed near ΔK_{th} with a maximum thickness some 20-40 times larger than the limiting thickness of films formed naturally on metallographically polished samples exposed to the same environment for similar periods. Since the formation of enhanced crack surface oxide deposits is far less predominant in dry, oxygen free environments, at high load ratios (where plasticity induced closure effects are minimal) and in higher strength materials (where fretting oxidation is less effective), the resulting concept of oxide induced crack closure provides an attractive explanation for many of the somewhat surprising effects (the decrease in threshold value when test atmosphere was changed from air to hydrogen) of microstructure and environment on near threshold behaviour.

2.3.2.3 Roughness Induced Crack Closure

A further mechanism of crack closure is that induced by fracture surface roughness or morphology (Figure 2.17). Such roughness-induced closure can arise where the size scale of the fracture surface roughness is comparable to crack tip opening displacements and where significant Mode II displacements exist, such that the crack can become wedged closed at discrete contact points along the crack faces. Like oxide induced closure, this mechanism is most prevalent at low stress intensity ranges where maximum plastic zone sizes are typically smaller than microstructural dimensions. In this regime, crack advance proceeds via a single shear mechanism, with associated Mode I and Mode II displacements, resulting in serrated fracture paths which obviously enhance the closure effect. Such roughness induced closure provides an important contribution to the role of microstructure in influencing near threshold crack growth and in fact has wide significance to a large range of engineering materials (e.g. titanium alloys which form little oxide debris).

For example, with respect to the well-known observations [2] of improved near threshold crack growth resistance in coarser grained materials, coarse microstructures tend to promote rougher fracture morphologies, and further delay the transition from a serrated (single shear) to a more planar (alternating or simultaneous shear) fracture surface to higher ΔK values, when r_{max}, the plastic zone size, is approximately equal to the grain size. As a result coarse microstructures will promote more closure such that the effective ΔK values will be lower, at the same nominal ΔK, than in finer-grained microstructures. This explanation is entirely consistent with the fact that at high load ratios where closure effects are minimal, the effect of grain size on near threshold behaviour is markedly reduced.

Both oxide induced and roughness induced crack closure mechanisms predominate at near threshold levels but it is worth noting that their effect is not necessarily unique to this regime.

2.4 Summary

This chapter reviews some of the available literature for corrosion fatigue crack propagation in metals. Attention was focussed on some specific factors which have been shown to affect the rate of fatigue crack propagation viz., environment, frequency, waveform and non-metallic inclusions. Special emphasis was placed on the mechanisms by which environmentally assisted crack propagation occurs i.e. hydrogen assisted cracking and anodic dissolution models. The effects of variable amplitude loading on fatigue crack propagation were also considered. The observed phenomenon of retardation of the fatigue crack growth following overload cycles in such cycles has been shown to arise primarily due to crack closure.

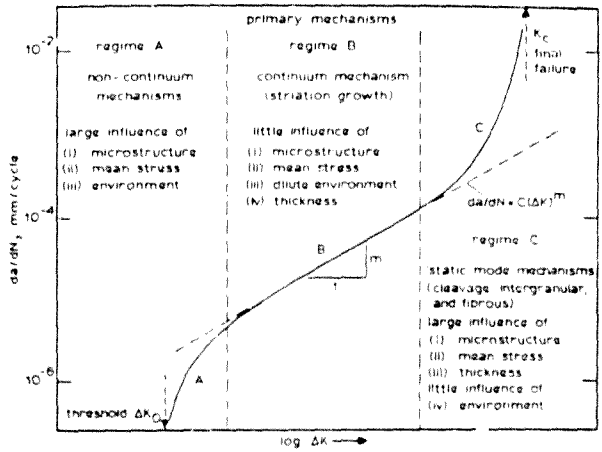

Figure 2.1: Schematic variation of fatigue crack growth rate da/dN with alternating stress intensity ΔK in steels, showing regimes of primary crack growth mechanisms. Ritchie [2].

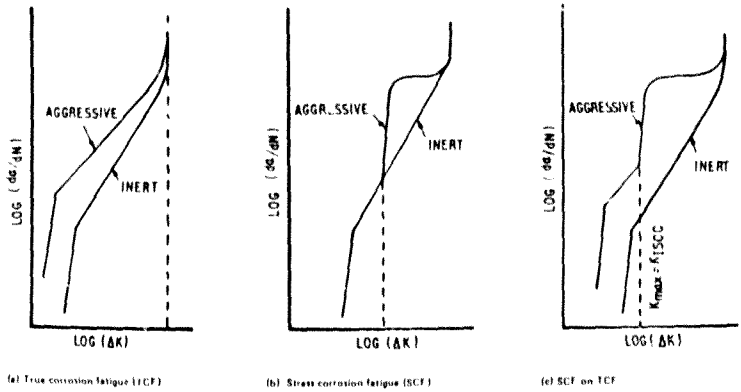

Figure 2.2: Schematic illustrations of the three basic types of corrosion fatigue crack growth behaviour. Austen and Walker [8].

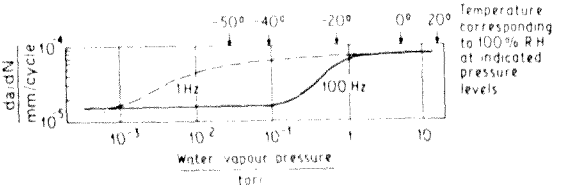

Figure 2.3: The effect of water vapour on crack growth rate. Material RR58, $\Delta K = 8.3$ MN/m$^{3/2}$.

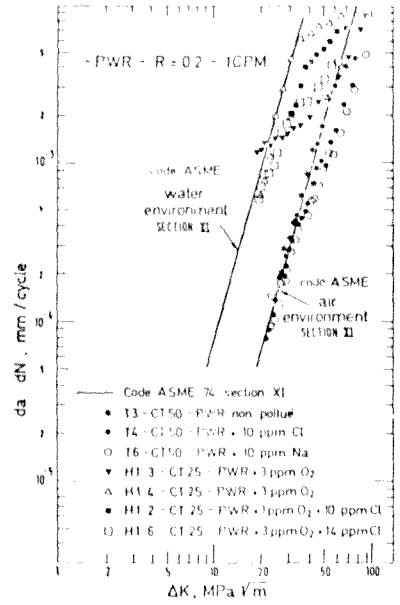

Figure 2.4: Fatigue crack growth of A 508 cl3 steel in water containing impurities. Dufresne and Rieunier [17].

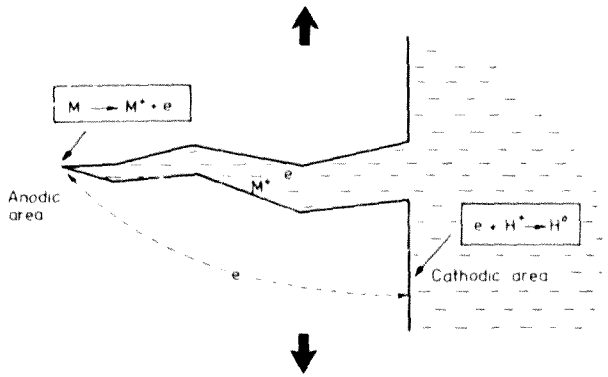

Figure 2.5: Schematic Illustration of the Anodic Dissolution Model.

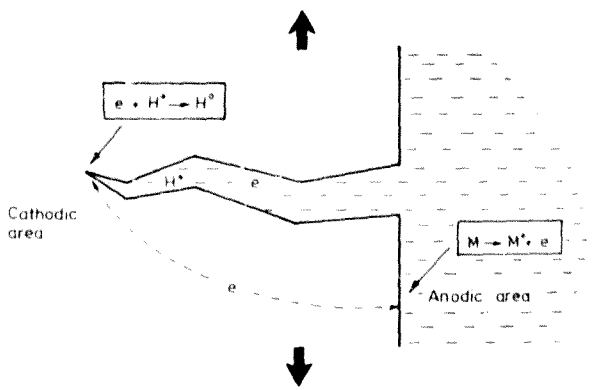

Figure 2.6: Schematic Illustration of the Hydrogen Embrittlement Model.

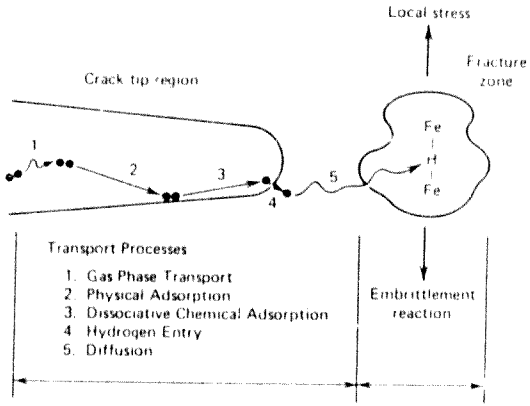

Figure 2.7: Schematic illustration of various sequential processes involved in embrittlement by external gaseous environments. Embrittlement reaction is depicted schematically by the iron-hydrogen-iron bond. Jones [29].

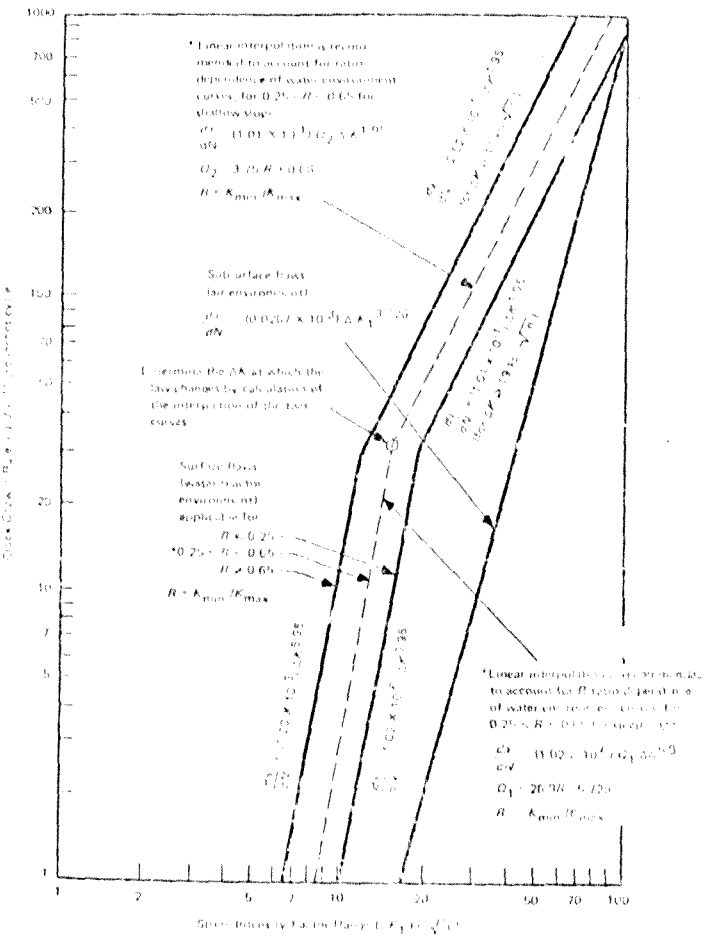

Figure 2.8: Reference Fatigue Crack Growth curves for Carbon and Low Alloy Ferritic Steels (ASME XI (1974)).

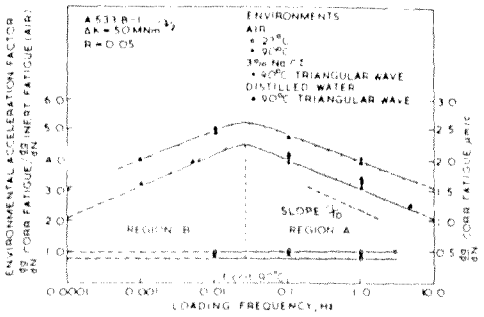

Figure 2.9: Effect of loading frequency on environmental acceleration factor for A533B-1 RPV Steel. Atkinson and Lindley [10].

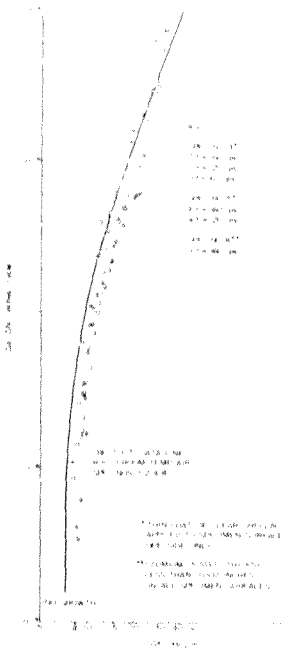

Figure 2.10: Fatigue-crack-propagation rates of ASTM A533B-1 steel in distilled water at ambient temperature, R=0.10 Paris et al [34].

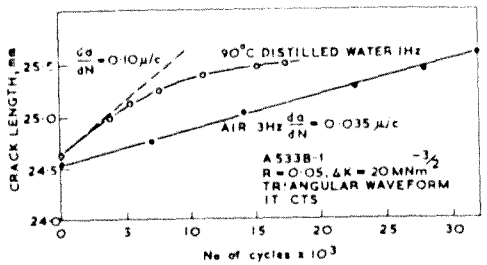

Figure 2.11: Comparison of fatigue crack growth rate in air and water at constant stress intensity. Note the retardation effect in water. Atkinson and Lindley [10]

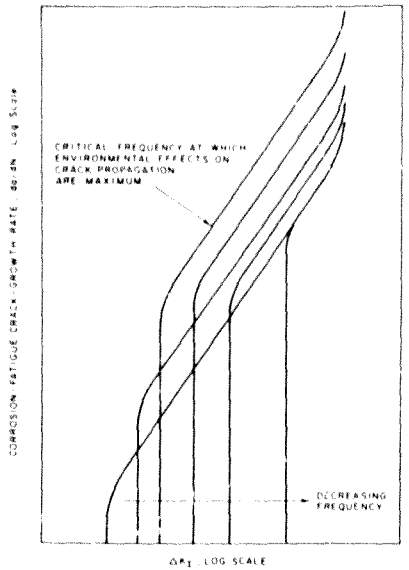

Figure 2.12: Schematic of idealized corrosion-fatigue behaviour as a function of cyclic-load frequency. Rolfe & Barsom [37].

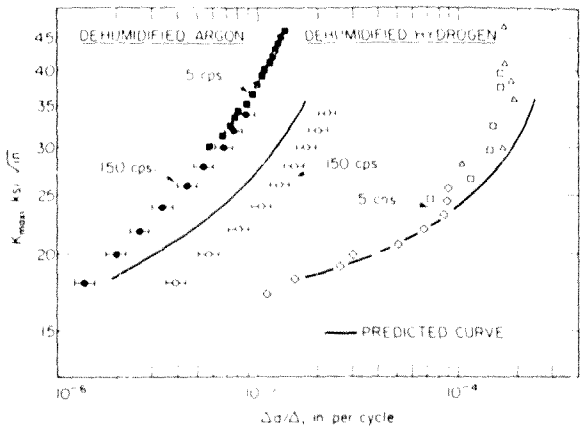

Figure 2.13: Application of superposition model to fatigue crack growth behaviour in 18Ni maraging steel tested in dehumidified argon and hydrogen. Wei and Landes [38]

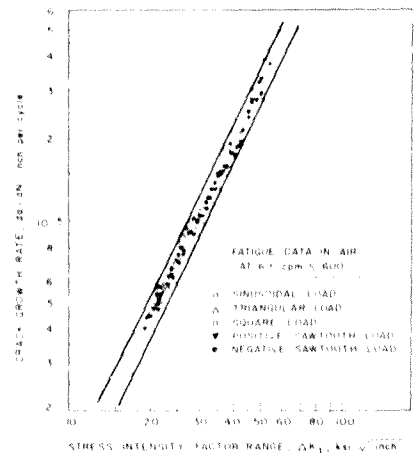

Figure 2.14: Fatigue crack growth rates in 12Ni-5Cr-3Mo steel under various cyclic stress fluctuations with different stress-time profiles. Barsom [39].

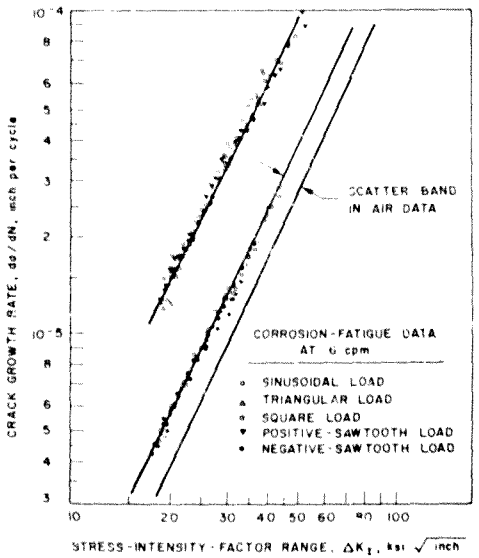

Figure 2.15: Corrosion-fatigue-crack growth rates in 12Ni-5Cr-3Mo steel in 3% solution of sodium chloride under various cyclic stress fluctuations with different stress-time profiles. Barsom [39].

Nominal Load Ratio, $R = K_{1min}/K_{1max}$

Baseline Stress Intensity Range, $\Delta K_B = K_{1max} - K_{1min}$

Overload Stress Intensity Range, $\Delta K_{OL} = K_{2max} - K_{1min}$

Overload Factor, $r_{OL} = K_{2max}/K_{1max}$

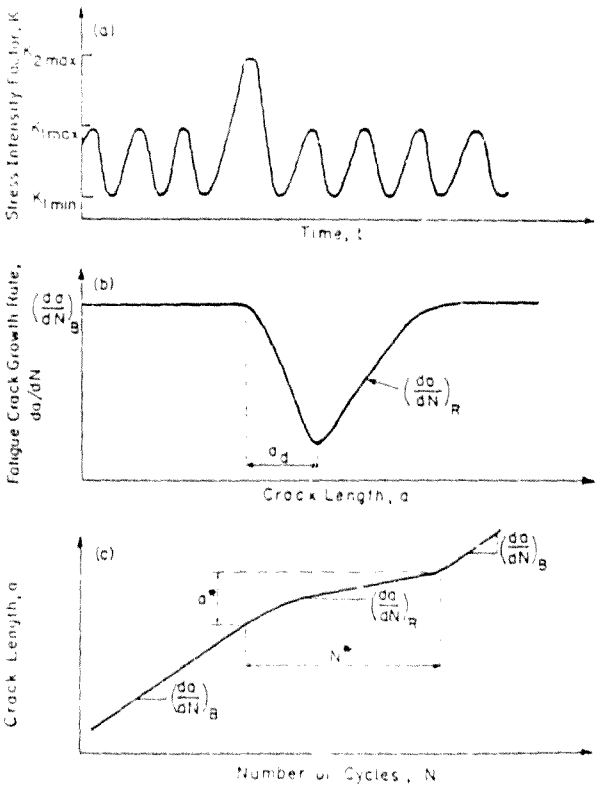

Figure 2.16: Schematic illustration showing the transient deceleration in growth rates during Mode I fatigue crack propagation resulting from the application of a single positive (spike) overload. Ritchie [61].

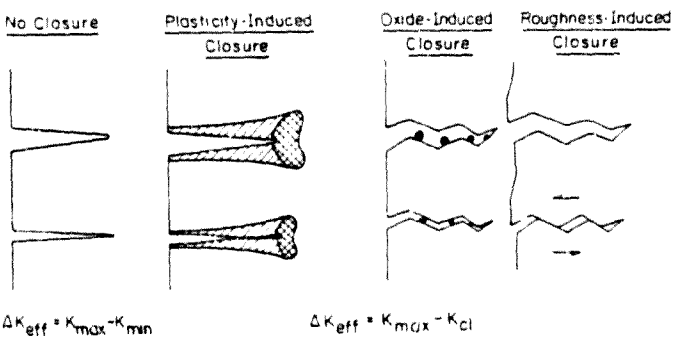

Figure 2.17: Schematic illustration of mechanisms of crack closure arising from plasticity, oxide-debris and fracture surface roughness. ΔK_{eff} is the effective stress intensity, given by the difference between the maximum stress intensity K_{max} and the stress intensity to cause closure of the crack K_{cl}. Pitchie [61].

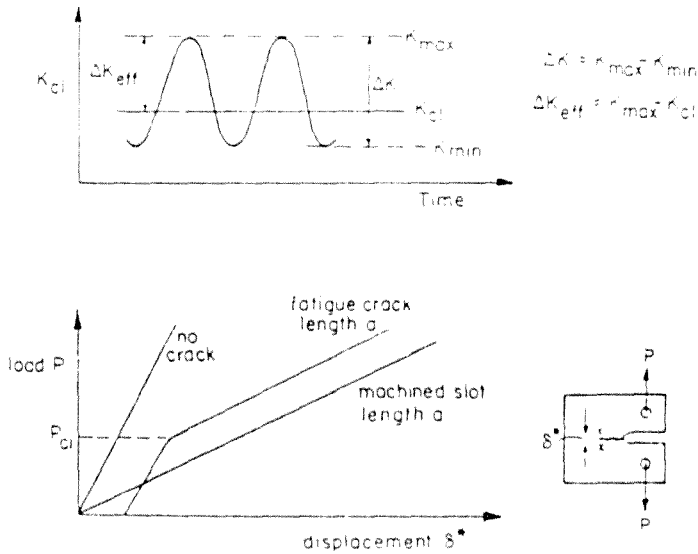

Figure 2.18: Elber's procedures for experimentally demonstrating plasticity-induced crack closure, showing elastic compliance curves for uncracked test-piece, test-piece containing a finite width slot of length a, and test-piece containing fatigue crack of length a. Note how fatigue cracked specimen does not appear to indicate presence of crack until above the closure load. Ritchie [61].

3 EXPERIMENTAL SYSTEMS

3.1 Testing System

3.1.1. E S H Servo-hydraulic Testing Machine

Fatigue testing was carried out on a 50kN capacity E.S.H. servo-hydraulic testing machine. In this system the load generated by the hydraulic actuator is measured by a strain-gauge dynamometer or load cell in series with the specimen. The signal from the load cell is amplified and compared in a differential amplifier with the desired signal obtained from the data input. The output of the differential amplifier is transmitted to a servo-valve which controls the actuator. This system thus forms a closed-loop control circuit (Figure 3.1). The loop may also be completed using a displacement transducer signal or a strain gauge signal from the specimen instead of from the load cell, if desired.

A very important advantage of these machines is the versatility of the system regarding the input signal which can be accepted. Virtually any analog signal, for example, from a function generator, random noise generator, magnetic tape or computer, can be used as input. Thus, not only constant amplitude waveforms or simple block programmes but also random waveforms, such as actual service recorded stress histories, can be accommodated. In particular, load transients typical of PWR start up or shut down could be employed. Specimens or components of specific materials can therefore be subjected to much more realistic fatigue testing than is possible in conventional machines.

In this project a waveform generator was used which could generate the input signal for the cyclic tests. It could generate different waveforms viz., sinusoidal, positive and negative sawtooth as well as square waveforms at frequencies ranging from 0.01 Hz to 50 Hz. Sinusoidal and positive sawtooth waveforms at frequencies of 0.1, 1 and 10 Hz were employed in the

present investigation.

3.1.2 Computer Control

As many of the tests were of long duration, (average duration approximately two weeks to one month), it was imperative that these tests be computer controlled. In the present study this was achieved with the use of a Commodore Pet microcomputer.

The Computer made it possible to control the tests using the function generator to generate the input signal of the required waveform and at the correct frequency. The input signal was then relayed through an interface unit to the ESH testing machine. This was simultaneously carried out while the computer was monitoring the feedback load signal from the ESH testing machine through the interface unit. Other functions performed by the computer either independently or simultaneously included; cycle monitoring, crack length monitoring and data logging in the form of both a constant print out as well as data storage on disk.

As a result of design constraints of the interface unit it was not possible to carry out computer controlled tests using the waveform generator for low frequency tests. This restriction was overcome by using the computer not only to control the test but also to generate the waveform signal at the appropriate frequency. This, however, meant that crack length monitoring could not be done constantly and simultaneously with the fatigue test. In some instances this did not prove to be a serious restriction, since fatigue testing was stopped so that the crack length could be measured after which testing was resumed.

3.1.3 Microcomputer Interface Unit

The microcomputer interface unit provides an interface between the analog input and output signals from the testing machine to the microcomputer. The various modules incorporated in the testing system are summarised overleaf, and the function and operation of each device is then fully detailed.

Module	Function	Purpose
ADC 12-8CH	Analog to digital converter	Measurement of analog voltages from transducers etc.
SC12	Signal Conditioner	Generation and processing of analog voltages. 1. A mean value of voltage. 2. The amplitude of external voltage is changed.
DAC8-4CH	Digital to analog converter	Generation of analog voltages for general purpose use
PS	Power supply	Power supply for modules
TIMER	Timer and bus terminator	Termination board for interface units, combined with a cycle counter

ADC 12-8CH

A 12 bit ADC with 8 differential input channels and containing a programmable gain instrumentation amplifier (PGIA) was used in this work.

The gain of the ADC12-8CH can be set under software control in the range 1,2,4 .... 2^i, ... 1024. The settling time for the different gains is automatically increased as the gain goes from 1 to 1024 to ensure reliable results. However, the measurement of very low voltages is inherently prone to errors, due to noise, earth loops, etc.

The input of the ADC12-8CH has been multiplexed to provide a choice of differential input channels. The differential inputs allow very good noise rejection to be realized.

SC12

In order to enable a microcomputer to perform complex functions it must also be able to provide an analog output that can be set by software. The normal control sequence would then be that the ADC12-8CH measures load or displacement, whereafter the microcomputer calculates a new control output which is finally used to drive the testing machine through the signal conditioning module. This module contains two digital to analog converters which, in combination, should be able to perform the majority of tasks required in control applications.

The 12 bit SC12 is provided with an input and output and performs the following basic functions.

1. An analog output can be operated by the microcomputer in the range -10.0 to 9.995V irrespective of the SC12's input.

2. Any constant or changing voltage in the range +10 to -10V can be supplied to the SC12's input, which is then attenuated by the microcomputer and the result provided at the output socket.

3. The functions 1 and 2 can also be summed, hence providing any combination of 1 and 2 above at the output. The output must remain in the range of +10 to -10V, however.

A typical example of an application of the SC12 is the conditioning of a sine wave with an output of 20V peak to peak, which is fed into the SC12's input socket. The microcomputer is able to vary the amplitude and mean components and produce it at the SC12's output socket.

DAC8 4CH

A four channel 8 bit digital to analog converter (DAC) provides the input voltage for variable power supplies, relay operation etc. No interface machine code software is required as BASIC statements can be used directly for 8 bit interfaces.

PS

The power supply provides +10 and + 20V potentials to the modules which contain their own regulators. A special switching system has been devised which prevents an already switched on unit switching itself on again after a power failure. This is a safety precaution as the interface will not have been initialised and the program in the microcomputer will not exist in the event of the power failure.

TIMER

This module serves two purposes

1. It provides a passive termination facility for the bus contained within the racking system to allow more reliable operation.

2. Circuitry is contained on the board which will count the number of pulses (eg. number of fatigue cycles).

The counting facility will count transitions which go from a value less than $-V_1$ to a value greater than V_2 volts, hereby ensuring that any noise within the band $-V_1$ to V_2 volts will not be counted. V_1 and V_2 can be individually set using two
present potentiometers within the unit. These potentiometers are normally set at -3V and 3V respectively.

The interface unit and the microcomputer are interconnected by means of two fifty way ribbon cables. This cable is terminated

at the microcomputers "memory bus" and at the BUS BOARD contained within the interface. The BUS BOARD contains transceivers which fully buffer the interface unit from the microcomputer. This ensures reliability as well as safety.

3.2 Environmental Circuit

3.2.1 PWR Water Circuit

The system was designed [1] to provide a simulated PWR environment in which low temperature (23- 90°C) and low pressure (approximately atmospheric pressure) corrosion fatigue testing could be carried out. The system consisted of the circuitry including tubing, valves, pumps etc., also with water chemistry conditioning and water storage facilities. Figure 3.2 is a flow diagram of the low temperature, low pressure loop and water conditioning unit.

Tap water is processed via filtration and de-ionization before being treated in an activated carbon resin bed, oxygen scavenger bed and a final polishing unit. The demineralized, deoxygenated water is then passed through a fine filter before entering the storage tank of 200 litre capacity. The system is a recirculatory one because, firstly the de-ionizer will not be able to cope with long periods of use without regular replacement of the cartridges, secondly, dosing chemicals will be lost to drain and finally there is a need to conserve water. When the water chemistry levels are not to specification the stored water will be discarded and a new batch made up.

The storage tank is fitted with a hydrogen gas bubbling tube to allow hydrogen to be bubbled through the water in order to keep the oxygen levels down. The hydrogen can be vented into the atmosphere via a pressure relief valve. The storage tank also has a dosing connection which permit dosing with boric acid and lithium hydroxide. After dosing is completed the oxygen level can be reduced by further hydrogen bubbling.

Low density polyethylene tubing was used instead of stainless

steel tubing since it was a cost effective way to experiment with the recirculating system. This also meant that low density steel tubing since it was a cost effective way to experiment with expensive stainless steel ones. All the valves and couplings were manufactured from brass or cadium plated brass. The financial saving, without a serious drop in technical requirements, fully justified the use of low density polyethylene tubing and brass fittings.

3.2.2 Water Conditioning

The water conditioning system consists of two treatment sections, a pretreatment consisting of filtration and de-ionization and then the final purification and filtration.

During the pretreatment stage, tap water is passed through a Sartobran capsule filter which has a 3μm absolute rating (i.e. 100% confidence that no material >3μm will pass through the filter).

The filter contains cellulose acetate filter material and has an operating temperature and pressure of 120°C and 4 bar respectively. A venting screw is situated in the filter housing to allow venting of any trapped gas in the filter. This filter not only removes the more massive particles in the water but also ensures prolonged life of the de-ionization and deoxygenation plant.

The prefiltered water then passes through a 28 l capacity mixed bed de-ionizer before entering the main purification section. This de-ionization cartridge serves to increase the ion removal capacity at a later stage and helps to reduce replacement of the final de-ionization cartridges.

The pretreated water then passes into a NANO pure II de-ionizer which produces type 1 grade water i.e. water having the following characteristics

Specific Conductance (micromhos, max)	Down to 0.05
Specific Resistance (Megohm, min)	Up to 18.3
Total matter (mg/l, max)	< 0.1
Silicate (mg/l, max)	< 0.01
Culture/Colony count	< 10.0

The NANO pure II system being used in the PWR corrosion fatigue work contains four cartridges. The first cartridge is a de-ionizer and contains a combination of granular activated carbon and virgin, macroreticular resin. It effectively removes colloids, bacteria, organics and chlorine. The second cartridge removes oxygen. A product of the reaction is the formation of SO^{2-} ions which are removed in cartridges No. 3 and No. 4. The third cartridge is a high capacity mixed bed de-ionizer and is used as a rougher in the four cartridge unit. It has more grain removal capacity than the fourth ultrapure cartridge, but to a lower purity level. The fourth ultrapure cartridge is also a mixed bed de-ionizer which can produce water with a resistivity up to 18.3 megohm.

After the demineralized water has passed through the cartridges it can be recirculated for further clean-up or it can be passed through a final 0.2 μm filter before being passed into the storage tank. The 0.2 μm filter is a pleated membrane filter that removes all bacteria and was radiation sterilized at the time of manufacture. This filter is consistent with the filter placed in the return line just before entry into the storage tank. These filters ensure that no material < 0.2 μm is allowed into the storage tank.

3.2.3 Recirculating system

The demineralized water in the storage tank is dosed with boric acid and lithium hydroxide in order to simulate environment conditions. Hydrogen is bubbled through the water to ensure that the oxygen level remains within specification (O_2 < ppb). The water in the storage tank can now be pump mixed via the diaphragm pumps. This recirculating loop has a sample point to allow water samples to be taken in order to ensure proper mixing. The design of all the return loops is such that the returning water cascades through the hydrogen blanket thus facilitating dissolved oxygen removal.

The main supply loop to the corrosion fatigue test cell is also pumped via a diaphragm pump with a maximum flowrate of 144 l/hr. This loop also contains a sampling point for chemical analysis checks and an inline oxygen meter for batch tests. A multiple valve system near the test cell allows specimen changes and subsequent hydrogen purging without allowing oxygen to leak into the system.

All the piping consists of low density polyethylene which has an oxygen permeability of 60×10^{-10} $cm^2/sec(cm\ Hg)$. Given a tube length of 50 m having an O.D. of 1/2" and an I.D. of 3/8" the oxygen leaking into 160 l of water over a period of six months will be 0,1 ppb. This amount can be regarded as negligible since the specification allows up to 100 ppb of dissolved oxygen.

3.2.4 Analytical Equipment

The water chemistry specifications drawn up by the ICCGR for testing in PWR type water is as follows:

Water Chemistry

Conductivity	< 20 μmho/cm
pH (room temperature)	6.5 ± 0.2
Dissolved O_2	< 5 ppb
Boron	1000 ppm
H_2	15 - 50 Std. cc/kg H_2O
Chloride	< 0.1 ppm
Fluoride	< 0.1 ppm

Conductivity

An Orion model 101 conductivity meter was used to measure the electrical conductance. Measurements could be made over a wide range (i.e. 0.001 μmho to 1 mho) using a variety of cells with an accuracy better than 1% full scale. When used with the appropriate percentage T coefficient and the sampling temperature controls the conductivity meter automatically converts the conductance to a reading taken at 25°C.

The Orion conductivity meter allows selection from three A.C. frequencies (3 kHz, 2 kHz and 80 Hz) permitting a choice of cell types. Commmon cells with platinized electrodes are calibrated at 1 kHz, therefore the most accurate conductance measurement will be made at the same frequency. The 3 kHz frequency should be used when working with special cells using steel electrodes. The 80 Hz frequency is recommended for conductance measurements at very low levels (of the order of μmhos). When operating at low levels, it is necessary to use cells with very small cell constants (0.1), which consequently have large capacitive effects. Table 3.1 shows examples of some conductivity measurements and recommended cell constants for the appropriate measuring frequencies. Table 3.2 is a cell and frequency selection chart for the model 101 conductivity meter.

High Sensitivity Dissolved Oxygen Detector

The sensor of the Orbisphere Model 2713 oxygen detector is the membrane enclosed polargraphic type. It senses the presence of

oxygen in the medium in contact with the membrane and passes a current, which is proportional to the concentration of the oxygen, to the measuring instrument. The instrument has a measurement range from 1 µg/l (1ppb) to 20 mg/l (20 ppm).

A flow chamber enables the sensor to be mounted in an air tight flow circuit, which allows continuous monitoring of the oxygen levels. Sample flow rates should be within the range of 50 cm^3/min to 250 cm^3/min while temperatures can range between 0 to 45°C. Sample pressures should be less than 20 bar.

Flame Emission Techniques for Boron and Lithium Determinations

Atomic spectra in the ultraviolet or visible region are produced by atomization of the sample, a process whereby the constituent molecules are decomposed and converted to gaseous elementary particles. Both the emission and the absorption spectra of an atomized element consist of relatively few discrete lines at wavelengths that are characteristic of the elements. As a result of the atomized state of the sample the temperature of a flame is sufficient to excite a small fraction of the monatomic particles (atoms and ions) to higher electronic states. Their return to the ground state is accompanied by the production of emission lines, which serve as a basis for flame emission spectroscopy. Here the location of the lines provides qualitative information and their intensity permits quantitative analysis.

In the case of Boron an acetylene-air flame was used with care being exercised to keep the background noise as small as possible. Boron, in contrast to most other elements, has no strong line that can be used for spectral emission analysis, thus the BO_2 system of bands between 450 and 600 µm was used which was sufficiently sensitive for analysis. The bands have no self-absorption, so that the calibration graphs are always linear. Lithium on the other hand, has resonance lines at 670.8 and 323.26 µm which are at a good distance from interfering lines making analysis somewhat easier.

Ion-Selective Measurement (pH, Cl^-, F^-)

The Philips PW 9416 Ion-Selective Analyser was used for all the ion-selective analysis and pH determinations. The following electrodes were purchased for ion determinations: (1) Combination pH electrode, (2) Pt resistance thermocouple, (3) Chloride ion-selective electrode with reference electrode and (4) Fluoride ion-selective electrode with reference electrode.

Calibration and measuring methods are simply outlined step by step on a visual display unit. Once the sensor has been calibrated the measurement parameters can be stored in permanent memory. Nine memories are available which are retained even when the instrument is turned off.

The ion-selective electrode senses the activity and thus the related concentration of the measured ion. The reference electrode provides a stable electrode potential and completes the electric circuit. The resultant potential difference is detected by the voltmeter and the concentration of the ion being measured is computed from the measured voltage. The resulting concentration appears on the screen but may also be printed out by the built-in printer. Printer format can be selected so that main parameters can also be printed out. If required, mean and standard deviation can be provided with each result. Thus the reproducibility and accuracy of any group of results can easily be checked.

Dissolved Hydrogen Gas

Hydrogen gas concentrations were estimated from published data given the temperature and the partial pressure of hydrogen in equilibrium with water. The overpressure range during testing was between 0 - 40 kPa also the temperature ranged between 20 - 25°C. Thus the calculated hydrogen concentrations ranged between 14.6 to 21.7 Std. cc/kg H_2O. The PWR specification for dissolved hydrogen is 0 - 50 Std. cc/kg H_2O, thus results were well within the specification.

Sulphate Concentrations (SO^{2-}_4)

Ion selective analysis proved not to be sensitive enough for the low sulphate concentration in the water. This then required very specialised techniques, which included carefully controlled evaporation to concentrate the solution. As a result samples of water were sent to Bergstrom and Bakker Analytical Laboratories to determine the sulphate concentrations.

3.3 Environmental Cell

An environmental cell was required in which tests could be performed in a simulated low temperature low pressure PWR environment. Since this environment had to be very strictly controlled the cell had to meet very stringent requirements. It had to be chemically inert and be able to contain fluids at constant temperatures in range from 20 - 96°C. Complete isolation of the environment was required to avoid any contamination of the circulating fluid. The ability to monitor crack growth remotely and the possibility of making optical crack length measurements was also a priority. Another important consideration was oxygen permeability through cell walls since (as described earlier) the oxygen concentrations must be maintained at very low levels.

Previously, a number of designs for an environmental cell were considered centering around a localised environment in the immediate vicinity of the crack. These designs were unsatisfactory since certain practical problems were encountered particularly leaks, thus a new cell was designed.

The new cell design was based on the idea of enclosing the entire specimen in the cell (Figure 3.3) and was constructed entirely from 12 mm thick perspex. This allowed all round visual observation and specimen access with good thermal insulation, was rigid enough to withstand the stresses of handling and those exerted during a fatigue test. It was also inert and thus could not contaminate the enclosed environment. All the seals were of an O-ring type which maintain a good static as well as dynamic

seal even at elevated temperatures and were also chemically inert to the environment. The design of the cell facilitated the ready passage of the current and potential leads. Access was also made for the fitting of a thermocouple inside the cell so that the temperature of the environment around the specimen could be accurately monitored. Sufficient space was provided for the addition of extra probes in the future, for example, reference electrodes for electrochemical potential as well as conductivity measurements and sampling facilities in further corrosion studies. Removable sides with O-ring seals meant that easy access was available for changing the specimens (Figure 3.4a and 3.4b).

One further constraint of the cell design was that it required leakproof passage of the current input leads to the specimen. Aluminium alloy rods were used which had, on the one hand, to be sufficiently thick to accommodate the high current density with neglible heating effects, and on the other to be sufficiently thin so as to be flexible during the fatigue test, so that the exit seals of these rods through the environmental cell were not impaired during large crack opening displacements. Reduction of the central portion of the rod from the original 4.5 mm to 3 mm diameter fulfilled the latter of these requirements, without seriously affecting the former.

3.4 Crack Length Measurement

Since good reproducibility of results is an important requirement much effort has been devoted to ensuring a highly stable system, especially in view of the fact that tests were, in some cases, to run for two to four weeks or more. An attempt was made to locate possible sources of errors with a view to reducing experimetal error. The potential drop system used to measure crack length can be divided into two sections, namely (a) the current producing circuit and (b) the recording equipment (Figure 3.5).

3.4.1 Power Supply

A Farnell Constant Current unit (Figure 3.6) providing a highly stabilized current was used. The output specifications are given in Table 3.3. Currently a one hour warm up period to stabilize output is being used.

In order to reduce any thermo-electric heating effects which could be transferred to the specimen, 50 amp welding cable was used as current leads. These were attached to the specimen by aluminium screwed connection (Figure 3.7). The electric heating of these connections was calculated for a 24 hour period and found to be negligible, (less than 1/13 watt).

The choice of current depended on two competing factors.

(a) increasing current input gives rise to increased measurability i.e. large output voltage.

(b) too large a current (typically exceeding 30 amps for a 12.7 mm steel CT specimen) leads to measurable specimen heating as a result of contact resistance at current input positions.

Thus the choice of current value depended on the resistivity of the material. In this project 20 amps was found to give good voltage output and minimal thermo-electrical heating effects.

3.4.2 Recording System

Probe wires for measurement of potential drop, typically about 0,2 mm diameter, were attached to wire-wrapping pins inserted in the specimens. These pins were inserted into 0,8 mm diameter holes drilled 2 mm either side of the notch centre, (Figure 3.7). The probe wires were then connected to a digital multimeter.

For the purposes of calibration, the voltage output was plotted against actual surface crack length measurement using an optical

(x7) travelling microscope.

Digital Multimeter

The digital multimeter had to fulfil two important requirements viz.;

(a) it had to have sufficiently high resolution in order to detect small changes in voltage (crack length) especially for small cracks i.e. at the start of crack growth.

(b) it had to be readily interfaced with a microcomputer for remote control and data logging.

The Fluke 8986OA Digital Multimeter is a fully guarded, microprocessor-controlled 5-1/2 digit, five function digital multimeter, which has a low DC voltage measuring range of ± 200 mV with a maximum resolution of 0.0005% of full scale (i.e. 1 μV on 200 mV range) with a 5-1/2 digit display. The IEEE-488 interface option enables connection of the digital multimeter to a micro computer through the IEEE standard-488 bus.

3.5 Argon Environmental System

This system was designed to produce an environment in which both the moisture and the oxygen levels were kept as low as possible. For this purpose, an ultra-high purity (i.e. 99.995%) argon gas was used the main impurities being:

oxygen	3 vpm
nitrogen	5 vpm
moisture	1 v
hydrocarbons	

Figure 3.8 is a diagrammatic of the argon system showing the oxygen and moisture removal arrangements.

Control of the gas flow was maintained by the fine argon

adjustment valve fitted to the gas cylinder. Finer adjustment of the flow rate was achieved by a flowmeter which gave flow rates from 0-25.1 l/min at a maximum pressure of one atmosphere.

An argon stream with a flow rate of 0.5 l/min was passed through an oxygen reduction column in order to reduce the oxygen level in the gas. This reduction column consisted of a glass column with a standard taper joint to allow for the insertion of the catalyst. A heating tape was wrapped around the outside of the glass column and connected to a Herastat temperature controller for the heating of the catalyst.

Oxygen removal from the argon gas was achieved by passing the gas through a bed of reactive metal or metal oxide, which was heated to 160°C to provide a reasonable reaction rate. In this case a copper catalyst R0-21 produced by BASF (Badische Aniline und Soda-Fabrik) was used. This catalyst is made in the form of small pellets and is supplied in the oxidized form. It is reduced by heating to a temperature of between 120 and 140°C in a gas stream. The temperature of the column should not exceed 200°C, or sintering of the copper will occur with a reduction in activity. The column of R0-21 catalyst will remove a volume of up to 4 litres of oxygen at room temperature. At 150°C the capacity is increased by a factor of 5.

After oxygen has been removed, the argon gas stream enters the moisture removal section after passing through a bubbler. For work at atmospheric pressure gas bubblers are placed in the argon inlet line and at the outlet of the system. They serve as visual indicators of gas flow, and the outlet bubbler also prevents diffusion of air back into the system. Any disparity in the two bubbling rates gives an indication of any gross leaks that may have occcurred in the system. The oxygen level in the argon gas was constantly monitored using the Orbisphere Model 2713 oxygen detector described earlier.

There are three primary methods for the removal of moisture from a gas stream viz.;

(i) low-temperature condensation

(ii) compression of the gas so that the partial pressure of water increases and condensation results, and

(iii) the use of drying agents.

These methods are sometimes combined to obtain high efficiency.

The effectiveness of the low temperature condensation method can be seen from the fact that the vapour pressure of ice at -90°C is 7×10^{-5} mm Hg while one of the better desiccants namely CaH_2 has an equilibrium water vapour pressure of 10^{-5} mm Hg. Also calcium hydride on reaction with water produces a fine, high volume powder which may clog the column. Furthermore, the reaction of this particular desiccant with water introduces hydrogen into the gas stream and under the present test conditions this was unacceptable.

The liquid nitrogen condensation method affords an excellent source of extremely dry gas because the vapour pressure of water at -196°C is about 10^{-23} mm Hg. However, the use of a liquid nitrogen trap for the removal of moisture from argon proved to be problematical, due to the fact that argon boils at -185,7°C and freezes at -189°C, thus liquid argon would freeze and block the capillary tube. In order to overcome this problem a liquid nitrogen and alcohol mixture was used, thereby maintaining a temperature in the range of -160 to -125°C. The lowering of the dewpoint led to a reduction of the moisture to less than 100 ppb.

The system was connected using Tygon tubing rather than rubber tubing since as can be seen from Table [illegible] Tygon (polyvinyl chloride) has a lower permeability to atmospheric gases than rubber. Coupled to this, Tygon tubing makes a very good seal with glass, is claimed to have a vapour pressure of 10^{-7} mm Hg at 21°C, and is also less susceptible to deterioration than most rubber tubing.

3.6 Summary

This chapter describes in detail some of the experimental systems used in this investigation. These include;

(i) the computer equipment for the control of the servo-hydraulic testing machine which make it possible to test continuously for extended periods of time,

(ii) the environmental circuits which provided the argon and PWR water environments to the required specifications,

(iii) the environmental cell within which the tests could be conducted and finally,

(iv) the crack length monitoring system which allowed for the accurate measurement of the cracks at predetermined intervals.

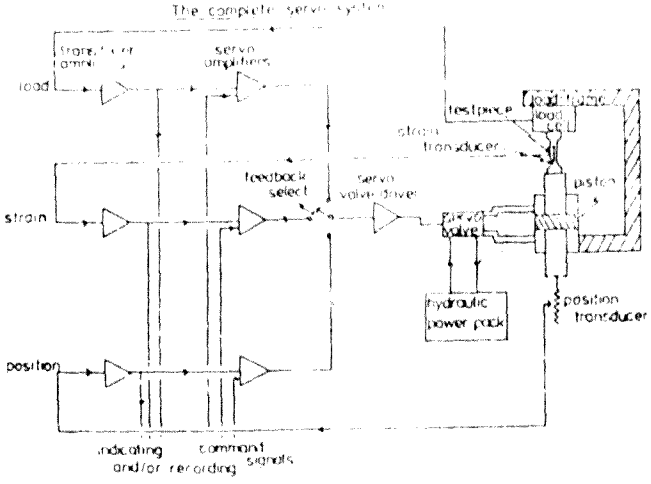

Figure 3.1: "Closed-loop" servo system for servo-controlled electro-hydraulic testing machine.

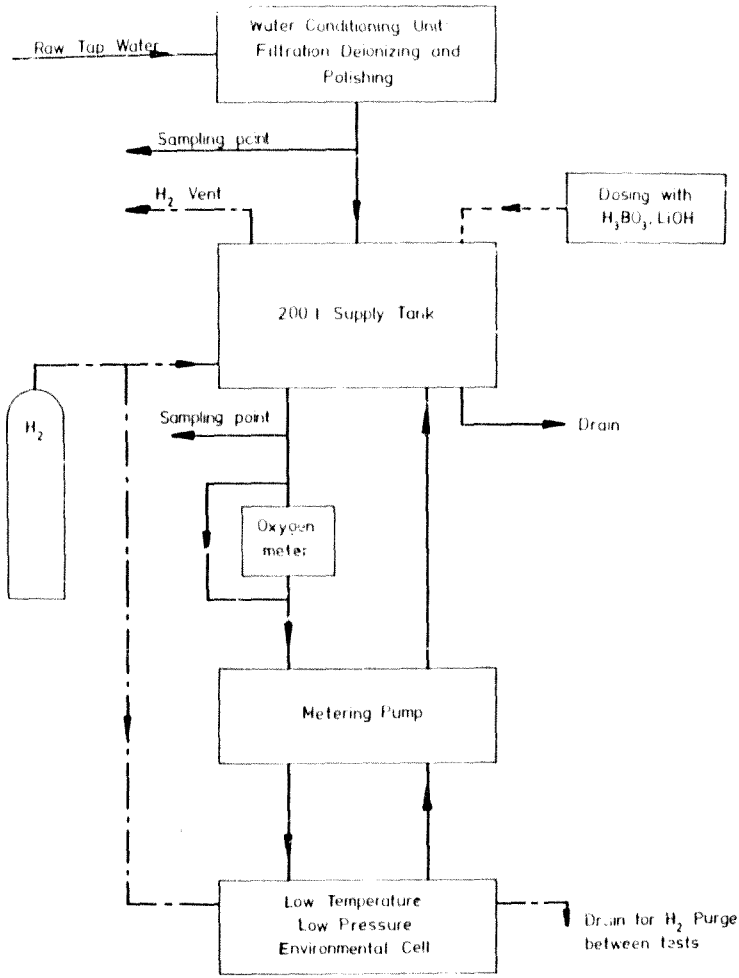

Figure 3.2: Flow diagram for low temperature - low pressure loop.

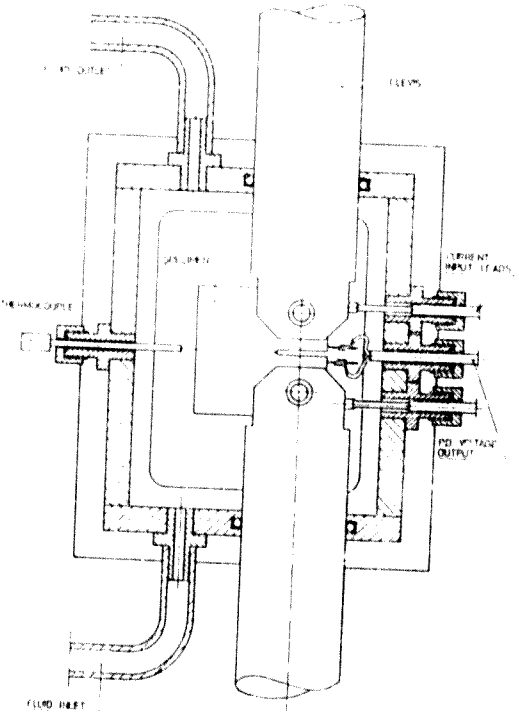

Figure 3.3: General arrangement of [illegible] rimental cell.

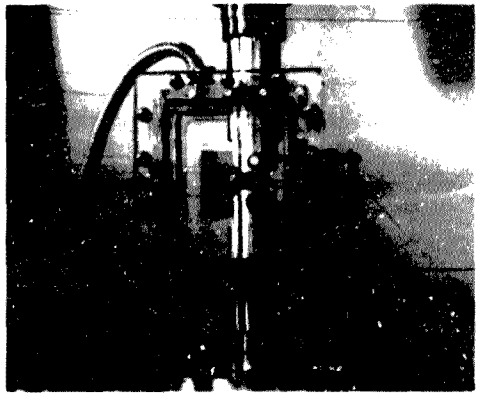

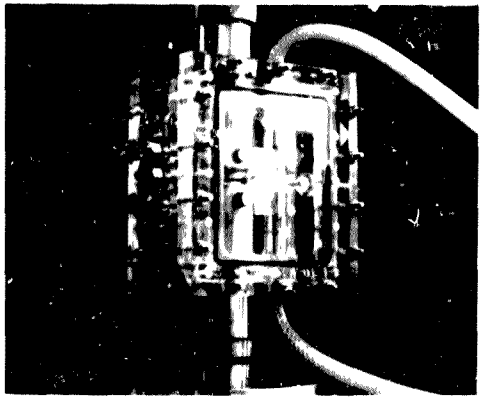

Figure 3.4 a & b Photo showing general arrangement of environment cell.

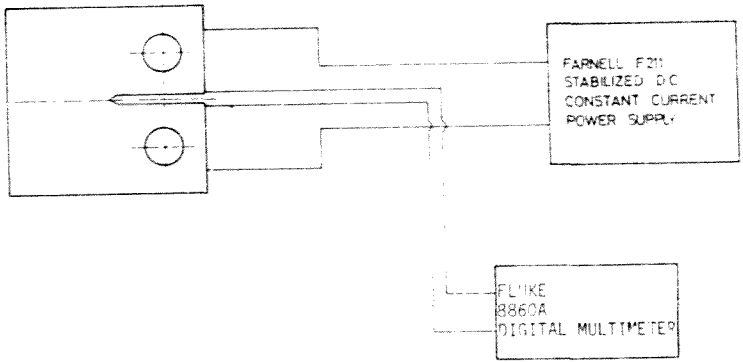

Figure 3.5 Schematic of crack monitoring system.

Figure 3.6 Farnell constant current supply system

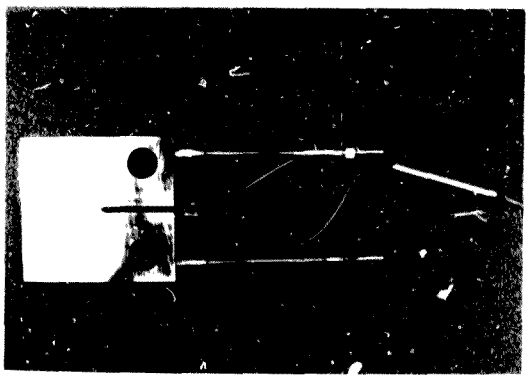

Figure 3.7: P.D. current and voltage connection leads.

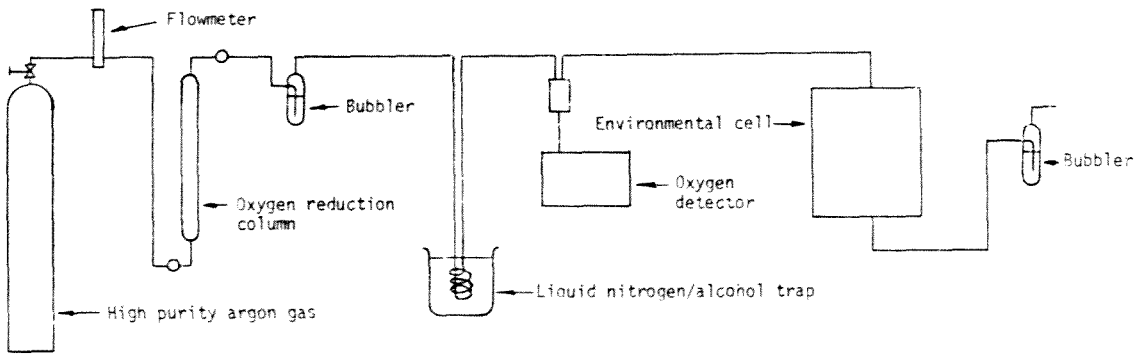

Figure 3.8: Schematic of argon environmental system.

TABLE 3.1

Resistivity	100,000,000	10,000,000	1,000,000	100,000	10,000	1,000	100	10	1	Ohm/cm
Conductivity	0,01	0,1	1	10	100	1,000	10,000	100,000	1,000,000	μS cm^{-1}
Example	Ultra pure water		Good distilled water		Good drinking water	0.01 % HCl			30 % H_2SO_4	
Cell constant	0,01	0,1	1		10					
Measuring frequency	Low frequency				High frequency				4 electrode measurement	

TABLE 3.2 Cell and frequency selection chart.

Range	Frequency (1)			Cell Constant		
	80 Hz	1 KHz	3 KHz	0.1	1.0	10
1 mho		X	X		X	X
100 mmho		X	X		X	X
10 mmho		X	X		X	X
1 mmho	X	X	X		X	
100 μmho	X	X	X	X	X	
10 μmho	X	display blanks	display blanks	X	X	
1 μmho	X			X	X	

NOTE: 3 KHz should be used with steel cells only.
Over-range is indicated by blinking of the display. When ranges 1 μmho and 10 μmho are selected only the frequency 80 Hz can operate. When 3 KHz or 1 KHz is selected there is no display.

TABLE 3.3 Farnell constant current unit specification.

SPECIFICATION

MAINS INPUT	A.C., Mains 210, 220, 230, 240V + 10% 49 - 400Hz 105, 110, 115, 120V by tap change
OUTPUT	Preset constant current
LINE REGULATION Output change for a + 10% Mains change	Less than 0.2% + 1mA
LOAD REGULATION Output change for a full range of load resistance	Less than 0.2% + 1mA
RIPPLE AND NOISE Content at full load	Less than 0.5% pk pk
TEMPERATURE COEFFICIENT Typical	0.01% per °C
AMBIENT TEMPERATURE RANGE For normal operation	10° to 40°C
STORAGE TEMPERATURE RANGE	-40°C to +85°C

TABLE 3.4 Permeability [illegible] for some polymeric materials.

Permeability Q [in 10^{-10} cm^3 sec (cm Hg)] for some common polymeric materials*

Polymer	Temp °C	H_2	O_2	N_2	CO_2	H_2O
Cellulose and cellulose derivatives						
Cellophane (cellulose acetate)	25		0.0021	0.00152	0.0017	47 160 000
Cellulose acetate, plasticized	21	4				
	25					11 000–15 000
	30		0.78	0.28	2.18	
Cellulose nitrate	25	1.7	1.95	0.12	2.23	
Ethylcellulose, plasticized	30		26.5	8.4	41.0	
Elastomers						
Natural rubber, vulcanized	25	48	23	7.0	140	2 800
Butadiene rubber, vulcanized	25	12	19.2	6.1	110	
Buna S, vulcanized	25	10	6	2.2	122	3 100
Buna N, vulcanized	25	10	4.8	1.0	91	6 100
Neoprene, vulcanized (poly-chloroprene)	25	11	4.0	1.2	25.8	910
Butyl rubber, vulcanized	25	7.2	3.3	0.5	5.3	
Hooker HS, vulcanized	25	1.6	0.4		2.1	4.1
Silicone rubber	30		91	1200	666	
Ethylene-propylene rubber	30		760		330	
Hydrocarbon polymers						
Teflon (polytetrafluoroethylene)	20				4.7	
	25					
Teflon FEP (tetrafluoroethylene hexafluoropropylene copolymer)	25		1.1	0.3	10	
Teflon TFE (tetrafluoroethylene trifluorochloroethylene)	25		0.010	0.005	0.21	0.01
Polyamides and polyesters						
Nylon 6 [poly(6 aminocaproic acid)]	20				0.058	
	25					40 4 000
	30		0.018	0.0005		
Nylon [poly(ethylene terephthalate)]	30		0.045	0.011	0.15	
	40					
Polycarbonate [poly(4,4'-isopropylidene diphenylene carbonate)]	25		1.4	0.4	8.0	
Olefin polymers						
Polyethylene, low density	25	440				21 60
	30		4.5	1.6	26.7	
Polyethylene, high density	30		0.54	0.18	3.1	
Polypropylene	30		2.3	0.44	9.2	
Polystyrene	25	1150				920 1 080
	30		1.1	0.29	8.8	
Polyvinylchloride	25					140 260
	30		0.4	0.13	1.1	
Saran [poly(vinylidene chloride-vinyl chloride)]	30		5×10^{-3}	2×10^{-3}	0.04	
Thiokol, plasticized, rubber-like	25					13 330
	30		0.54	0.14	1.4	
Acrylics						
Polymethylmethacrylate	25					1 000

4 EXPERIMENTAL PROCEDURE

4.1 Material Specification

The material used in this programme was SA 508 Grade B Class III forged steel used for the manufacture of nuclear pressure vessels. This steel was supplied by the Atomic Energy Commission, and was scrap material generated during the manufacture of a reactor pressure vessel. Tests [1] previously conducted in the department to fully characterise the chemical composition and the mechanical properties yielded the following data.

TABLE 4.1 Chemical Analysis

Element	Wt%
C	0.16
Mn	1.38
P	0.013
S	0.008
Si	0.25
Ni	0.77
Cu	0.06
Cr	0.26
Mo	0.52
V	0.013
Al	0.029
Sn	0.016
Co	0.021

Mechanical Properties

Yield strength	492.6 MPa
Tensile strength	625.8 MPa
Elongation	22.87 %
Reduction in Area	69.15 %
Hardness	227 VPN (30 kg load)
Charpy Toughness	268 J

4.2 Test Programme

The following test programme was undertaken.

(i) Corrosion Fatigue Test Matrix

	WAVEFORM				
	Sinusoidal			Pos. Sawtooth	
FREQUENCY (Hz) / R-RATIO / ENVIRONMENT	.1 .2	1 .2	10 .2	1 .2	10 .2
Argon		AR1	AR2	ARP1	ARP2
Air		A1	A2	APS1	APS2
PWR Water	W1	W2	W3	WPS1	WPS2

(ii) Variable Load Amplitude Test Matrix

WAVEFORM \ FREQUENCY / ENVIRONMENT	3 Hz Argon	3 Hz PWR	0.3 Hz PWR
Ripples	S1	S2	S9
Peaks	S3	S4	
Trapezoidals	S5	S6	
Spectrum	S7	S8	S10

4.3 Water Chemistry Control

After the PWR water test rig was assembled it was thoroughly cleaned to prevent contamination of the high purity water. The system was then filled with ultra pure demineralised, deoxygenated water and kept under hydrogen pressure. The water was then dosed with lithium hydroxide and boric acid through the dosing facility on top of the storage tank. The dosed water was thoroughly mixed by continuously circulating the water through the system via the pump while maintaining a constant flow of hydrogen through the tank. After approximately four hours the oxygen concentration was reduced to within specification (i.e. $[O_2] < 100$ ppb). Periodic checks confirmed that the water chemistry remained within specification for long periods of time. Indeed only after several months did the chloride level rise to above the specified level necessitating complete replacement of the water supply.

Prior to the commencement to each corrosion fatigue test, the environmental cell was purged with hydrogen to remove as much oxygen and contaminated water as possible. The cell was filled using the 30 kPa hydrogen pressure in the storage tank thus ensuring a gradual filling of the cell thereby preventing the

entrapment of hydrogen in the specimen starter notch. The water was circulated through the system via the recirculating pump at a flow rate of 26 l/hr. The corrosion fatigue test was then started.

On completion of the test the cell was emptied by forcing the PWR water back into the storage tank with the use of hydrogen over-pressure. The cell was then isolated from the rest of the system by a system of valves and the hydrogen pressure was relieved before the side covers were removed allowing for the removal and replacement of a test specimen.

4.4 Fatigue Testing

4.4.1 Prefatigue Cracking

Standard 1TCT compact tension specimens were prepared in accordance with B.S. 5447 (Figure 4.1). The specimens were then prefatigued in air to a length of approximately 3 mm from the starter notch. In order to expedite crack initiation, especially with high R-ratio tests, higher loads were initially used and were later stepped down to meet the test load requirement. To avert the transient effects of larger plastic zone size due to the larger loads, prefatigue cracking was only terminated after sufficient measurable crack extension had occurred.

4.4.2 Visual Crack Length Measurement

Fatigue crack length measurements were made as a function of elapsed cycles by means of visual and potential drop techniques. To facilitate accurate visual measurement; (i) the test area of the specimen was polished and indirect lighting used to aid crack observation and (ii) all measurements were conducted while the specimen was subjected to the mean load. Visual measurements were made using a low power (x 7) travelling microscope having an instrument resolution of 0.01 mm. These measurements were made at regular cycle intervals which were reduced as the crack growth rate increased.

4.4.3 Crack Curvature Correction

As a result of crack front bowing any surface crack length measurement will not accurately reflect the true length of the crack. Thus, in order to obtain a more accurate crack length measurement a crack curvature correction factor was applied to all surface crack length measurements. This crack curvature correction factor was obtained by producing beach marks on the fracture surface as a result of varying the minimum applied load, P_{min}, while keeping the maximum load, P_{max}, constant (i.e. varying the R-ratio). Alternate regions of 0.1 and 0.6 R-ratio crack growth were therefore visible on the fracture surface. A seven point through-thickness average crack length was then calculated. The ratio of the average through thickness crack length and the corresponding surface measured crack length recorded during the test being the crack curvature correction factor.

4.4.4 Calibration of the Potential Drop Technique

Potential difference measurements were made at fixed points across the crack for various crack lengths. These potential measurements can then be directly related to the curvature corrected crack length using Johnson's analytical solution [62] to Laplace's electrical potential equation,

$$a = \frac{2W}{\pi} \cos^{-1} \frac{\cosh(\pi/2W)}{\cosh\{(V/V_o)\cosh(\pi y/2W)/\cos(\pi a_o/2W)\}}$$

where V_o,V and a_o,a denote the initial and the actual measured values of potential and crack length, respectively, and $2y$ is the distance between the potential probes and W is the specimen width.

Due to crack curvature and short circuiting resulting from crack closure effects, Johnson's equation was found to consistently

underestimate the crack length and this was especially noticeable at longer crack lengths. Because of this underestimation of the crack length the following calibration procedure was followed. A least squares linear regression was taken of the corresponding curvature corrected crack lengths and the Johnson's estimate of the crack length. The Johnson's estimate of the crack length would thus be corrected by multiplication and addition of the appropriate regression constants, with the result that the crack length was reliably measured at all stages using the P.D. technique.

4.5 Computer Control and Data Logging

The original computer control system of the E.S.H. testing machine was designed for medium frequency testing. (This system consists of a microcomputer interface unit which allows the use of a function generator to provide the input signal to the E.S.H. testing machine and thus allows the computer to constantly monitor and maintain the fatigue loads at the preset frequency. This function can be carried out while simultaneously reading and storing the experimental data). Thus, the analog to digital converter has design limitations which prevent it from sending a signal, from the function generator to the E.S.H. testing machine, for frequencies lower than 10 Hz. As the frequencies required for this project are all essentially low frequencies (i.e. < 10Hz) this represented a serious restriction in that it firstly prevents continuous and simultaneous monitoring of the crack length and control of the E.S.H. machine. Secondly it means that either the E.S.H. is manually operated or the computer is used to generate the appropriate fatigue signal and frequency thus giving limited data reading and storing capability.

The last alternative while giving some computer control, does not allow for the simultaneous control of the E.S.H. machine and crack length reading. This means in fact that the E.S.H. testing machine actually has to stop fatigue testing in order for a crack length measurement to be taken. Fortunately the duration of the reading and storing operation was very short, of the order of 30

seconds. Since many of the tests ran for several days, computer control and data recording was considered vital. Also the load spectrum for the variable amplitude tests could not be generated by the function generator and could only be generated by the computer. Computer software was therefore designed to use the system in this mode of operation.

A flowchart of the programmes is provided in Figure 4.2 and listings are in Appendix 1. The programme first required the computer to initialize all the peripherals (i.e. digital to analog converter, fluke digital multimeter, disc drive and printer). All the relevant data (e.g. specimen dimensions, loads, frequency of crack length readings etc.,) were then manually entered. Some of this basic data (e.g. loads, frequency, etc.) would be checked against preset limits if inadvertantly the wrong values were entered, the programme will abort and will have to be restarted. After the correct data had been entered, the programme commenced the waveform and frequency generation and the resultant signal was relayed to the E.S.H. machine via the digital to analog converter. For the purposes of the this project the sine, positive sawtooth and spectrum load waveforms were generated at frequencies of 10, 3, 1 and 0.1 Hz.

At the required cycle interval the programme exited the waveform and frequency generation loop and entered the data reading and storage loop. The computer now addressed the Fluke digital multimeter and took several voltage readings, to allow for the voltage to stabilize. The voltage was converted to a crack length using Johnson's equation which together with the elapsed number of cycles were stored on disc and recorded at the printer. The programme re-entered the waveform and frequency generation loop and repeated this process until the final number of cycles had been reached, or the crack length reached a preset limit. At this stage the programme allowed for a review of the input data and new limits for data reading interval and fatigue testing could be set. At the completion of the test the load was ramped down and the peripherals were closed.

4.6 Data Reduction Technique

After obtaining the fatigue crack growth data, that is, Johnson crack length versus elapsed cycles, it was processed into the standard form of fatigue crack growth rate versus the stress intensity range. In order to remove some of the scatter in the experimental data it was numerically smoothed using the incremental polynomial method. The data reduction programme, flowchart provided in Figure 4.3, therefore incorporated both these functions as well as plotting the graphs of da/dN vs. ΔK on a log-log scale.

The Johnson crack length was manually corrected for both underestimation and crack curvature and then stored on disc. This operation can be included into the data reduction programme by adding a linear regression subroutine to the programme. The programme first smoothed the crack length values using the incremental polynomial method and then calculated the crack growth rate, da/dN and the stress intensity range, ΔK using the following expressions;

$$\Delta K = \frac{\Delta P Y}{B W^{\frac{1}{2}}}$$

where ΔP is the fatigue load range,

B is the specimen thickness, and

W is the specimen width.

The compliance function, Y, is given by

$$Y = 29.6\left(\frac{a}{W}\right)^{1/2} - 185.5\left(\frac{a}{W}\right)^{3/2} + 655.7\left(\frac{a}{W}\right)^{5/2} - 1017\left(\frac{a}{W}\right)^{7/2} + 638.9\left(\frac{a}{W}\right)^{9/2}$$

where a is the smoothed curvature corrected crack length.

Incremental Polynomial Method

This method for computing da/dN involves fitting a second-order polynomial to sets of seven successive data points. The form of the equation for the local fit is as follows:

$$a = b_o + b_1\left(\frac{N - C_1}{C_2}\right) + b_2\left(\frac{N - C_1}{C_2}\right)^2$$

where b_o, b_1 and b_2 are the regression parameters that are determined by the least squares method (that is, to minimize the square of the deviation between observed and fitted values of crack length) over the range

$$a_{i-3} \leq a \leq a_{i+3}$$

The parameters

$$C_1 = \frac{1}{2}(N_{i-3} + N_{i+3})$$

$$C_2 = \frac{1}{2}(N_{i-3} + N_{i+3})$$

are used to scale the input data, thus avoiding numerical difficulties in determining the regression parameters. The rate of crack growth at N_i is obtained from the derivative of the

above parabola, which is given by the following expression:

$$\frac{da}{dN} = \frac{b_1}{c_2} + \frac{2b_2}{c_2^2} (N_i - c_1)$$

The calculated values of stress intensity range and crack growth rate were then plotted on a log-log scale while a printout of the number of cycles, smoothed crack length, ΔK and da/dN values was produced.

4.7 Variable Amplitude Loading

At the 1983 International Cyclic Crack Growth Rate (ICCGR) Group meeting Scott [63] suggested a spectrum load sequence for a corrosion fatigue experiment in PWR or BWR primary coolant. This spectrum sequence was based on a simplified sequence of three different types of stress cycle, A, B and C, with R-ratios of 0.2, 0.7 and 0.9 respectively as shown in Figure 4.4. The magnitudes of the stress cycles and number of occurrences were so adjusted so that when applied to a two inch thick compact tension (2T CT) specimen, large differences in the crack extension would be obvious depending on which type of corrosion fatigue behaviour (e.g. plateaux or not) was observed.

Due to the lengthy testing time, of the order of 8 months for a 100 block sequence, it was decided to run a dry fatigue test to validate a revised dry fatigue crack growth equation likely to emerge from the Electric Power Research Institute (EPRI) database. In the case of a dry test, where no environmental effects are prevalent, high frequencies could be employed and the test duration reduced. The spectrum used in the present study is the same as that given previously (Figure 4.4) but with the cyclic periods adjusted to give a less time consuming experiment.

Since in the present study the spectrum load sequence was to be applied to 1T CT specimen the loads were recalculated ensuring that the stress intensities remained the same as for those calculated for the 2T CT specimens. Details of the specification

for each transient A, B and C for both 2T and 1T CT specimens are given in Table 4.1.

A computer programme (listing in Appendix) was designed to generate the spectrum loading sequence. The computer generated spectrum loading sequence used in the present study had the cyclic frequency increased by a factor of 3 (i.e. cyclic frequency of 3 Hz rather than 1 Hz). The increased frequency was not expected to invalidate the results since in a dry environment no frequency effects were expected. Dehumidified, high purity argon gas was used as the dry environment.

To assist with the interpretation of the results, with respect to the contribution of each of the different components of the spectrum sequence to the crack growth rate, the spectrum was divided into its various components (Figure 4.5). The computer programme was modified accordingly and tests were conducted using the various components of the spectrum as well as the spectrum itself. Before these tests were commenced the test specimens were prefatigued in air, initially a R-ratio of 0.2 was applied to initiate the fatigue crack and thereafter the R-ratio was increased in steps until a R-ratio of 0.9 was attained. Care was exercised that the magnitude of the load change did not cause crack arrest and the load was only changed after a reasonable amount of crack growth had occurred. The specimens were prefatigued to a crack length of 19 mm with the last 0.5 mm of crack growth at the R-ratio of 0.9.

4.8 Argon System

The production of dry, low oxygen argon gas required two start up procedures. Firstly, the heating tape around the oxygen reduction column was switched on and the temperature monitored by means of a thermometer inside the column. While the temperature continued to rise to the operating temperature of 160°C a constant flow of argon was required to displace as much of the oxygen in the system as possible.

Secondly, the stainless steel capillary coil of the nitrogen trap

was heated over a bunsen burner to ensure the removal of as much moisture which had been adsorbed onto the tubing as possible. A constant gas stream through the capillary tube not only ensures removal of the moisture but also prevents further moisture adsorption. After heating the tube for approximately 5 - 10 minutes the capillary tube was allowed to cool before being immersion in alcohol. Care should be exercised that the temperature difference is not too great since the lower temperatures will cause contraction of the gas with the consequent rapid suction of the medical paraffin, in the bubbler, through the tubing. The higher temperature on the other hand will cause a rapid expansion of the gas blowing the medical paraffin into the oxygen removal column.

Once the coil has been immersed in alcohol liquid nitrogen was added until the temperature has dropped to approximately -150°C. When the temperature reached -100°C more liquid nitrogen was added to bring the temperature down to the appropriate level. When the oxygen level on the Orbisphere oxygen detector had dropped to less than 1 ppb the fatigue test was started. Using these techniques, oxygen levels of less than 1.0 ppb and calculated moisture levels of less than 100 ppb, were achieved.

4.9 Summary

The chapter deals with the experimental techniques employed to produce PWR water with the correct water chemistry as well as the procedures followed to ensure accurate P.D. voltage measurement and its subsequent conversion to an average crack length with allowances made for crack front bowing. The computer programme used for computer control of the fatigue testing machine as well as data reduction and plotting routines were also fully described. The origin of variable amplitude loading sequence used in this investigation and its break down into simpler loading sequences to facilitate with the interpretation of the results is also explained.

Table 4.1 Proposed simplified spectrum of loads.

Transient	No/block	Period of rising load	R	Load Range (kN) for a 50mm CT specimen (Mean load for B&C is 120 kN)	Load Range (kN) for a 25mm CT specimen (Mean load for B&C is 42 kN)
A	1	1 sec	0.2	96.00	33.6
B	30	0.5 sec	0.7	42.53	14.88
C	1500	0.5 sec	0.9	12.63	4.46

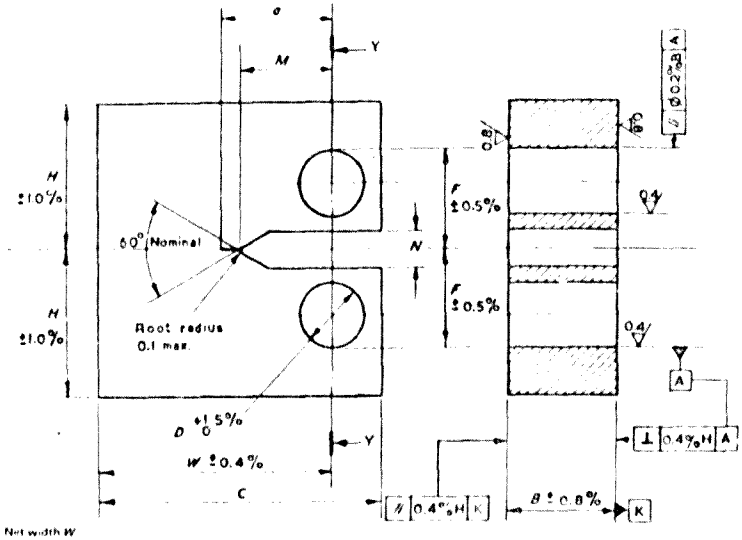

Net width *W*	
Total width *C*	1.25*W* min
Thickness *B*	^ 5*W*
Half height *H*	0.6*W*
Hole diameter *D*	0.25*W*
Half distance between hole outer edges *F*	1.6*D*
Notch width *N*	0.065*W* max
Effective notch length *M*	0.25*W* to 0.40*W*
Effective crack length *a*	0.45*W* to 0.55*W*

All dimensions are in millimetres

Figure 4.1: B.S. 5447 Compact Tension Specimens.

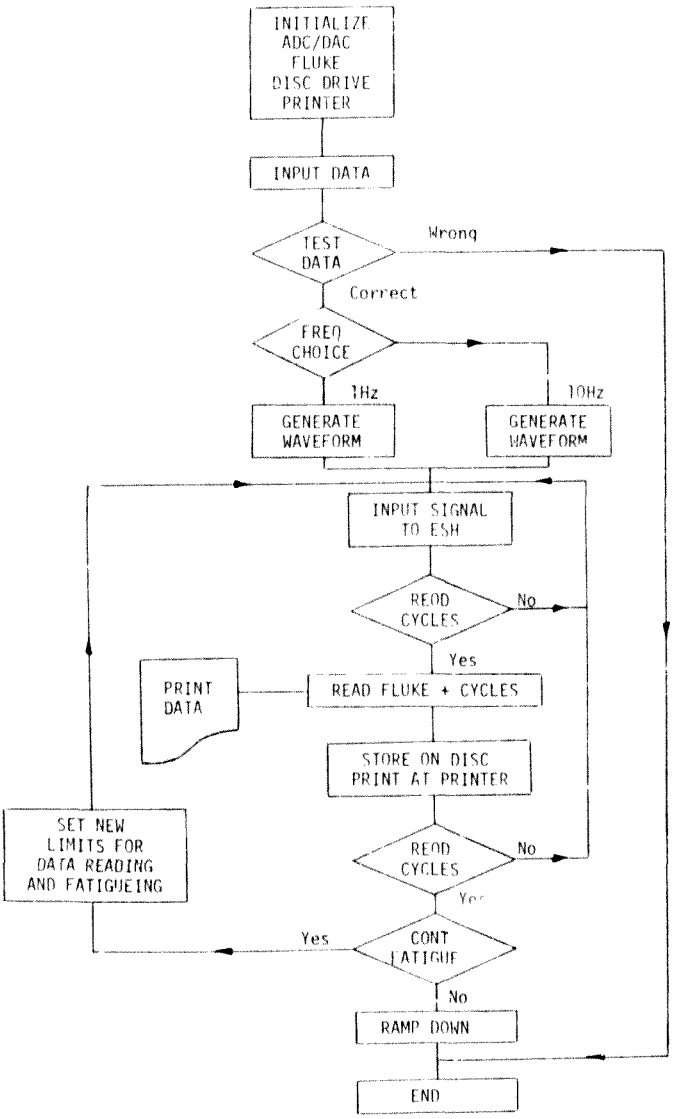

Figure 4.2: Flow chart for fatigue testing programmes.

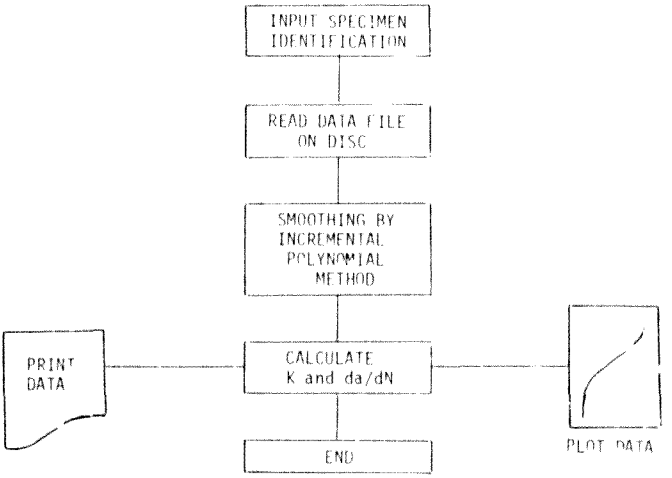

Figure 4.3: Flow chart for data reduction programme.

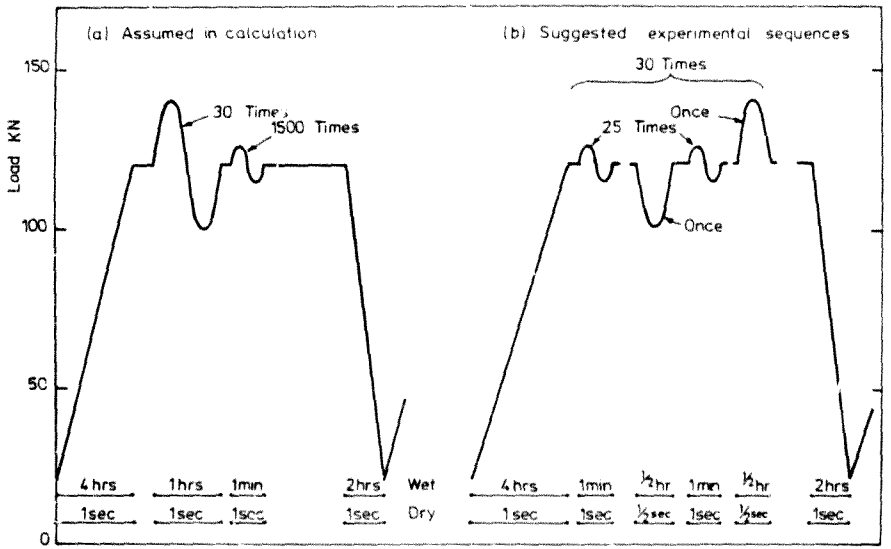

Figure 4.4: Scott's proposed spectrum loading sequence

SPECTRUM LOADING

Cycles per block

Transient A (R=0.2)	1
Transient B (R=0.7)	30
Transient C (R=0.9)	1500

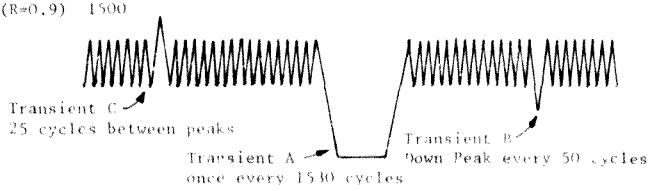

TRAPEZOIDALS

Cycles per block

Transient C	1500
Transient A	1

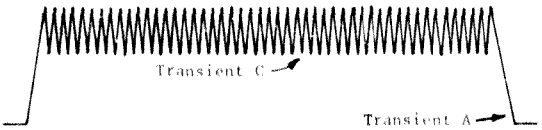

PEAKS

Cycles per block

Up Peaks	30
Down Peaks	30
Transient C	1500

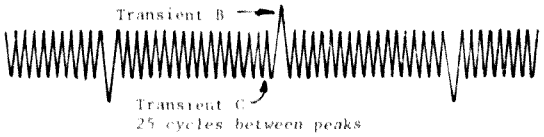

RIPPLES

Cycles per block

Transient C 1500

Figure 4.5: Schematic of various loading schedules adopted in the present study.

5 RESULTS

5.1 Crack Growth Rate Data

5.1.1 Constant Amplitude Loading

5.1.1.1 Environment

The effect of environment on fatigue crack growth behaviour for a frequency of 10 Hz, R ~ 0.2 using sine wave loading is illustrated in Figure 5.1. These tests show that at ΔK levels below 30 MPa$\sqrt{m}$ PWR water gives about 3 times faster crack growth rates than argon, however, at ΔK levels between 40 and 50 MPa$\sqrt{m}$ there is little difference in the fatigue behaviour. The air and argon data lie below the ASME XI (1974) dry line and agree well with the 1 Hz data while the PWR water data resides slightly above this data. The 0.2 R-ratio 1 Hz sine waveform data is shown in Figure 5.2 where it is evident that the air and argon data lie below the ASME XI (1974) dry line while PWR water gives crack growth rates that are consistently about 5 times faster than argon but reside on the ASME dry line. The effect of decreasing frequency from 10 Hz to 1 Hz increases the growth rate by a factor of 2.

The effect of environment using positive sawtooth waveform is shown in Figures 5.3 and 5.4. In Figure 5.3, tests conducted at 1 Hz using positive sawtooth waveform show that below 40MPa$\sqrt{m}$ argon growth rates are 2 times slower than both the air and PWR water crack growth rates which reside together approximately on the ASME XI (1974) dry line.

In the case of the 1 Hz test using positive sawtooth waveform (Figure 5.4) at ΔK levels below 40MPa$\sqrt{m}$ the air growth data is about 1.5 times faster than crack growth rates in argon, while PWR water growth rates are 2 times faster than those recorded for argon. At ΔK levels above 50 MPa$\sqrt{m}$ the data tend to merge together, while at ΔK levels below 30 MPa$\sqrt{m}$ PWR water gives

growth rates that are between 2 and 3 times faster than the argon data.

The effect of environment at 10 Hz tends to be slightly greater for the positive sawtooth than the sine wave, while at a frequency of 1 Hz the effect for both waveforms is about the same. Only the positive sawtooth crack growth data at 1 Hz, however, exhibit any real measurable EAC growth inasmuch that the data resides above the ASME XI (1974) dry line at ΔK levels above 35 MPa$\sqrt{m}$.

5.1.1.2 Frequency

The results of the effect of frequency on fatigue crack growth rates in argon utilising a sinusoidal waveform are illustrated in Figure 5.5. From this Figure it can be seen that there is little effect of frequency on fatigue crack growth. The present data resides below the ASME XI (1974) dry line, which represents an upper bound to crack propagation data for SA 533 B and SA 508 steels in air. No effect of frequency was observed for tests conducted in argon using a positive sawtooth waveform (Figure 5.6). This data also resided below the ASME XI (1974) dry line.

Tests conducted in an air environment for both sine and positive sawtooth waveforms (Figure 5.7 and 5.8) show little effect of frequency within the ΔK range tested. In the case of the sine wave (Figure 5.7) the data resides well below the ASME XI (1974) dry line while for the positive sawtooth (Figure 5.8) the data resides on the ASME dry line.

The PWR water tests in Figure 5.9 show that reducing the frequency from 10 Hz to 1 Hz increases the growth rate consistently by a factor of 2 at ΔK levels above 30 MPa$\sqrt{m}$, while reducing the frequency from 10 Hz to 0.1 Hz increases the growth rate by a factor of 4 at a ΔK level of ~25MPa$\sqrt{m}$. However with increasing ΔK level both sets of data converge and at a ΔK level of ~40MPa$\sqrt{m}$ both exhibit air growth rates of ~4 x 10^{-7} m/cycle. The 0.1 Hz frequency data exhibits classic environmentally assisted crack (EAC) growth behaviour inasmuch that a growth rate

plateau is evident which resides well above the ASME air line at low ΔK levels. Growth rate plateaux by their very nature exhibit a constant growth rate that is insensitive to ΔK level.

For the positive sawtooth waveform in PWR water (Figure 5.10), there is an increase by a factor of 2 in crack growth rate at ΔK levels lower than 45 MPa√m. Above this ΔK value the 1 Hz and 10 Hz data tend to merge together.

The only significant effect of frequency was found in PWR water when the test frequency was decreased from 10 Hz to 0.1 Hz. This particular result agrees well with the data reported by Atkinson and Lindley [10] which showed that the maximum environmental effects in a water environment occurred at a frequency of ~ 0.05 Hz and predicts the significant environmental effects observed in the present study on reducing the frequency from 10 to 0.1 Hz.

5.1.1.3 Waveform

Tests conducted in argon at frequencies of 10 Hz and 1 Hz (see Figure 5.11 and 5.12) indicate that at 10 Hz there is little difference between the sine and the positive sawtooth waveform. At a frequency of 1 Hz, however, there is a slight effect of waveform viz., crack growth rates are about 1.3 times faster for positive sawtooth than for sine wave.

In air (Figure 5.13 and 5.14) positive sawtooth waveform consistantly gave faster crack growth rates than sine wave. At a frequency of 10 Hz the crack growth rate was 2 times faster than the growth rate for sine wave while at 1 Hz it was 1.5 times faster. Surprisingly, in PWR water (Figure 5.15 and 5.16) waveform effects tended to be more evident in the 10Hz data than in the 1 Hz with crack growth rates for positive sawtooth waveform being 1.5 times faster than sine wave at 10 Hz.

Generally, positive sawtooth waveform data exhibited crack growth rates that are approximately 2 times faster than the sine wave data. In argon waveform effects are evident only at a frequency of 1 Hz while in PWR water waveform effects are only evident at

10 Hz. In air waveform effects are observed at both frequencies.

5.1.1.4 High R-Ratio Tests

3 Hz Argon Tests

The results of the Transient C (R = 0.9) test (Table 5.1) with a final crack growth rate of 2×10^{-7} mm/cycle represents a near threshold condition for SA 508 cl III RPV steel in an argon environment i.e. $\Delta K_{th} \sim 5$ MPa/m. This crack growth rate data point together with the R = 0.2 data from the present study and relevant argon data reported by Bulloch and Buchanan [64] are illustrated in Figure 5.17. (The steel used by Bulloch and Buchanan was Ducol W30 which has a similar chemical composition to SA 508 and is used for pressure vessels in conventional coal fired power stations).

It can be seen that the near threshold data for the Ducol steel agrees well with the near threshold growth data point for the present investigation. Further an extrapolation from Bulloch and Buchanan's R = 0.9 argon data to the R = 0.2 argon data also shows excellent agreement. It is important to note that both the present data as well as the R = 0.2 data does not exceed the ASME XI upperbound for fatigue crack growth rate in an air environment. Bulloch and Buchanan's data [64] however resides below the ASME XI dry code line for ΔK levels < 7 MPa/m which reflects the conservative nature of this code line at near threshold levels.

3 Hz PWR Water Tests

After 500 blocks the fatigue crack had reached an average growth rate of 6.5×10^{-7} mm/cycle which again represents near threshold fatigue crack growth behaviour (i.e. $< 10^{-6}$ mm/cycle). In order to obtain further data points the R = 0.9 test was allowed to continue after the 500 blocks were completed. This then generated corrosion fatigue crack growth data over a range of ΔK levels and this data is illustrated together with the R = 0.2 PWR water data in Figure 5.18. It can be seen that all

the R = 0.9 data points reside along the low R-ratio ASME XI line for reactor water environments. An extrapolation from the R = 0.9 PWR water data to the R = 0.2 data again shows excellent agreement.

The effect of environment on fatigue crack propagation is shown in Figure 5.19. From this Figure, as well as Table 5.1 it is evident that the crack growth rate after 500 blocks for Transient C in PWR water has been enhanced by a factor of 3.3 as opposed to crack growth in argon. This enhancement decreases with increasing ΔK to 2.58 times at ΔK = 11.17 MPa$\sqrt{m}$ when compared to Bulloch and Buchanan's argon data.

0.3 Hz PWR Water Tests

Crack extension after 500 blocks at a frequency of 0.3 Hz was measured at 2.2 mm which yielded an average crack growth rate of 3.19×10^{-6} mm/cycle. Here the test was again allowed to continue to provide crack growth data over a range of ΔK. This data is illustrated in Figure 5.20. It is also clear that the effect of reducing the frequency shifts the data points closer to the high R-ratio upperbound for reactor water environments (i.e. increases crack growth rate for the same ΔK level). The Transient C data resides between the high and low R-ratio ASME XI lines for low stress intensity levels (i.e. < 10 MPa$\sqrt{m}$) while at higher stress intensity the data lies on the low R-ratio line.

The effect of environment and frequency on the Transient C test dramatically increase the fatigue crack growth rate by the order of 16 times greater than the argon test, Figure 5.21. This increase only occurred at the low ΔK range (i.e ΔK < 5.6 MPa$\sqrt{m}$) while at the higher ΔK range the increase was considerably reduced to about 4 times before increasing again to final failure.

5.1.2 Variable Amplitude Loading

5.1.2.1 3 Hz Argon Tests

All crack extension data and related ΔK levels for the various loading sequences are listed in Table 5.1. In order to determine the individual effect of the various discrete R-ratio cycles of the Spectrum loading sequence on the overall spectrum crack extension, the spectrum was divided into the various loading sequences containing fewer R-ratios (i.e. Trapezoidals and Peaks). After 500 blocks the crack extension for the individual Trapezoidal, Peak and Spectrum loading sequences were 0.33, 0.42 and 0.67 mm respectively which yielded average crack growth rates of 4.4×10^{-7}, 5.49×10^{-7} and 8.75×10^{-7} mm/cycle.

This crack growth data was then plotted (Figure 5.17) against the stress intensity levels calculated for the 0.9 R-ratio loading sequence. While it can be seen that the Trapezoidals, Peaks and Spectrum loading data points show good agreement with Bulloch and Buchanan's [64] reported 0.9 R- ratio data, there is an approximate four fold increase in crack growth rate for Trapezoidals, Peaks and Spectrum loading sequence when compared to the single Ripples (R = 0.9) data point at a ΔK level of 5.8 Mpa/m.

The crack growth rate data points for Trapezoidals, Peaks and Spectrum loading sequences reside above the ASME XI line for an air environment, indeed the Spectrum data point lies close to the low R-ratio ASME XI line for reactor environments.

5.1.2.2 3 Hz PWR Water Tests

The crack extensions after 500 blocks for the Trapezoidal, Peaks and Spectrum sequences were 1.15, 1.41 and 2.56 mm, corresponding to average crack growth rates of 1.53×10^{-6}, 1.84×10^{-6} and 3.69×10^{-6} mm/cycle respectively. This growth rate data was again plotted against the stress intensity levels calculated for the R = 0.9 loading sequence. From Figure 5.18 it can be seen that once again the variable amplitude data compares favourably

with the R = 0.9 PWR water data generated from the present study. The increase in crack growth rate for corresponding stress intensity levels, however, exhibited rather small changes i.e. 1.3, 1.3 and 1.7 times respectively. These data points also lie above the low R-ratio ASME XI line for reactor environments.

The effects of PWR water environment on the fatigue crack growth rate for the Trapezoidal, Peaks and Spectrum loading sequences is illustrated in Figure 5.19, where it is evident that the crack growth rate behaviour was enhanced by a factor of 3.5, 3.4 and 4.2 times respectively.

5.1.2.3 0.3 Hz PWR Water Tests

After 500 blocks of Spectrum loading sequence the crack had extended 3.23 mm which gave an average crack growth rate of 5.65 x 10^{-6} mm/cycle. This data is illustrated in Figure 5.20 together with the relevant R = 0.9 crack growth data generated from the present study and it is evident that the Spectrum crack growth data lie directly on the curve for the R = 0.9 data. Also these data points lie between the high R and low R-ratio ASME XI line for reactor environments.

The effect of decreasing the frequency for the spectrum loading sequence was to increase the crack growth rate by a small factor of 1.5 times when compared with 3 Hz PWR water test see Figure 5.21. The effect of environment and frequency, however, increased the crack growth rate by a factor of 6.5 times when compared to 3 Hz Argon test.

Figure 5.22 compares environmental and frequency effects resulting from variable amplitude loading tests. The effect of environment on the average crack growth data for the various Transient tests and spectrum loading test is clearly displayed in this Figure; also a significant frequency effect on both the spectrum loading and Ripples tests in PWR water is evident.

5.2 Fractography

The fracture surfaces of all fatigue crack propagation specimens were sectioned, surface cleaned and studied in the Scanning Electron Microscope at various magnifications. These will be presented in terms of the effect of environment on the fractographic features.

5.2.1 Constant Amplitude Loading

5.2.1.1 10 Hz Tests

The fractographic features of the sine and positive sawtooth specimens were very similar and thus they will be discussed together.

The argon fatigue tested specimens showed the dominant fracture mode to be ductile striated fracture. There was no evidence of the crack encountering any inclusion sites although the steel was known to contain many inclusions [1]. Clear evidence of individual striations can be seen (Figures 5.23 and 5.24) and the average measured striation spacing over the various ΔK levels tested was 1×10^{-4} mm which compares reasonably well with recorded macroscopic crack growth rates. In the case of the specimens fatigued in air the crack growth mechanism was again that of ductile striations (Figure 5.25). However in this case there is evidence of a few MnS inclusions (Figure 5.26). In the case of the specimens tested in PWR water there is evidence of the crack front encountering far more MnS inclusion clusters (Figure 5.28 and 5.29) many of which were observed to be partially dissolved (Figure 5.29). The fracture mode exhibited in this environment was primarily transgranular ductile striations (Figure 5.27)

5.2.1.2. 1 Hz Positive Sawtooth Tests

Figure 5.30 shows the general fracture surface at the start of the specimen tested in argon, and ductile striated growth is not

very evident however, at higher ΔK levels ductile striated growth became more evident (Figure 5.31). The fracture surface reveals little evidence of the crack encountering MnS inclusion clusters during growth. For the specimen fatigued in air there was a small amount of individual inclusion clusters evident on the fracture surface. These inclusions were clearly evident and still present in their sites (Figure 5.32) and it can be seen that the dominant fracture mode is once again ductile striated growth. At higher magnifications there is some evidence indicating two kinds of individual striations viz., coarse and fine (Figure 5.33). Measurement of the coarse striations give average striation spacing which range between 1×10^{-4} mm to 4×10^{-4} mm which exhibits good commonality with the observed macrocrack growth rates which ranged between 1×10^{-4} and 5×10^{-4} mm/cycle. Evidence that the growing crack front had encountered numerous non-metallic inclusion clusters is shown in Figure 5.34 while Figure 5.35 shows the detailed nature of crack extension through an individual cluster. At high magnifications (Figure 5.36 and 5.37) partially dissolved MnS inclusions can still be seen in their sites while the general fracture mode was ductile striated growth with an average striation spacing of 1×10^{-4} mm, at an observed macroscopic growth rate which ranged between 2×10^{-4} and 6×10^{-4} mm/cycle.

5.2.1.3 1 Hz Sine Wave Tests

Figure 5.38 shows a rough fracture surface with deep fissure formation perpendicular to the crack growth direction, such features are characteristic of ductile striated fatigue fracture. Little evidence of individual inclusion clusters were evident in this specimen. Individual striations were observed (Figure 5.39) and their average spacing was 1×10^{-4} mm. Evidence of some isolated inclusion clusters were observed (Figure 5.40 and 5.41) in those specimens which were fatigued in air while the general fracture mode was ductile striated growth. The specimen tested in PWR water again showed evidence of numerous inclusions clusters within which partially dissolved MnS inclusions were observed (Figure 5.43 and 5.44). As shown in Figure 5.42, ductile striated growth was again the dominant fracture mode.

5.2.1.4 0.1 Hz Sine Wave Test

The 0.1 Hz PWR water test exhibited extensive isolated regions of intergranular failure dispersed within a transgranular ductile striated fatigue fracture surface at initial ΔK levels i.e. 24 MPa√m. The percentage area of this static subcritical fracture mode was assessed 36%, (Figure 5.45) while the size of the intergranular facets varied between 20 to 60 μm. A detailed view of the intergranular failure regions, (Figure 5.46) show

(i) that the separate regions of intergranular failure are connected by a ductile fatigue crack growth fracture mode,

(ii) evidence of a corrosion product that covered the otherwise smooth grain boundary regions of failure.

With increasing ΔK level the extent of intergranular failure is reduced, until at ΔK=30 MPa√m the fatigue fracture mode was almost totally ductile striated growth, see Figures 5.47 - 5.50. However, small areas of fan-shaped growth (100μm by 80μm in size), associated with non-metallic inclusion clusters, were evident.

5.2.1.5 High R Ratio Tests

3 Hz Argon Tests

A general view of the ribbon of fatigue crack extension, approximately 150 μm in size, for the Ripples test is shown in Figure 5.51. Note the significant difference in fatigue fracture appearance between the air pr cracking region and the argon fatigued region. A solitary MnS inclusion with the associated void formation is also evident while a detailed view (Figure 5.52) shows that the fatigue fracture process exhibits a certain degree of directionality.

3 Hz PWR Water Tests

The specimen subjected to the Ripples loading programme was allowed to continue past the 500 blocks so that more data points for crack growth behaviour could be obtained. This led to different fractographical features being observed in the different crack growth regimes.

At the near threshold ΔK levels (Figure 5.53) the fracture surface shows ductile crack extension which contained highly directional tear ridges. A small isolated region of intergranular decohesion of approximately 12 μm in size can also be observed.

At intermediate ΔK levels the fracture surface is predominantly transgranular ductile striated growth (Figure 5.54), once again small isolated incidences of intergranular failure can be seen. Facets were between 10-15 μm in size.

At relatively higher ΔK levels, i.e. as the crack approached final failure, the fracture surface showed extensive ductile fatigue crack growth extension in the form of microvoid coalescence (Figure 5.55). There is a large variation in dimple size with the largest dimples being 30 μm in size. These microvoids are associated with non-metallic MnS inclusions which have been torn out of the microvoids or have remained on the companion fracture surface.

0.3 Hz PWR Water Tests

A general low magnification view (Figure 5.56) of the fracture surface immediately at the start of testing, i.e. ΔK level of 5.6 MPa/m, shows that while the main fracture mode was transgranular ductile striated growth, extensive intergranular facets are evident which accounted for some 18% of the fatigue surface area. Subsequent fractographs at increasing ΔK levels (Figures 5.57 - 5.59) show a dominant fracture mode of ductile striated growth and decreasing area fractions of intergranular failure. A detailed view of intergranular facets (Figure 5.60) that occurred near the precrack region shows facets of 10 - 30 μm in size with

evidence of a rough corrosion product on the facetted regions. Near the final failure region, (Figures 5.61 - 5.62) i.e. $\Delta K \sim 11$ MPa$\sqrt{m}$, the fracture mode is a combination of ductile striated crack growth with regions of microvoid coalescence which had an average dimple size of approximately 25 μm.

5.2.2 Variable Amplitude Loading

5.2.2.1 3 Hz Argon Tests

For the specimen subjected to the Peaks loading programme (see Figure 5.63 and 5.64) no evidence of plasticity effects due to overloading or underloading viz., beach marks etc. were observed. There was, however, much evidence of ductile striated fracture mode. Similar details for the specimen subjected to the Trapeziodal loading programme (Figure 5.65 and 5.66) were observed. The specimen subjected to the spectrum loading programme showed much evidence of ductile striated growth (Figure 5.67) while at higher magnification (Figure 5.68 and 5.69) individual striations were clearly seen and exhibited an average striation spacing of 8×10^{-4} mm which was somewhat greater than the average crack growth recorded for this particular specimen. Figure 5.70 shows a MnS inclusion cluster surrounded by striated growth, many of the inclusions are clearly evident in individual sites.

5.2.2.2 3 Hz PWR Water Tests

Figure 5.71 gives a general view of the fracture surface of the specimen subjected to the Peaks programme where the predominant fracture mode is once again transgranular ductile striated fracture. A detailed view, Figure 5.72, shows the nature of striated crack extension and an isolated region of intergranular decohesion is clearly evident. These intergranular facets varied between 20-30 μm in size. Similarly for the Trapezoidal specimen the predominant fracture mode was transgranular ductile striated fatigue crack growth. However, in this case there was evidence of isolated fan-shaped regions (Figure 5.73) within which the

ductile nature was markedly reduced and isolated fan-shaped regions were recorded, see Figure 5.73.

For the Spectrum specimen the dominant fracture mode (Figure 5.74) was also transgranular ductile striated growth. Figure 5.75 shows that the metal fatigue region just ahead of the precracked region encountered a number of MnS inclusion clusters. A more detailed view (Figure 5.76) shows that some of the MnS inclusions have been dissolved out and also the reduced ductility in the region just ahead of the cluster. A further interesting feature observed was the "elephant trunk" (Figure 5.77). This was caused by some hard debris being trapped in the opposite fracture surface and with each cycle, impacting the other surface forming this rippled effect.

5.2.2.3 0.3 Hz PWR Water Tests

For the Spectrum loaded specimen while the fracture mode was mainly transgranular ductile striated growth there were numerous flat featureless regions (Figure 5.78) which were dispersed over the entire fatigue crack growth region. A more detailed view (Figure 5.79) of the flat amorphous fan shaped regions show river type lines emanating from a point source, P. A high magnification view (Figure 5.80) indicates that the possible initiation point P could have been a large carbide or more likely an inclusion.

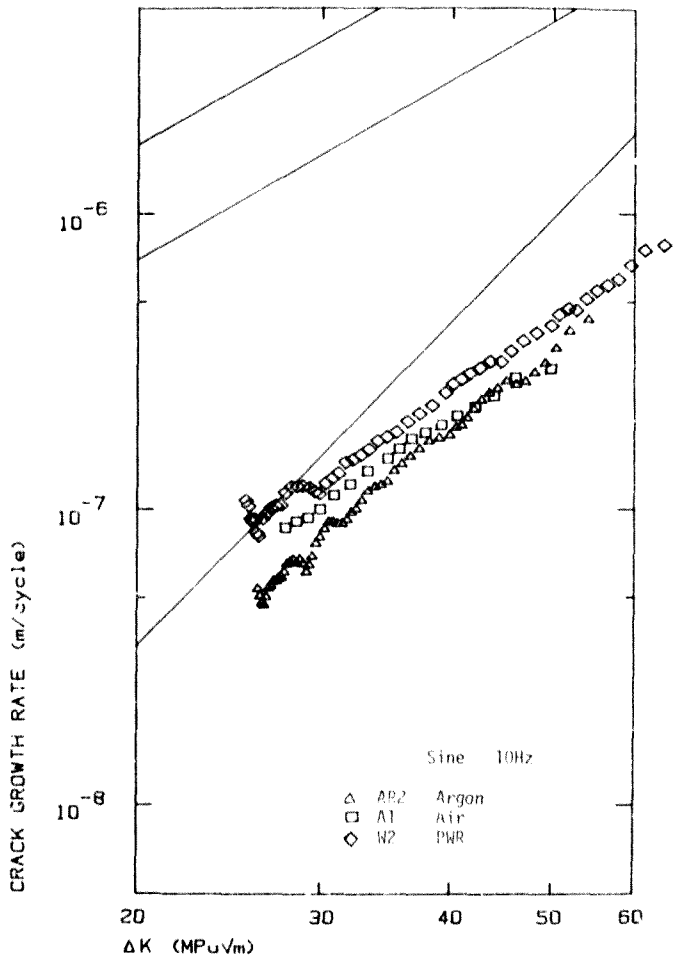

Figure 5.1: Effects of environment using sine wave loading at 10 Hz. Air and argon line below ASME dry line and agrees well with 1 Hz data. PWR data lines slightly above this.

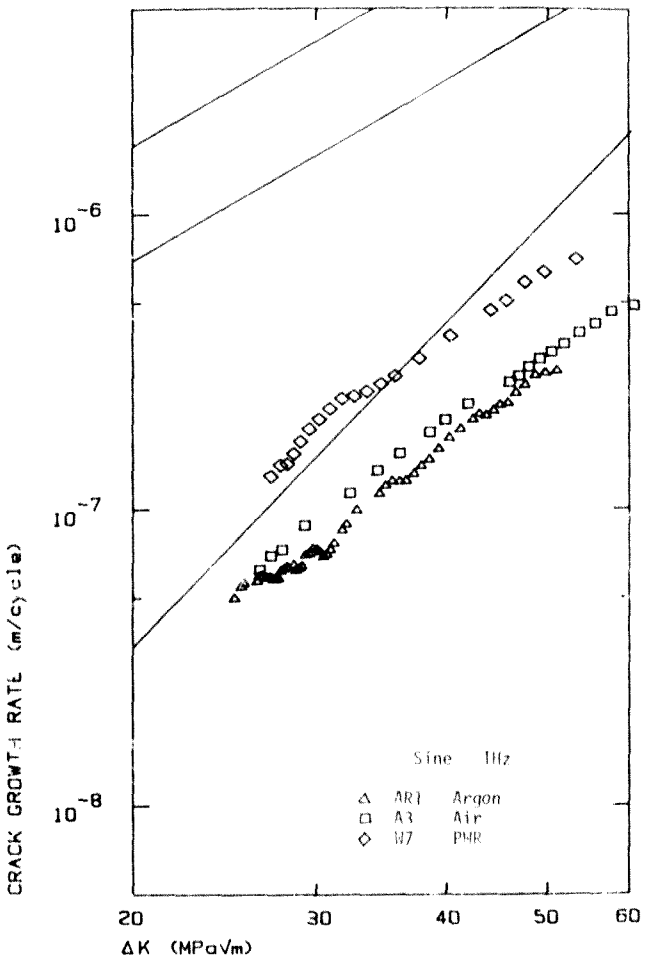

Figure 5.2: Effect of environment using simusoidal loading at 1 Hz. Air and argon lie below the ASME dry line. The LWR data resides above them and on the dry line.

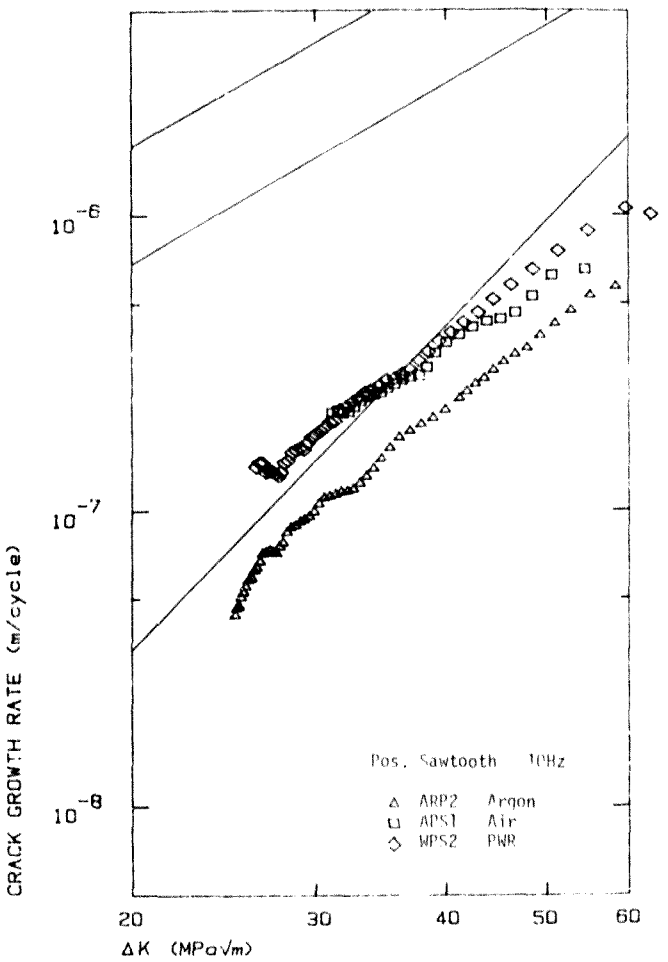

Figure 5.3: Effect of environment using positive sawtooth at 10 Hz. Argon data lie below the ASME dry line while the air and PWR environments give growth rates that are above the ASME dry line, but drops below this line for high ΔK values.

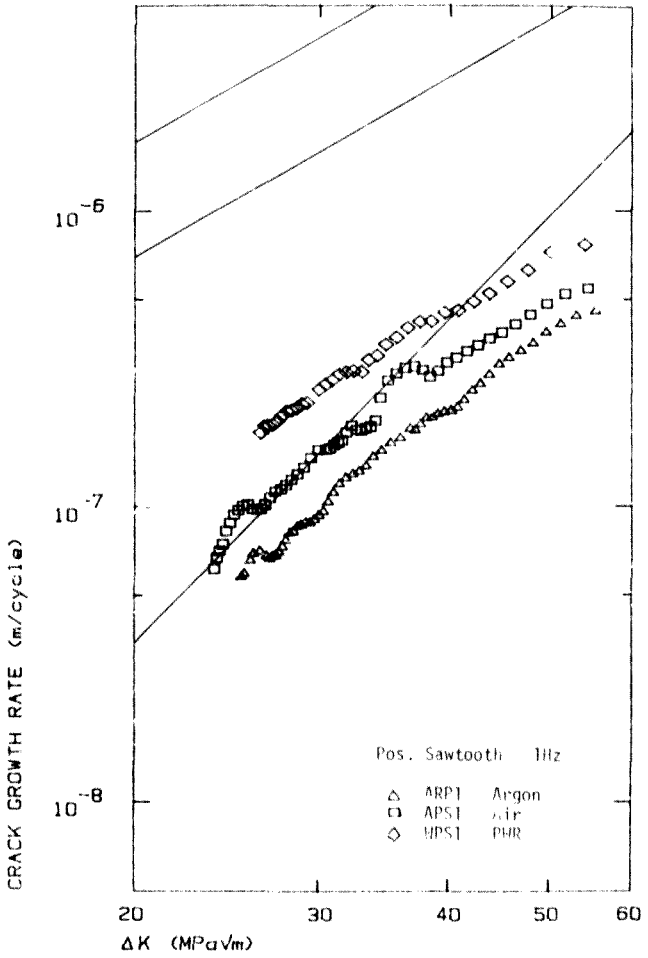

Figure 5.4: Effect of environment using positive sawtooth at 1 Hz. At $\Delta K < 40$ MPa$\sqrt{m}$ air growth rate is 1.5 times faster than argon growth rate while PWR growth rate is 7 times faster than air growth rate.

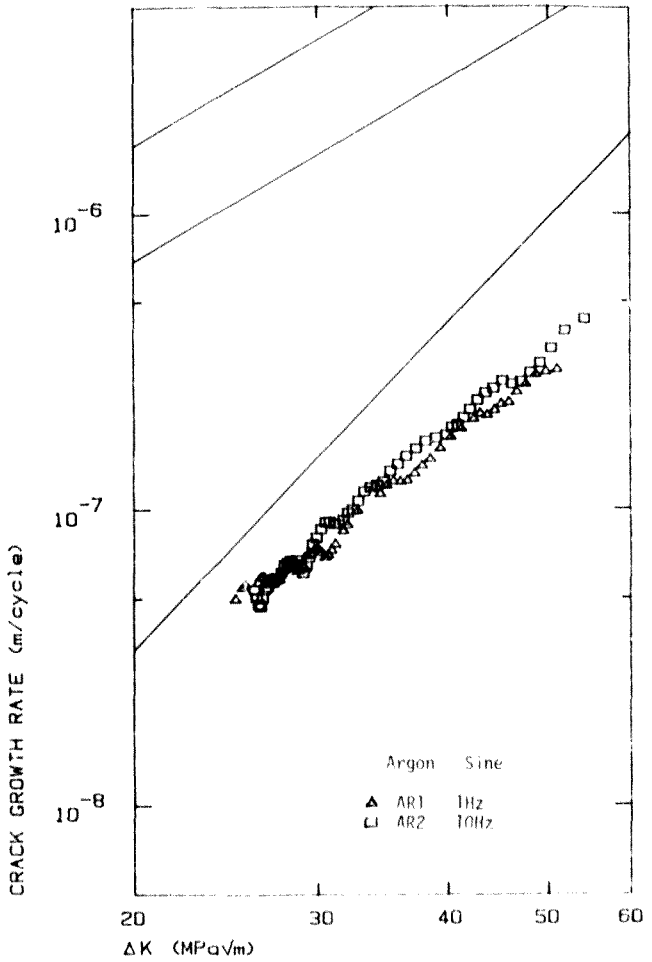

Figure 5.5: Effect of frequency in argon using simusoidal loading. Note that in argon there is very little difference resulting from lowering of the frequency.

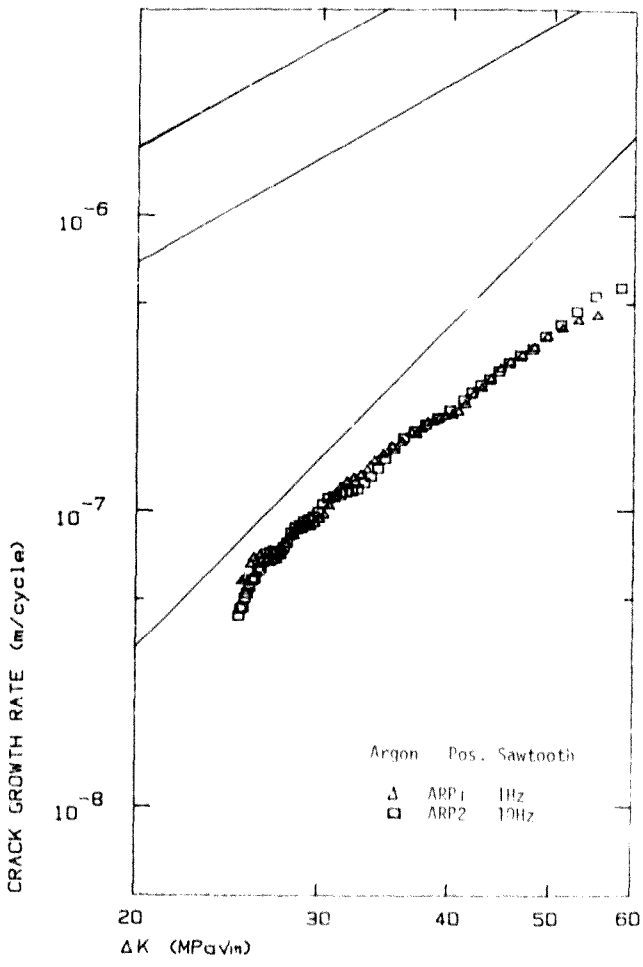

Figure 5.6: Effect of frequency in argon using positive sawtooth loading. There is no difference in the fatigue crack growth rate.

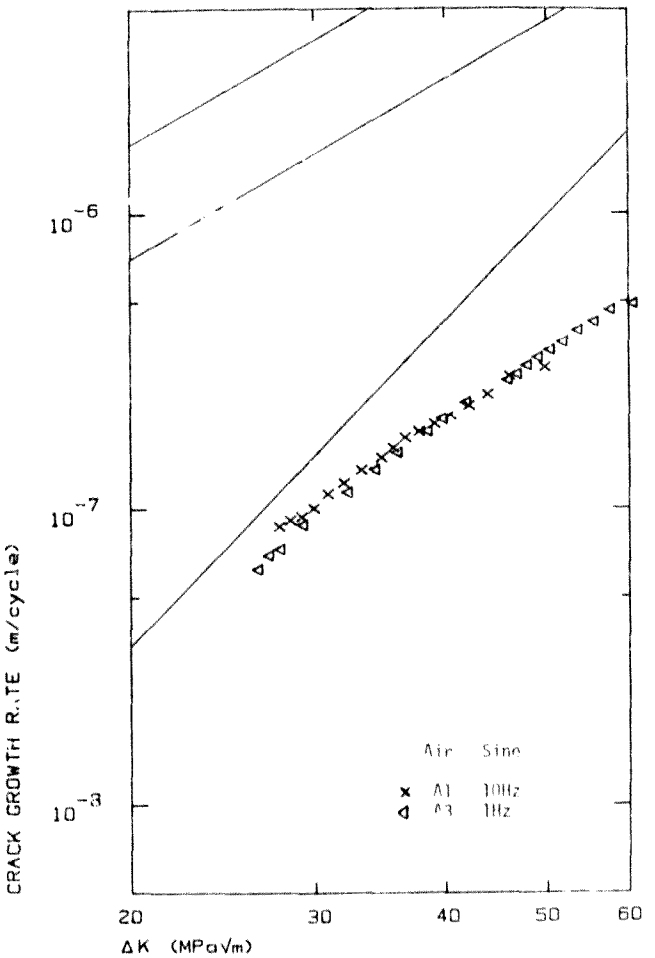

Figure 5.7: Effect of frequency in air using positive sawtooth loading. No noticeable difference in the crack growth rate.

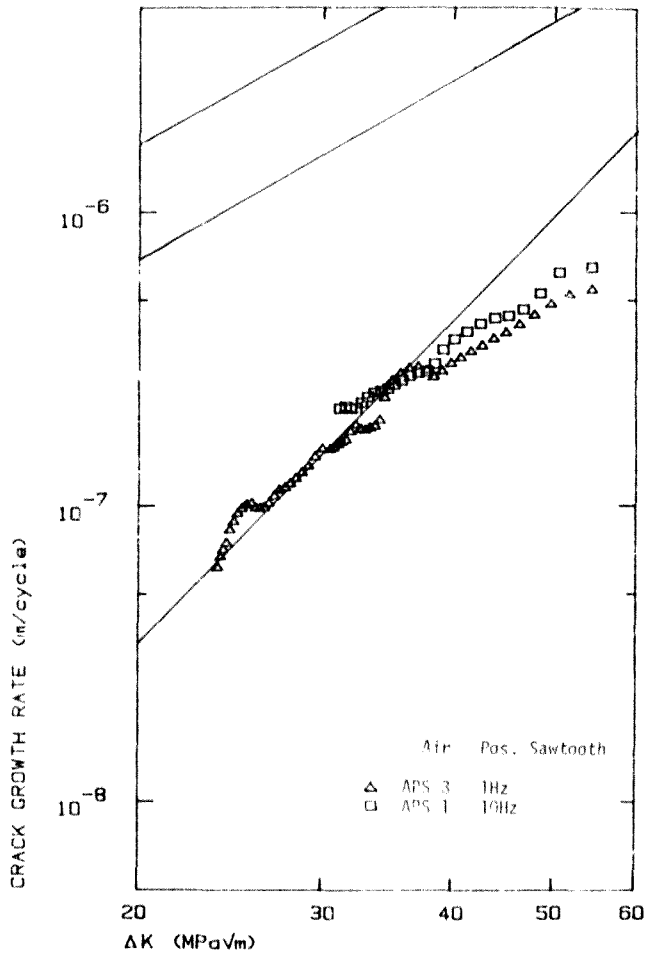

Figure 5.8: Effect of frequency in air using positive sawtooth shows no marked increase in the rate of crack propagation.

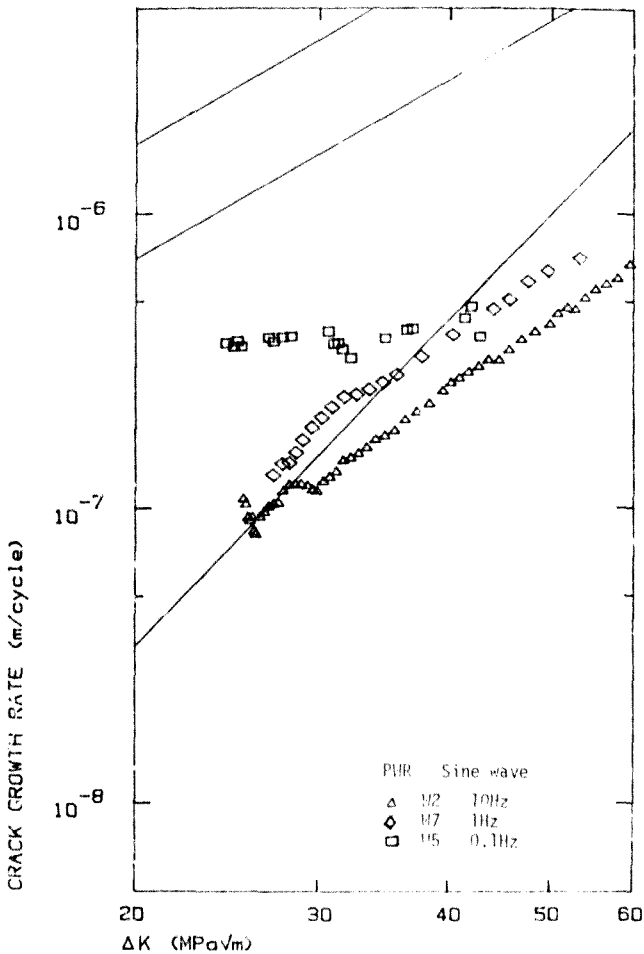

Figure 5.9: Effect of frequency in PWR water using sine wave shows definite increase in the crack growth rate as the frequency is decreased. Note the plateau formation at 0.1 Hz.

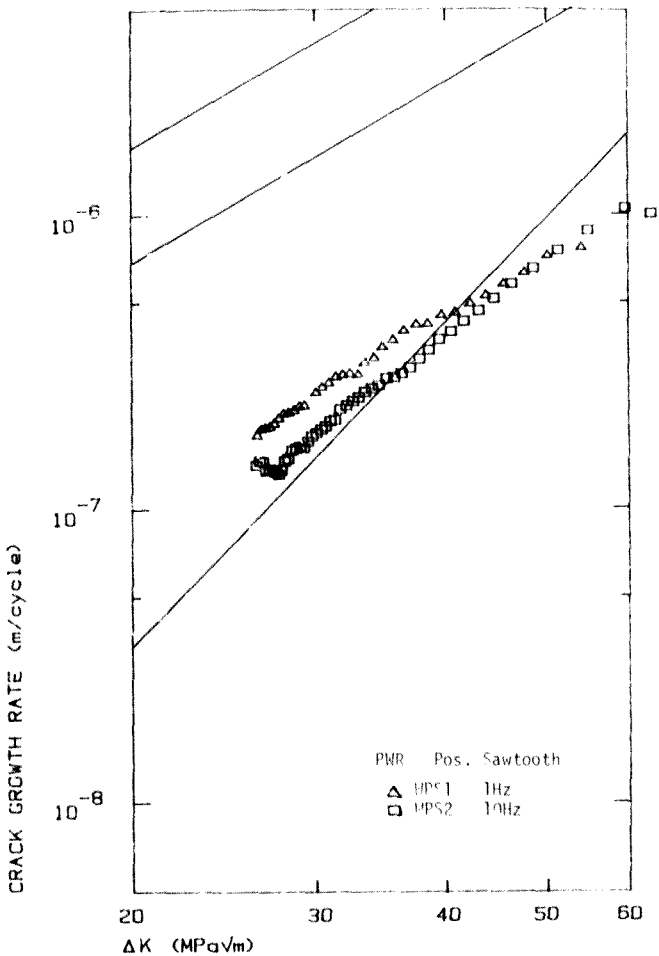

Figure 5.10: The effect of frequency in PWR water using positive sawtooth gives crack growth rates that are 1.4 times faster than those for sine wave at ΔK values below 40 MPa/m.

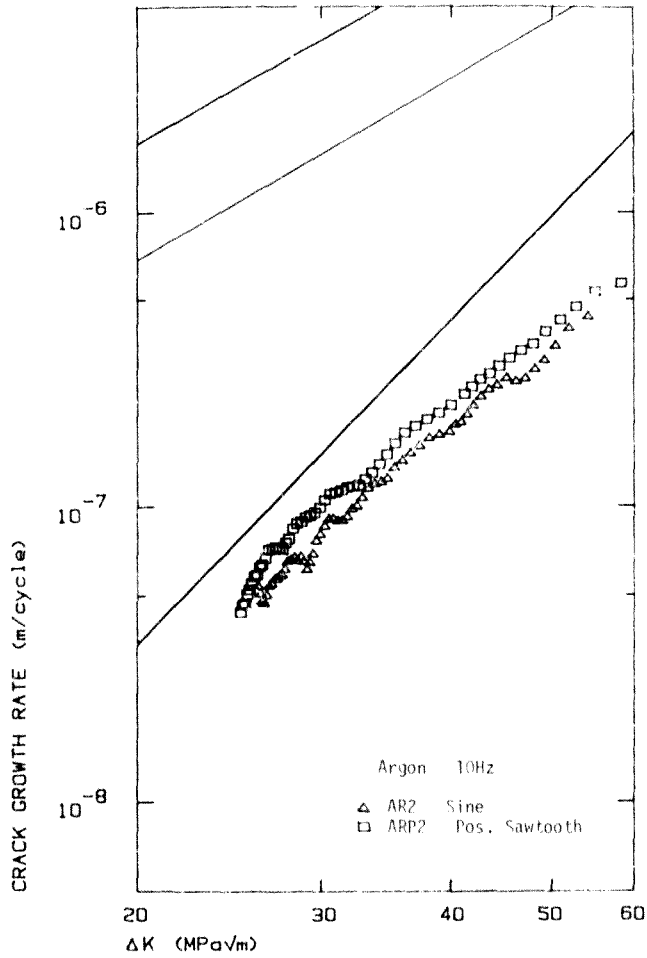

Figure 5.11: The effect of waveform in argon at 10 Hz shows little difference between the two wave shapes.

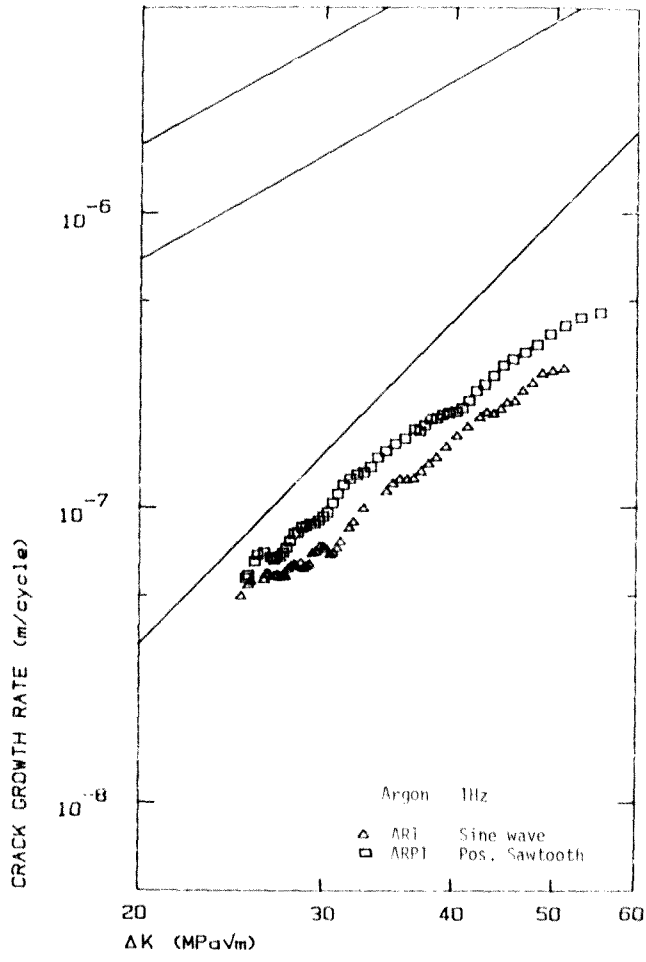

Figure 5.12: Effect of waveform in argon at 1 Hz. Positive sawtooth growth rate ~ 1.3 times that of sinusoidally varying load.

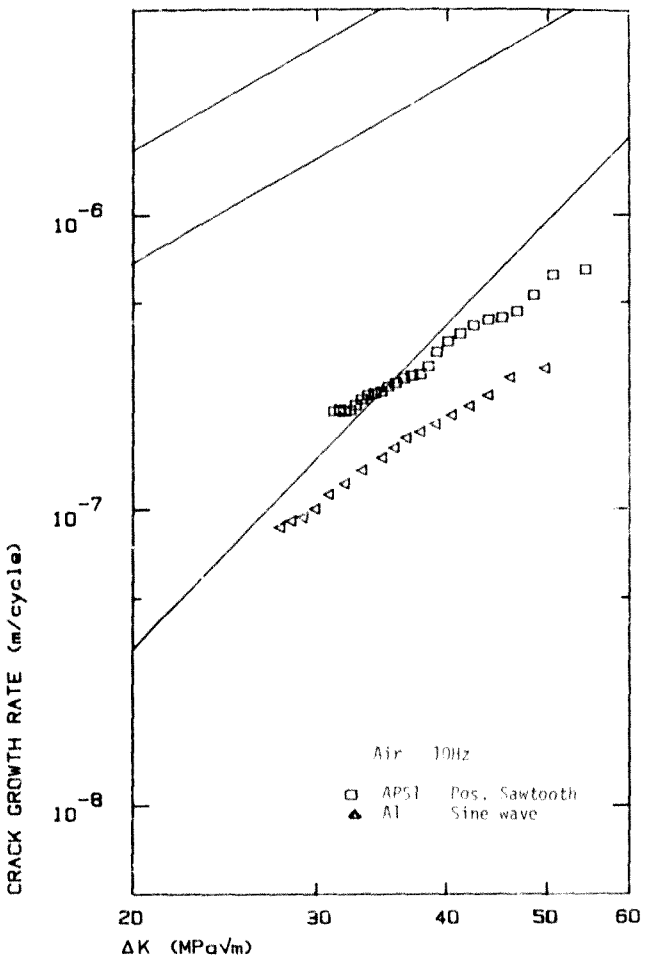

Figure 5.13: Effect of waveform in air at 10 Hz. Here the positive sawtooth growth rate is ~ 2 times faster than that of sine wave.

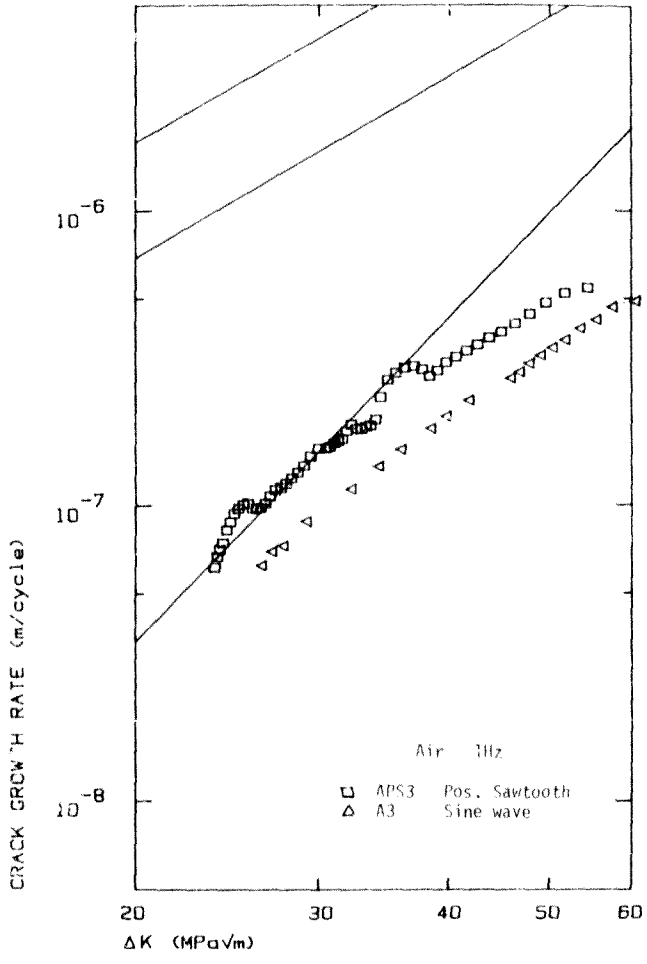

Figure 5.14: Effect of waveform in air at 1 Hz. The crack growth rate due to positive sawtooth loading was approximately 1.5 times faster than sine wave.

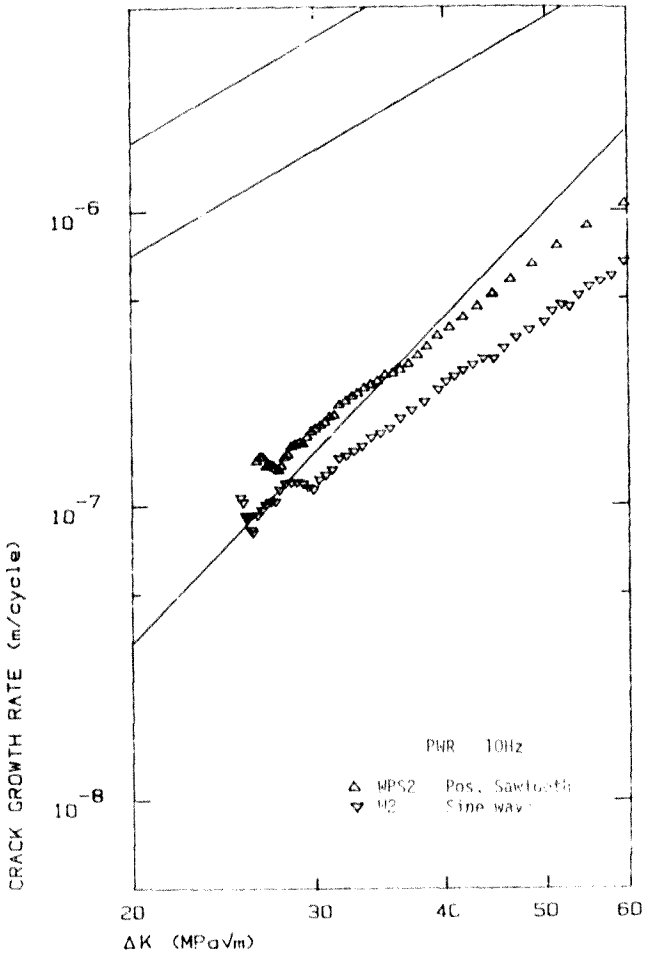

Figure 5.15: Effect of waveform on PWR water at 10 Hz leads to 1.5 times faster crack growth rate using positive sawtooth than sine wave.

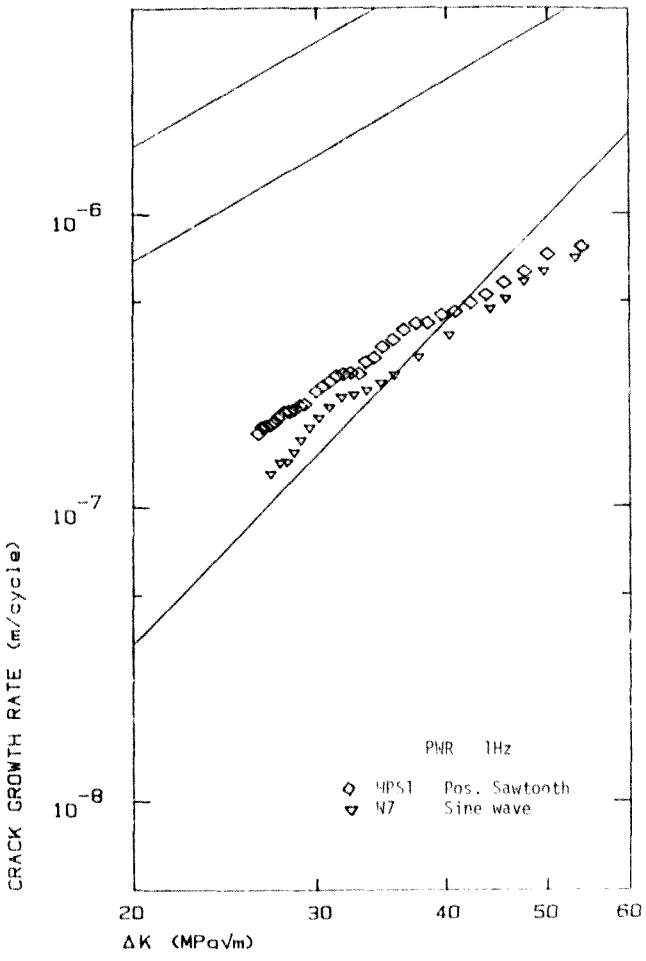

Figure 5.16: Effect of waveform at 1 Hz while not showing a larger difference in the waveforms the starting crack growth rate lies above the ASME dry line.

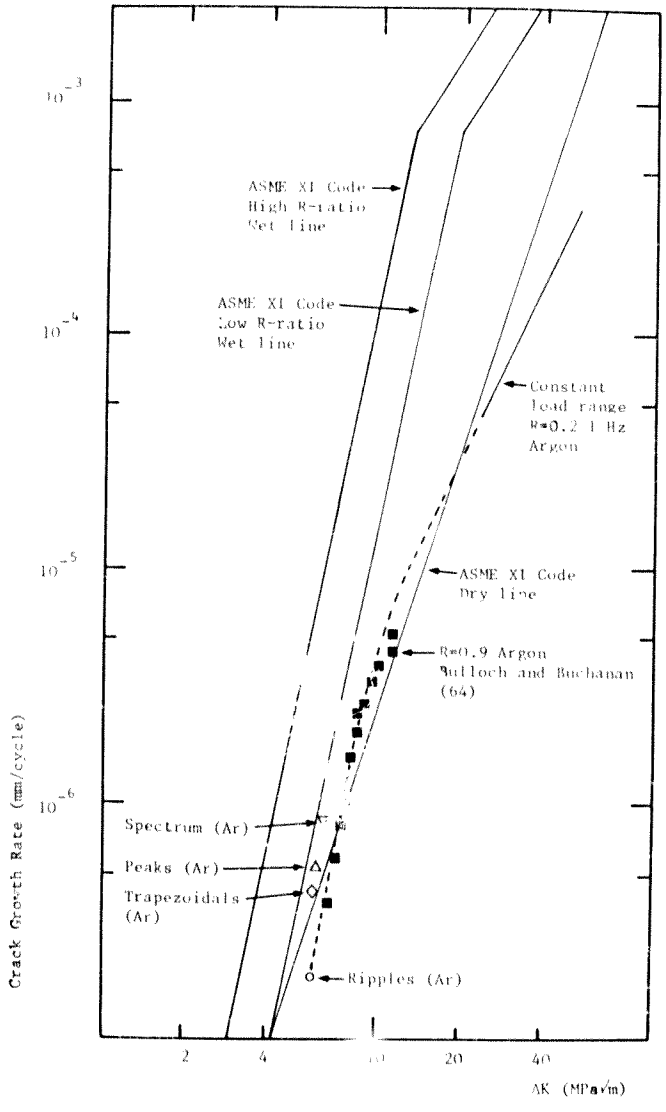

Figure 5.17: Fatigue crack growth data in argon for 3 Hz variable amplitude loading.

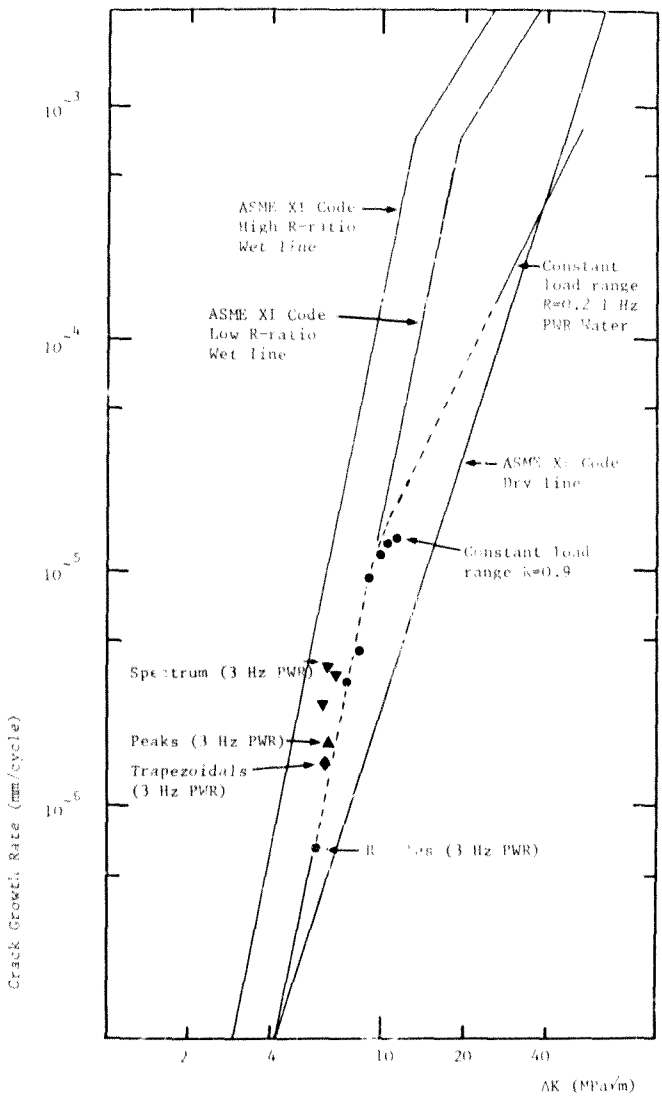

Figure 5.18: Fatigue crack growth data in PWR water environment for 3 Hz variable amplitude loading.

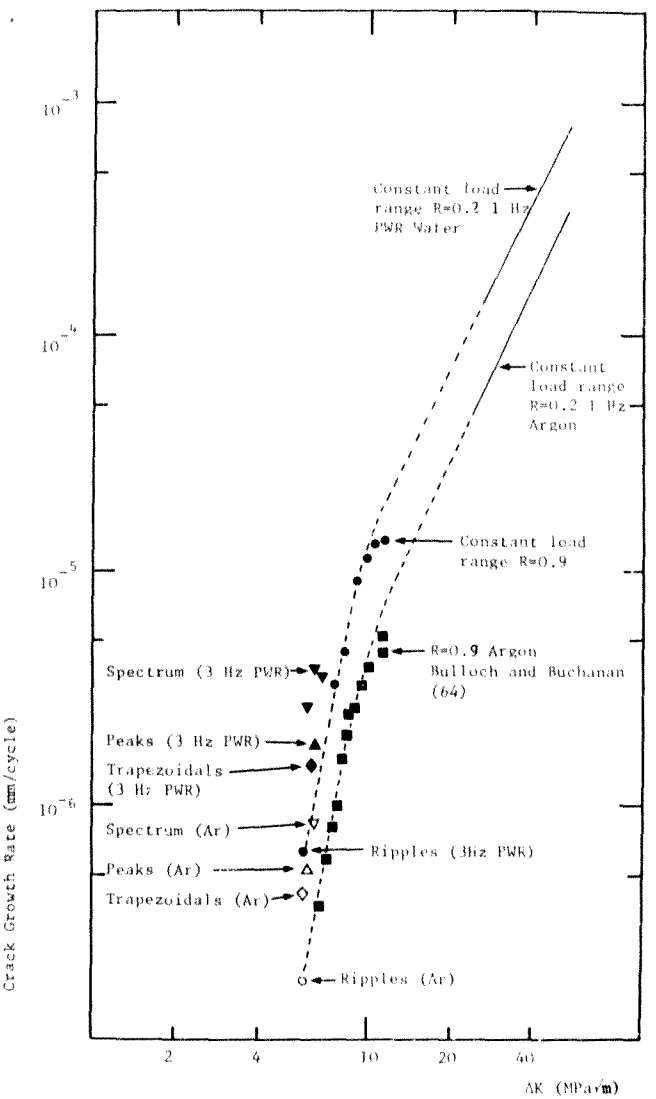

Figure 5.19: Effect of environment on fatigue crack growth behaviour for variable amplitude loading.

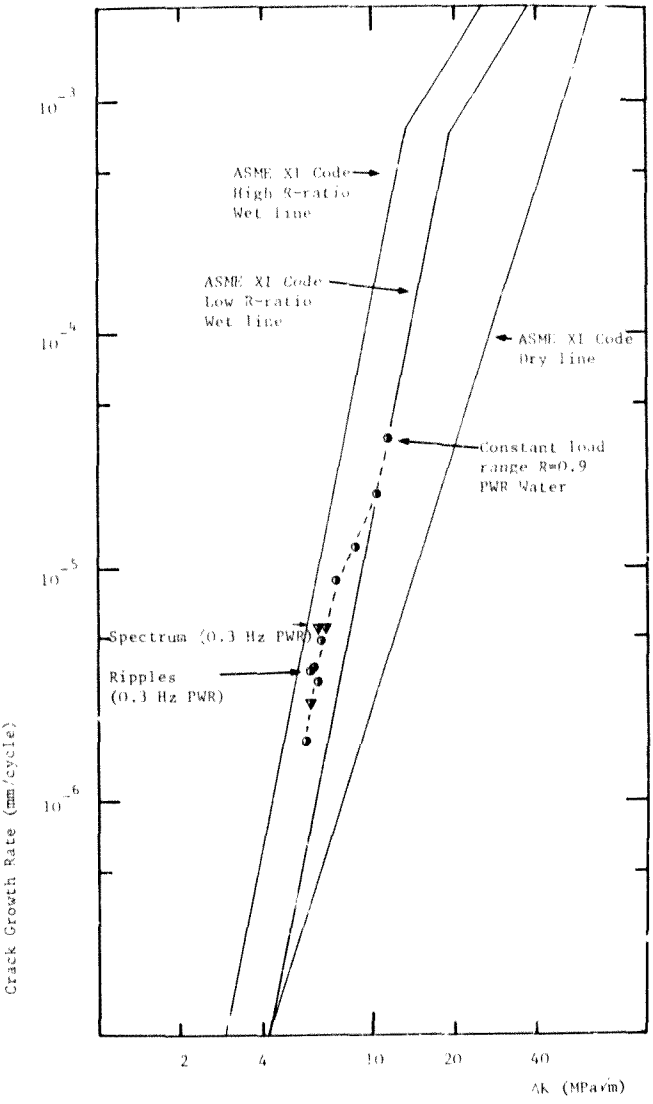

Figure 5.20: Fatige crack growth data in PWR water environment for 0.3 Hz variable amplitude loading.

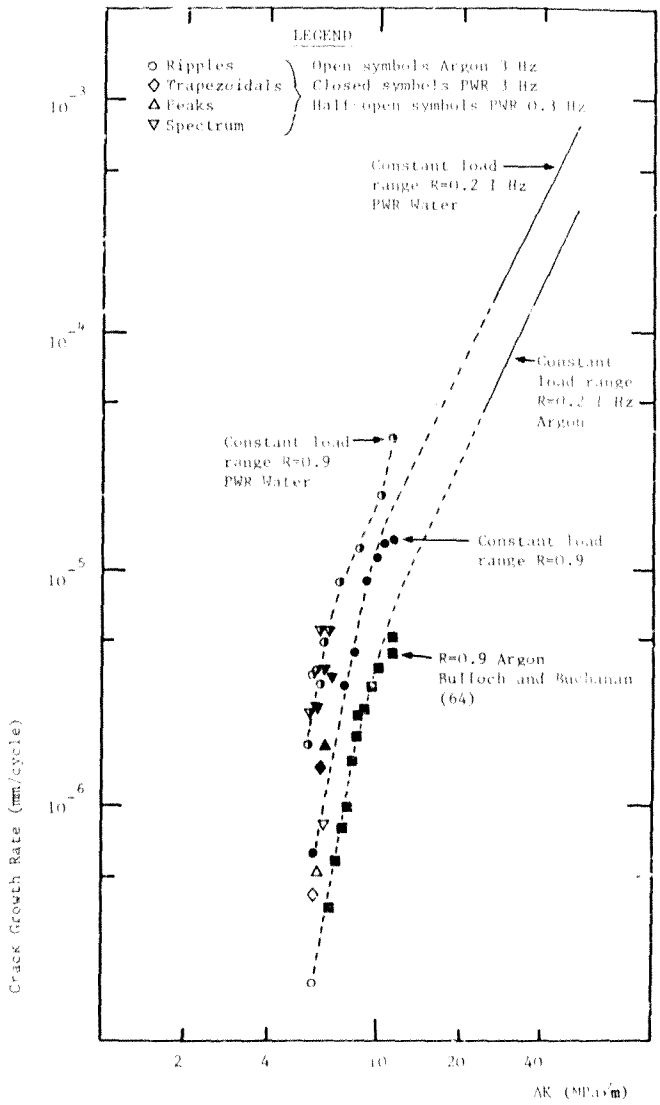

Figure 5.21: Effect of environment and frequency on fatigue crack growth behaviour for variable amplitude loading.

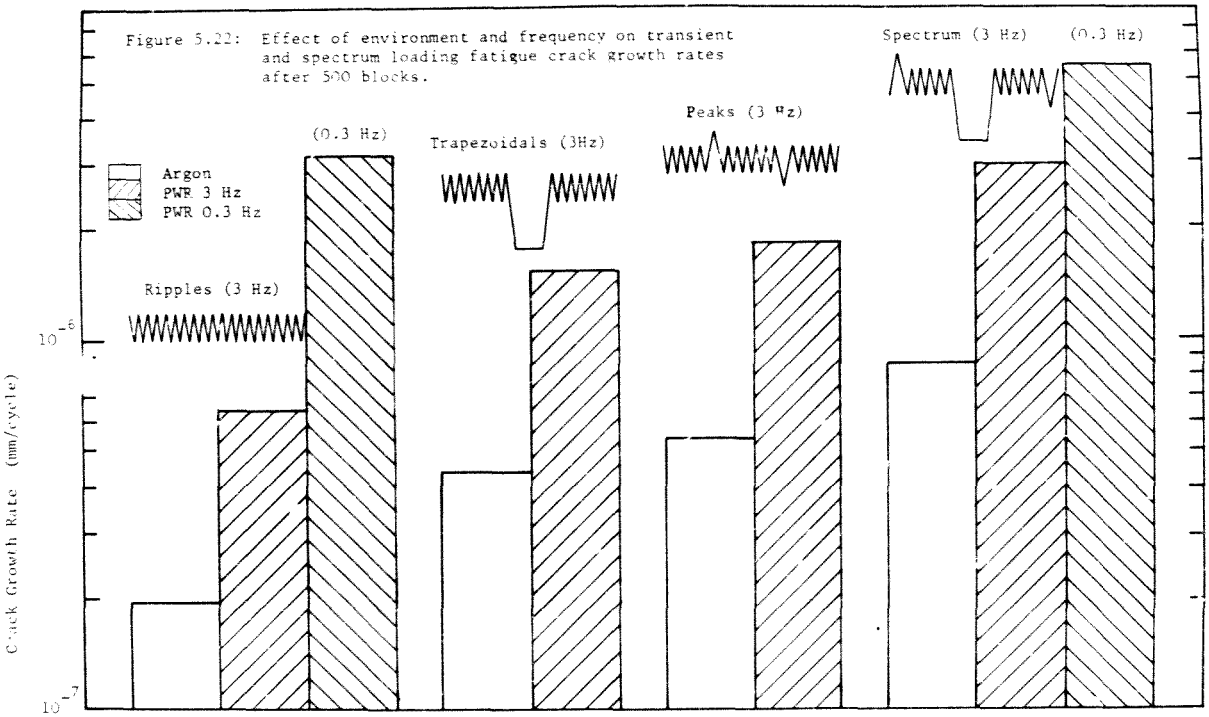

Figure 5.22: Effect of environment and frequency on transient and spectrum loading fatigue crack growth rates after 500 blocks.

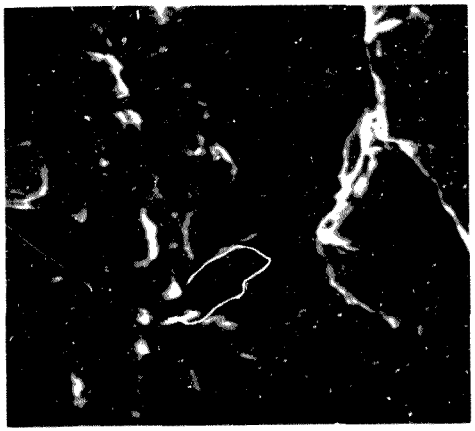

Crack growth direction.

Figure 5.23 2 μm

Ductile striated growth dominant fracture mode.
Positive Sawtooth, Argon, 10 Hz. Mag. x 5000

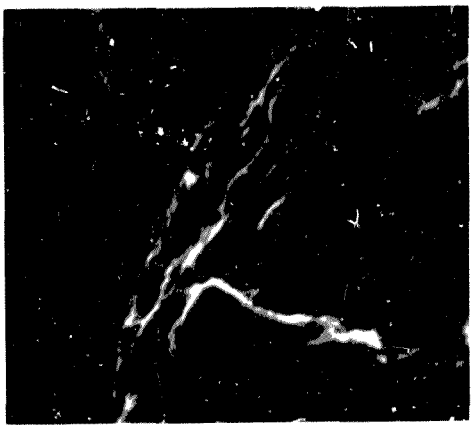

Crack growth direction.

Figure 5.24 2 μm

Striations clearly visible.
Positive Sawtooth, Argon, 10 Hz. Mag. x 5000

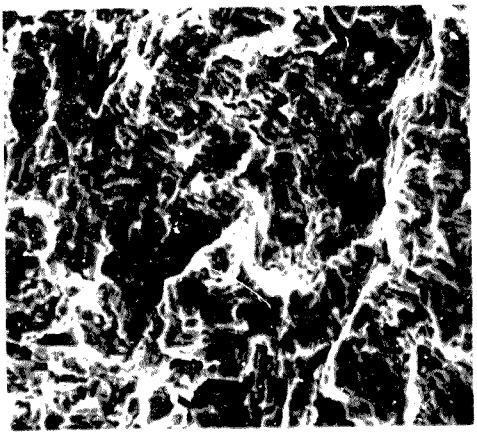

Crack growth direction.

Figure 5.25 10 μm

General area showing transgranular ductile striated growth. Note secondary cracks. Positive Sawtooth, Air, 10 Hz. Mag. x 1000

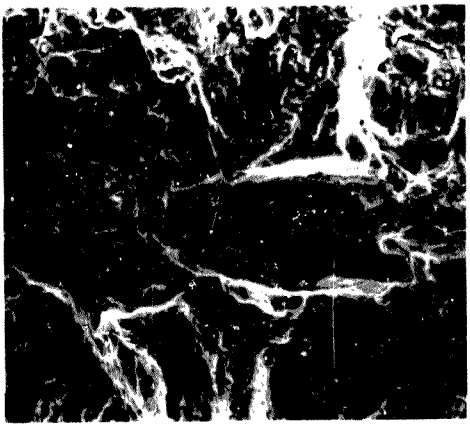

Crack growth direction.

Figure 5.26 10 μm

Inclusion site with undissolved MnS inclusion still present. Positive Sawtooth, Air, 10 Hz. Mag. x 1000

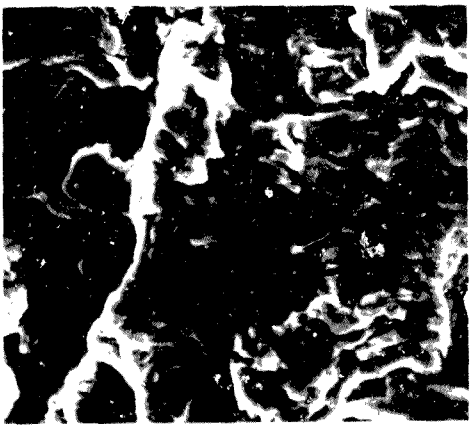

Crack growth direction.

Figure 5.27 5 μm

General fracture surface showing ductile striated growth as fracture mode. Positive Sawtooth, PWR Water, 10 Hz. Mag. x 3000

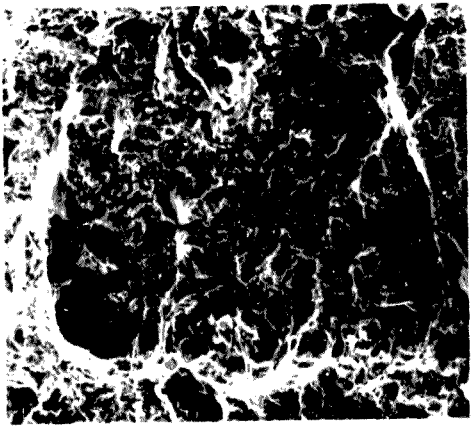

Crack growth direction.

Figure 5.28 2 μm

Dissolved MnS inclusion clusters.
Positive Sawtooth, PWR Water, 10 Hz. Mag. x 6000

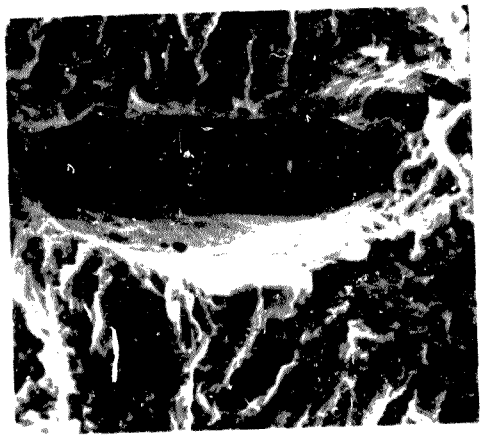

crack growth direction.

Figure 5.29 5 μm

Partially dissolved MnS inclusion cluster.
Positive Sawtooth, PWR Water, 10 Hz. Mag. x 2000

Crack growth direction.

Figure 5.30 10 μm

Fracture surface at start of test, ductile striated growth not very evident. Positive Sawtooth, Argon, 1 Hz. Mag. x 1000

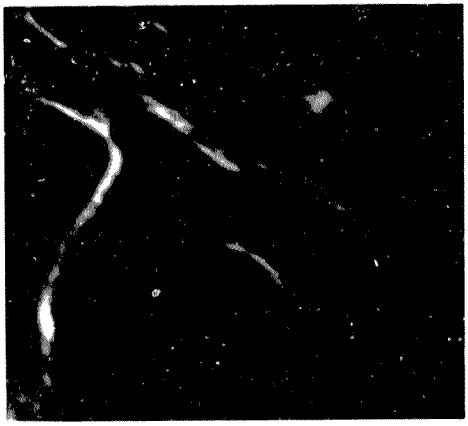

Crack growth direction.

Figure 5.31 5 μm

Ductile striations clearly visible.
Positive Sawtooth, Argon, 1 Hz. Mag. x 5000

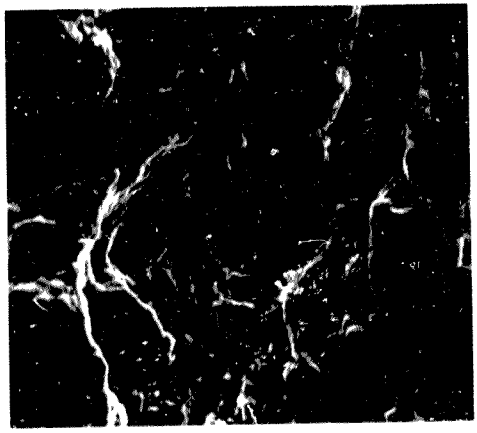

Crack growth direction.

Figure 5.32 5 μm

Undissolved MnS inclusion still intact.
Positive Sawtooth, Air, 1 Hz. Mag. x 2000

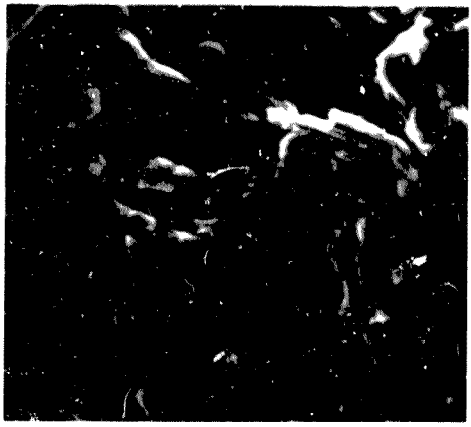

Crack growth direction.

Figure 5.33 5 μm

Ductile striated growth with secondary cracking.
Positive Sawtooth, Air, 1 Hz. Mag. x 5000

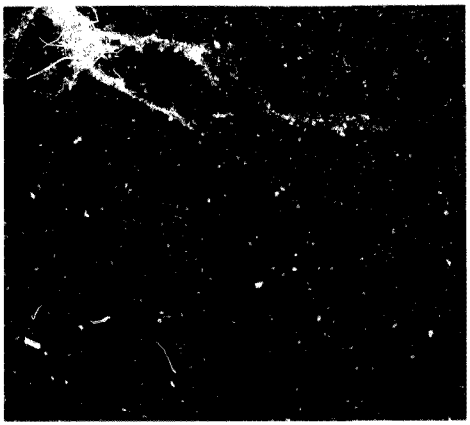

Crack growth direction.

Figure 5.34 500 μm

Fracture surface with numerous MnS inclusion clusters.
Positive Sawtooth, PWR Water, 1 Hz. Mag. x 20

Crack growth direction.

Figure 5.35 50 μm

MnS inclusion cluster encountered by the advancing crack front.
Positive Sawtooth, PWR Water, 1 Hz. Mag. x 200

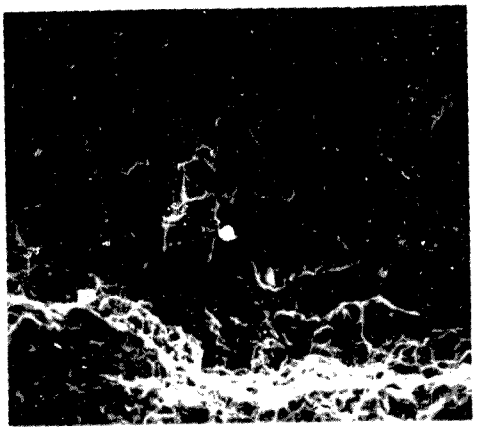

Crack growth direction.

Figure 5.36 10 μm

Inclusion cluster with some MnS inclusions intact.
Positive Sawtooth, PWR Water, 1 Hz. Mag. x 1000

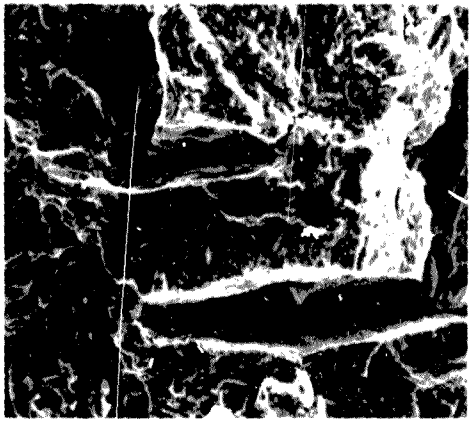

Crack growth direction.

Figure 5.37 10 μm

Partially dissolved MnS inclusion.
Positive Sawtooth, PWR Water, 1 Hz. Mag. x 1000

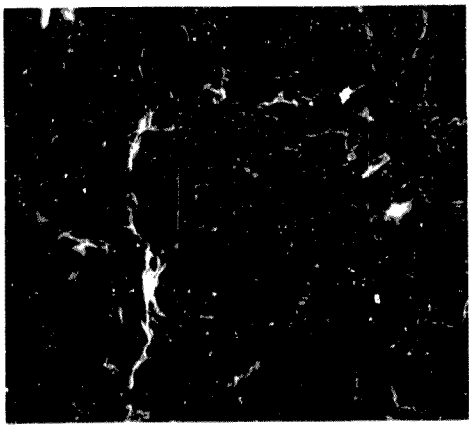

Crack growth direction.

Figure 5.38 10 μm

General surface showing ductile striated growth.
Sine, Argon, ' Hz. Mag. x 1000

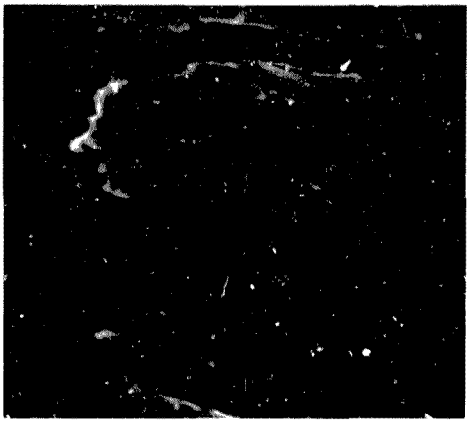

Crack growth direction.

Figure 5.39 2 μm

Ductile striations. Note also secondary cracks.
Sine, Argon, 1 Hz Mag. x 5000

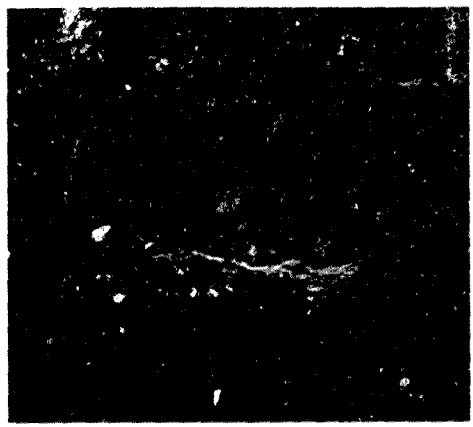

Crack growth direction.

Figure 5.40 50 μm

MnS inclusion cluster.
Sine, Air, 1 Hz. Mag. x 200

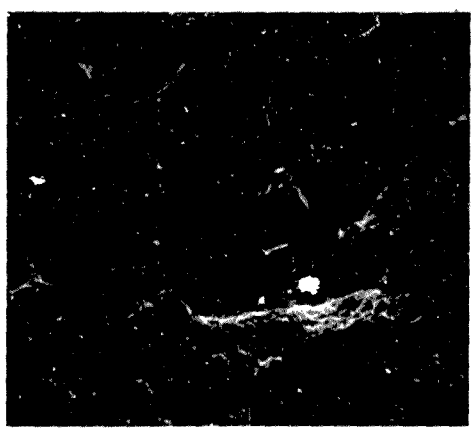

Crack growth direction.

Figure 5.41 50 μm

Further evidence of MnS inclusion clusters with some inclusions still intact. Sine, Air, 1 Hz. Mag. x 200

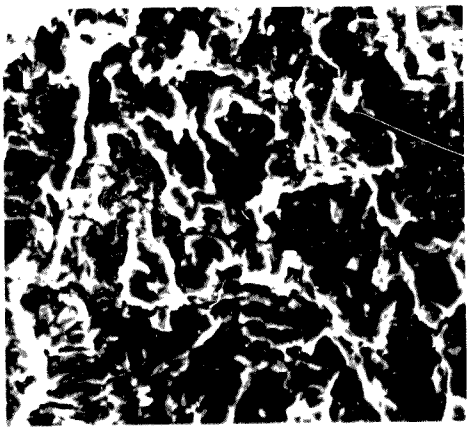

Crack growth direction.

Figure 5.42 20 μm

General fracture surface showing ductile striated growth.
Sine, PWR Water, 1 Hz. Mag. x 500

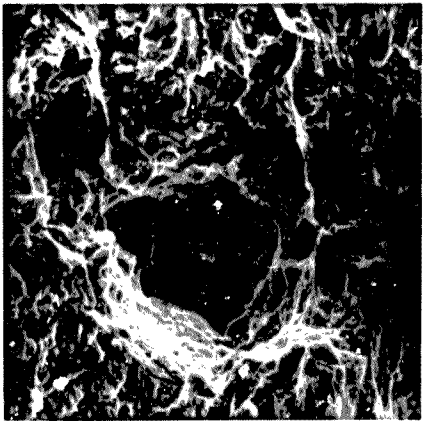

Crack growth direction

Figure 5.43 20 μm

Small globular partially dissolved MnS inclusion.
Sine, PWR Water, 1 Hz. Mag. x 500

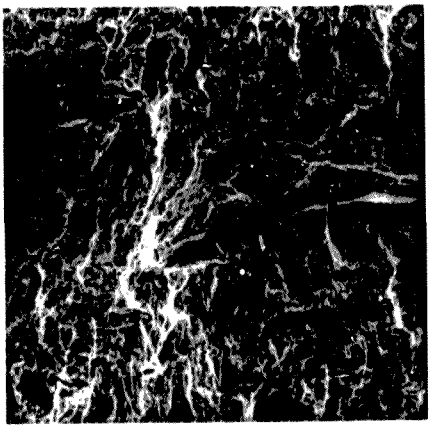

Crack growth direction.

Figure 5.44 20 μm

Partially dissolved elongated MnS inclusion.
Sine, PWR Water, 1 Hz. Mag. x 500

Crack growth direction.

Figure 5.45 58 μm

Intergranular failure interspersed between ductile striated growth. IG failure=36%. Sine, PWR Water, 0.1 Hz. Mag. x 172

Crack growth direction.

Figure 5.46 10 μm

Detailed view of intergranular failure. Note evidence of corrosion product. Sine, PWR Water, 0.1 Hz. Mag. x 1290

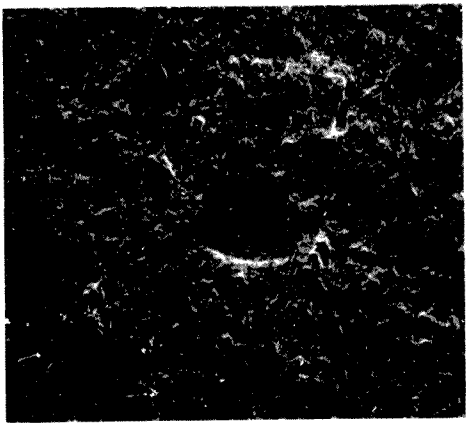

crack growth direction.

Figure 5.47 80 μm

General view of fatigue fracture surface. EAC growth fan 100 x 80 μm. Sine, PWR Water, 0.1 Hz. Mag. x 1900

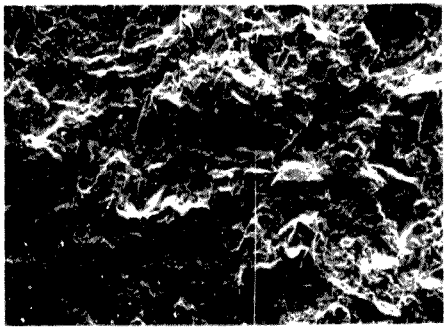

Crack growth direction

Figure 5.48

Mag. x 600

25 μm

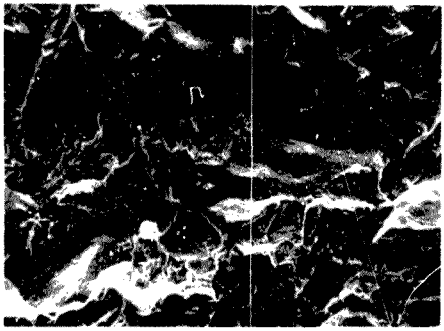

Crack growth direction.

Figure 5.49

Mag. x 1000

10 μm

Crack growth direction

Figure 5.50

Mag. x 2500

5 μm

This series of micrographs show an increasingly detailed view of a specific region of intergranular failure at initial ΔK levels of fatigue testing in a PWR environment. The facet size varies from 20 - 60 μm. Sine, PWR Water, 0.1 Hz.

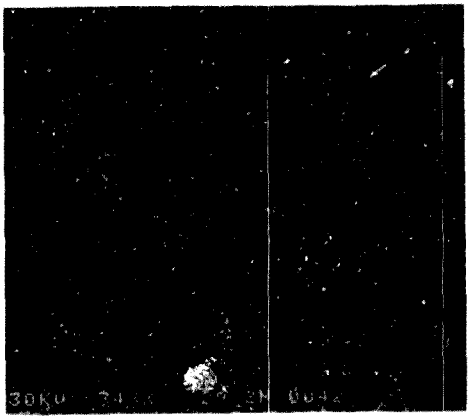

Figure 5.51

Note difference in fracture appearance between Air and Argon fatigued region. 0.9 R-ratio, Argon, 3 Hz. Mag. x 343

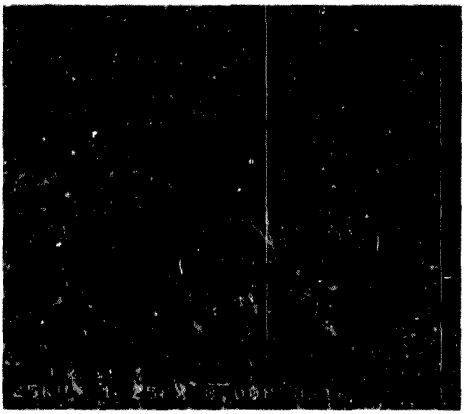

Figure 5.52

Typical ductile striated growth. Note directionality of striations. 0.9 R-ratio, Argon, 3 Hz. Mag. x 1250

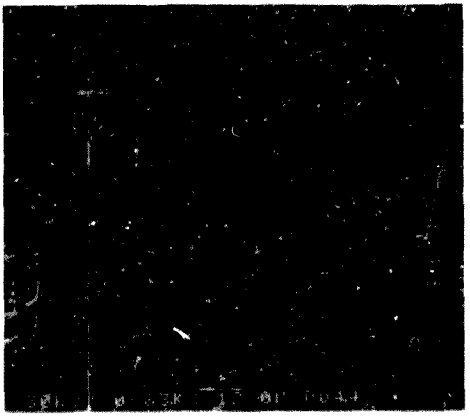

Crack growth direction.

Figure 5.53 12 μm

View at near threshold ΔK levels. Highly directional tear ridges. 0.9 R-Ratio, PWR Water, 3 Hz Mag. x 830

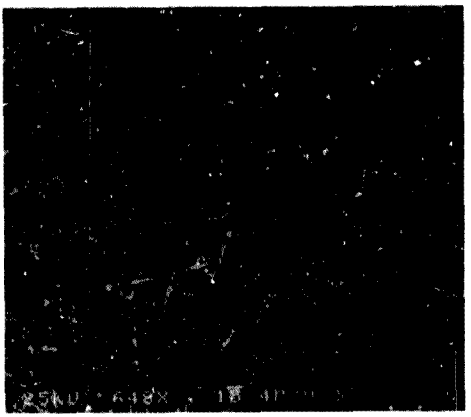

Crack growth direction.

Figure 5.54 13 μm

Ductile striated fatigue failure. Note small isolated IG facet 10-15 μm. 0.9 R-Ratio, PWR Water, 3 Hz Mag. 648

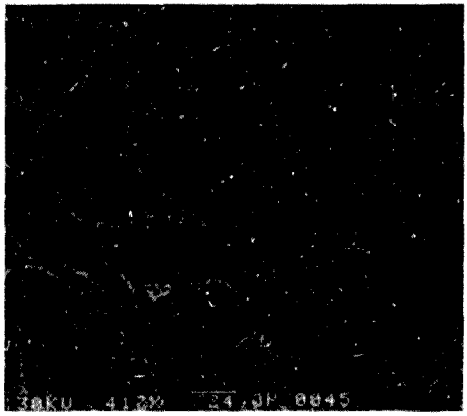

crack growth direction.

Figure 5.54 — 24 μm

Fast failure region. Note microvoid coalescence. Dimple size ~ 30μm. 0.9 R-ratio, PWR Water, 3 Hz. Mag. x 417

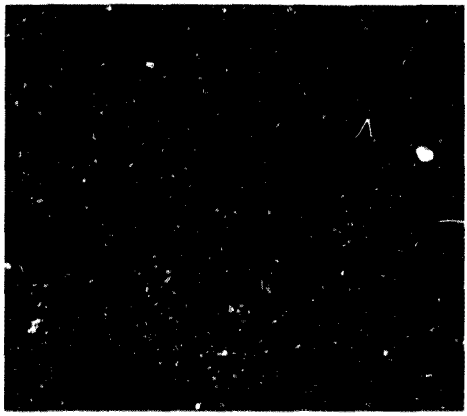

Crack growth direction.

Figure 5.56 55 μm

Region just ahead of precrack showing 18% IG failure. ΔK = 5.6 MPa√m. 0.9 R-Ratio, PWR Water, 0.3 Hz. Mag. x 181

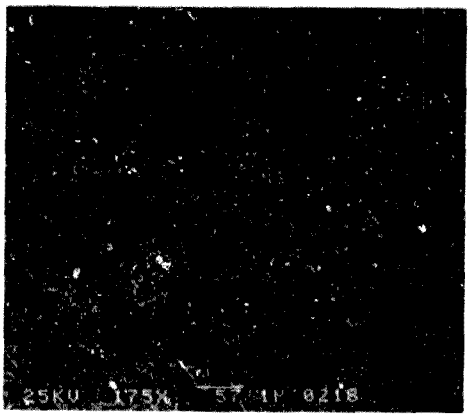

Crack growth direction.

Figure 5.57 57 μm

General view at ΔK = 6 MPa√m. IGF = 12%.
0.9 R-Ratio, PWR Water, 0.3 Hz. Mag. x 175

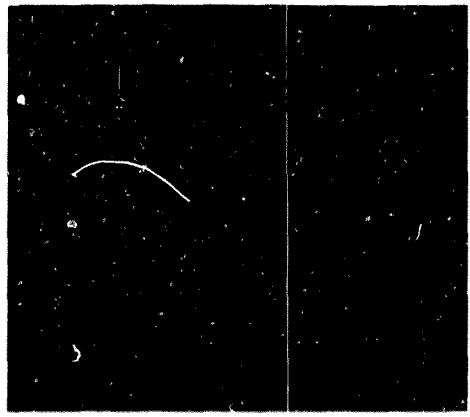

Crack growth direction.

Figure 5.56 55 μm

Region just ahead of precrack showing 18% IG failure. ΔK = 5.6 MPa√m. 0.9 R-Ratio, PWR Water, 0.3 Hz. Mag. x 181

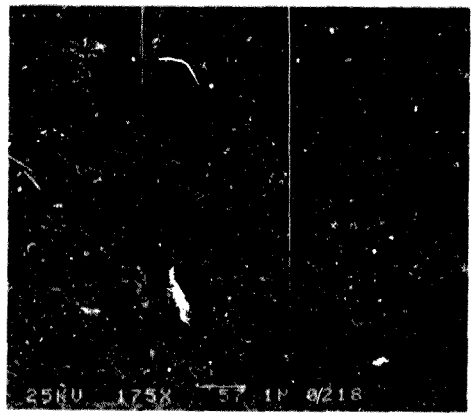

Crack growth direction.

Figure 5.57 57 μm

General view at ΔK = 6 MPa√m. IGF = 12%.
0.9 R Ratio, PWR Water, 0.3 Hz. Mag. x 175

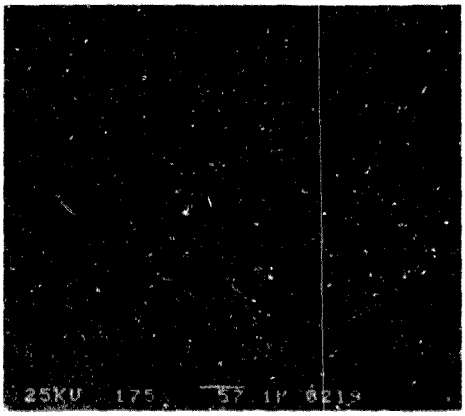

Figure 5.58 57 μm

General view at ΔK = 6.1 MPa√m IGF = 7%.
0.9 R-Ratio, PWR Water, 0.3 Hz. Mag. x 175

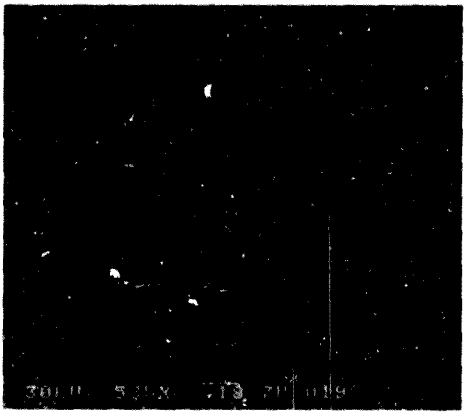

Figure 5.59 19 μm

General view at ΔK = 6.8 MPa√m IGF = 1%.
0.9 R-ratio, PWR Water, 0.3 Hz. Mag. x 535

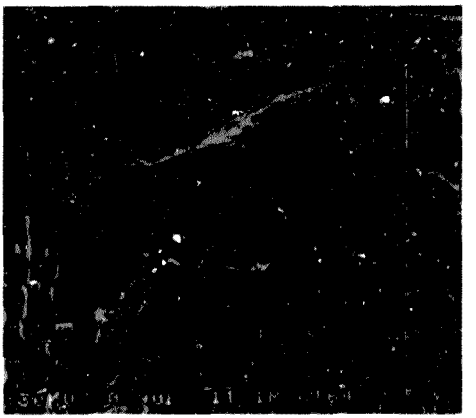

Crack growth direction

Figure 5.60 [illegible] 11 μm

Detailed view of 2G facets. Facet size 10-30 μm.
0.7 R ratio, PWR Water, 0.3 Hz. Mag. x 900

Crack growth direction.

Figure 5.61 16 μm

Ductile striated growth with microvoid coalescence.
0.9 R-Ratio, PWR Water, 0.3 Hz. Mag. x 713

Crack growth direction.

Figure 5.62 6 μm

Detailed view of microvoids. ΔK = 11 MPa/m.
0.9 R-ratio, PWR Water, 0.3 Hz. Mag. x 1820

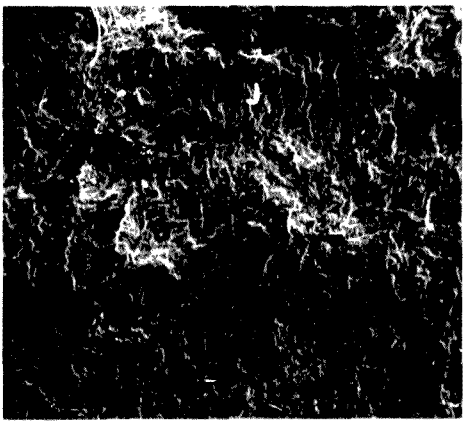

Figure 5.63 50 μm

Fracture surface showing precrack, fatigue crack growth and final cleavage fracture. Peaks, Argon, 3 Hz. Mag. x 200

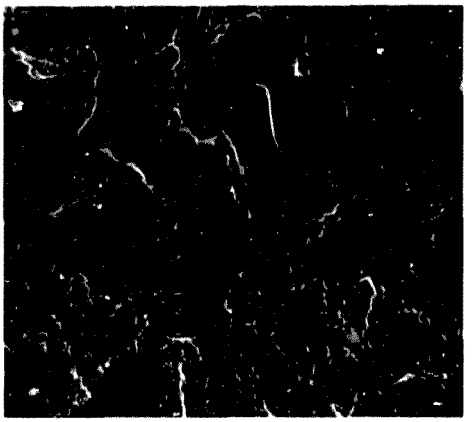

Figure 5.64 20 μm

General morphology of air/argon interface. Note striated growth not very evident. Peaks, Argon, 3 Hz. Mag. x 500

Argon

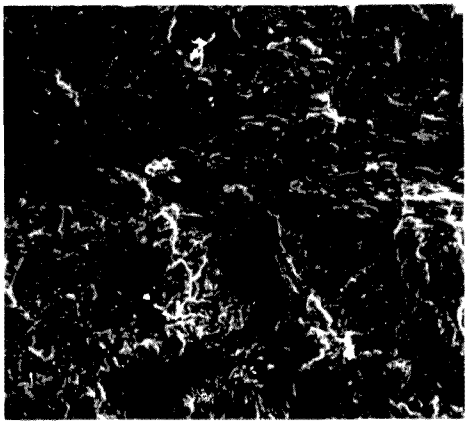

Air

Crack growth direction.

Figure 5.65 10 μm

Air/Argon interface. Note striated growth more evident.
Trapezoidals, Argon, 3 Hz. Mag. x 1000

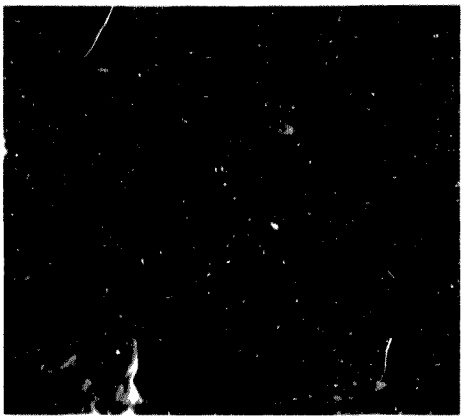

Crack growth direction.

Figure 5.66 2 μm

Striations clearly evident.
Trapezoidals, Argon, 3 Hz. Mag. x 5000

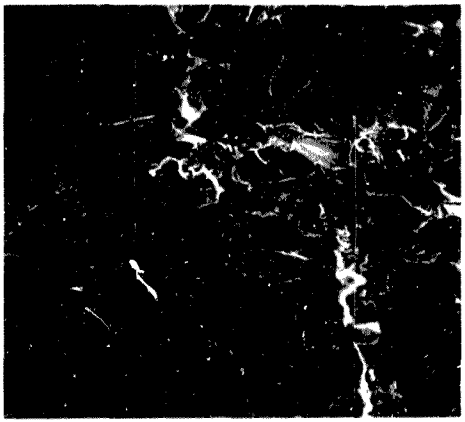

Figure 5.67 10 μm

Final fracture/fatigue interface.
Spectrum Argon, 3 Hz. Mag. x 1000

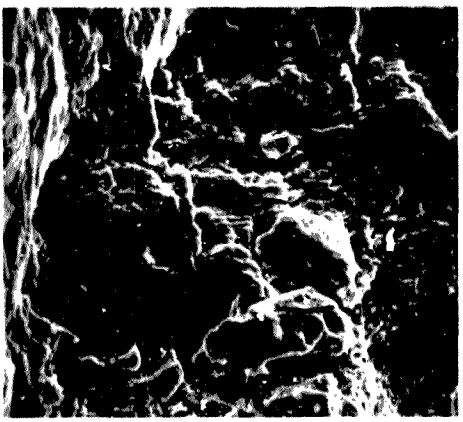

Figure 5.68 5 μm

Higher magnification shows fine striations
Spectrum Argon, 3 Hz. Mag. x 2000

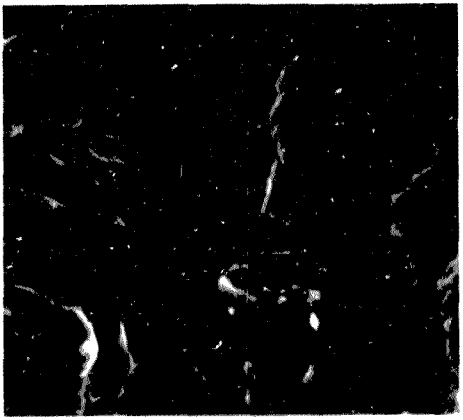

Crack growth direction.

Figure 5.69 2 μm

Ductile striations clearly visible.
Spectrum Argon, 3 Hz. Mag. x 5000

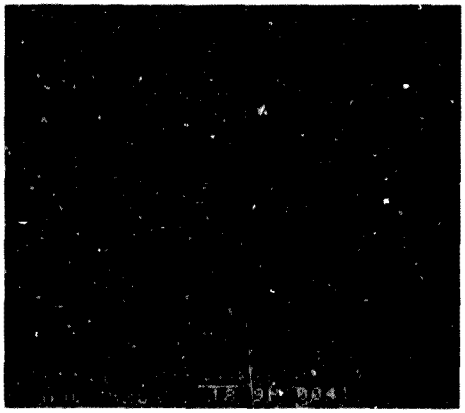

Crack growth direction.

Figure 5.70 19 μm Mag. x 538

General view of ductile striated growth. Note cluster of MnS inclusions with some inclusions still in place. Spectrum Argon, 3 Hz.

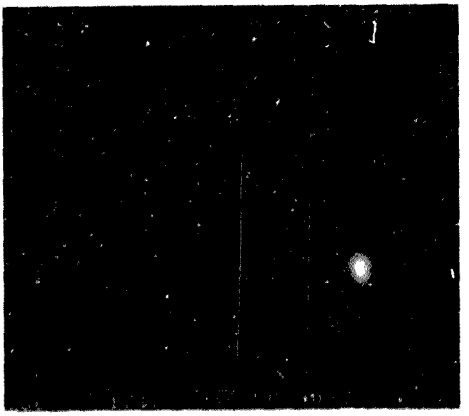

Crack growth direction.

Figure 5.71 58 μm

Ductile striated growth with isolated IG facets.
Peaks, PWR Water, 3 Hz. Mag. x 173

Crack growth direction.

Figure 5.72 12 μm

Detailed view of IG facets.
Peaks, PWR Water, 3 Hz. Mag. x 550

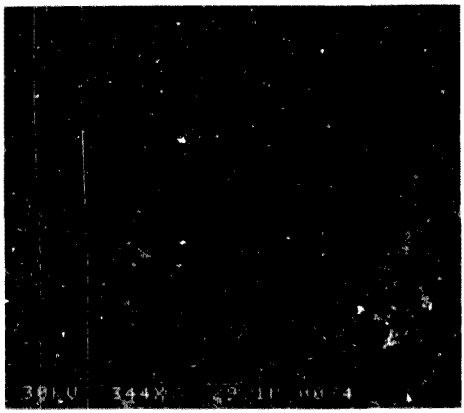

crack growth direction

Figure 5.23 20 μm

Isolated fan-shaped region in which ductility is markedly reduced. Trapezoidal, PWR Water, 3 Hz. Mag. x 561

Crack growth direction.

Figure 5.74 ——— 12 μm

Ductile striated growth.
Spectrum, PWR Water, 3 Hz. Mag. x 820

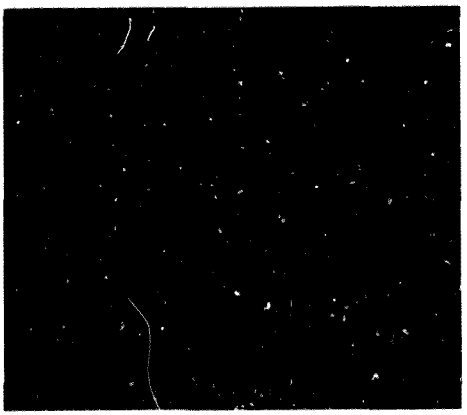

Crack growth direction.

Figure 5.75 ——— 79 μm

MnS inclusion cluster just ahead of precrack.
Spectrum, PWR Water, 3 Hz. Mag. x 126

Air

PWR Water

Crack growth direction.

Figure 5.76 30 μm

Detailed view of inclusion cluster. Most inclusions are dissolved out. Spectrum, PWR Water, 3 Hz. Mag. x 336

Crack growth direction.

Figure 5.77 12 μm

View of Elephant's Trunk caused by some hard debris impacting the surface. Spectrum, PWR Water, 3 Hz. Mag. x 840

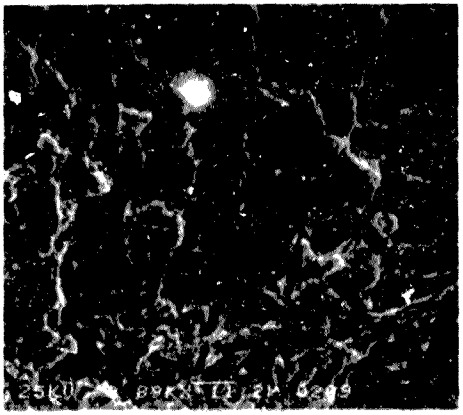

Crack growth direction.

Figure 5.78 ——— 11 μm

General view of flat featureless region.
Spectrum, PWR Water, 0.3 Hz. Mag. x 890

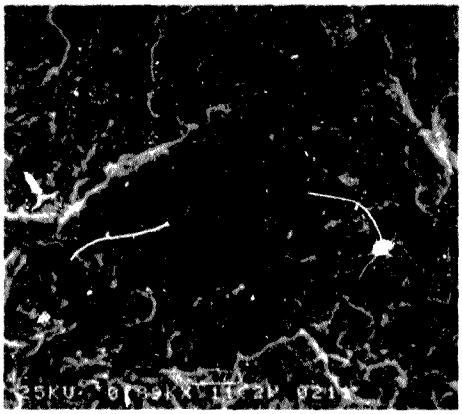

Crack growth direction.

Figure 5.79 ——— 11 μm

Note river type lines emanating from a point source P.
Spectrum, PWR Water, 0.3 Hz. Mag. x 890

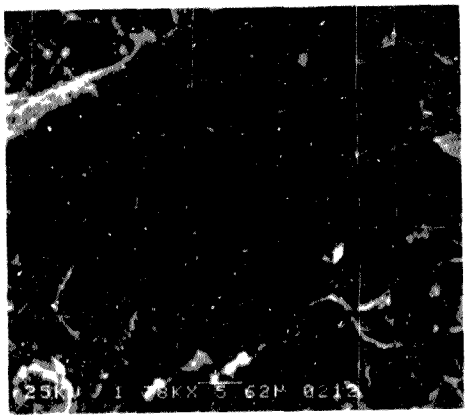

Crack growth direction.

Figure 80 [illegible] 9 μm

Detailed view of initiation point P. Possibly large carbide or small inclusion. Spectrum, PWR Water, 0.3 Hz. Mag. x 1'80

TABLE 5.1 : RESULTS OF VARIABLE LOADING SEQUENCES

Type	Blocks	Env	a_i mm	a_f mm	Δa mm	ΔK MPa $\sqrt{m}$	da/dN mm/cycle	Env Factor
Ripples (Trans. C)	500	Argon (3 Hz)	19.63	19.78	0.15	5.80	1.97×10^{-7}	-
		PWR (3 Hz)	19.50	20.00	0.50	5.84	6.56×10^{-7}	3.3
		PWR (0.3 Hz)	19.16	21.36	2.20	6.26	3.19×10^{-6}	16.2
Peaks (Trans. B + C)	500	Argon (3 Hz)	20.50	20.92	0.42	15.06	5.49×10^{-7}	-
		PWR (3 Hz)	20.48	21.89	1.41	15.83	1.84×10^{-6}	3.4
Trapezoidals (Trans.A + C)	500	Argon (3 Hz)	19.82	20.15	0.33	31.67	4.40×10^{-7}	-
		PWR (3 Hz)	19.99	21.14	1.15	33.27	1.51×10^{-6}	3.5
Spectrum	500	Argon (3 Hz)	19.98	21.65	0.67	30.46	8.75×10^{-7}	-
		PWR (3 Hz)	20.29	22.85	2.56	32.49	3.03×10^{-6}	3.5
		PWR (0.3 Hz)	19.38	22.53	3.23	31.95	5.65×10^{-6}	6.5

Argon

Ripples.		0.15
Peaks.	0.42 - 0.15 =	0.27
Traps.	0.33 - 0.15 =	0.19
		0.60
Spectrum		0.67

PWR

Ripples.		0.50
Peaks.	1.41 - 0.50 =	0.91
Traps.	1.15 - 0.50 =	0.65
		2.06
Spectrum		2.56

6 DISCUSSION

6.1 Constant Amplitude Loading

6.1.1 Environment

Generally in PWR water many more inclusion clusters were encountered by the advancing crack than in air, while in a pure argon environment little or no inclusions were observed on the fatigue fracture surface. The effect of environment was more obvious at 1 Hz than at 10 Hz for both waveforms investigated and consequently only the 1 Hz data need be discussed. The differences in growth behaviour between the argon and PWR water tests can only be explained in terms of hydrogen embrittlement effects.

6.1.1.1. Argon Environment

The effect of a pure argon environment on the fatigue crack growth rate was essentially insensitive to frequency over the range 1 to 10 Hz. In general growth rate data in argon was slightly slower than air growth data and appreciably slower than PWR fatigue crack growth data. The present fatigue crack growth data in argon agree well with the results from reported vacuum data [65] and McMinn's argon data [66] (Figure 6.1).

Fractographic examination of the fracture surfaces for positive sawtooth both at 1 and 10 Hz (Figures 5.23 and 5.31) and for sine wave (Figure 5.38) revealed that the fracture mode was ductile striated growth. Many workers [67-70] have tried to characterize the parameters which affect the relationship between fractographic features and fracture mechanics data for fatigue failures. However, to date, no single rationale exists that adequately explains the phenomenon of striation formation.

Laird [67] suggested that striations are formed as a result of plastic blunting of the crack tip (Figure 6.2). During the tensile part of the load cycle plastic blunting of the crack tip occurs, this is then followed by resharpening of the tip during the compression part of the cycle. Laird's model therefore accounts for the presence of fatigue striations in non-crystalline, as well as crystalline materials. Hertzberg [68] attempted to show that crystallographic considerations could be used to explain the sawtooth apparance of the striations however his model lacked experimental evidence. Pelloux [69] followed this up by showing that the formation and orientation of fatigue striations depended upon the crystallographic orientation of the grains and also that a process of deformation by alternating shear results in an extension of the notch length by a rupture mechanism (Figure 6.3).

Meyn [70] was among the first to show that fatigue striations are not formed when the fatigue crack propagation test is performed in vacuum. This observation negates the validity of the plastic blunting theory for the formation of striations (at least for low growth rates). This lack of striations was explained as the effect of "an environmental cracking of an unspecified nature" during testing in air and by the fact that no environmental cracking occurs in vacuum. Pelloux clarifies this environmental cracking as an oxide layer which immediately forms on crack surface exposed to air (Figure 6.4). This oxide layer will then limit the amount of reversibility of the deformation at the tip. However, Lankford and Davidson [71] found striations in vacuum.

In the case of the present study several factors need to be considered when describing these fractographic features. Firstly, the tests were conducted in high purity argon and not vacuum. The 99.95% pure argon represents a rather poor vacuum of about 10^{-3} Torr, thus sufficient active ingredients may be present to form a monolayer of oxide on the fracture surfaces. Secondly Kendell and Knott [72] also showed that monolayers of relatively inert gases such as argon can be adsorbed onto the fracture surface. Thirdly stage II growth rates were measured for all the tests conducted in argon. From these considerations it would

appear that both the Laird and the Meyn model can be used to explain the appearance of striations on the fracture surfaces. Yet, only Meyn's model can suitably tie up both the fractographic features and the crack growth data.

In the present study the crack growth rate differences observed in air and PWR water when compared to argon can best be explained in terms of a hydrogen embrittlement mechanism. Hydrogen embrittlement occurs as a result of the reaction between "hydrogen containing" environments and the freshly exposed atomically clean material at the crack tip which produces hydrogen ions which cause embrittlement. In an inert environment the absence of "hydrogen producing" species would explain the frequency independence of SA 508 cl III material recorded in the present study. The almost total absence of moisture in the pure argon environment would therefore lead to a fracture mode that was cycle dependent rather than time dependent. In the present study there is little effect of waveform and frequency in an argon environment.

6.1.1.2 PWR Water

The effect of an aqueous environment is directly related to the frequency of the test. The slower the frequency the greater the environmental effect. This can be seen in that the 0.1 Hz test exhibited EAC plateau growth rate, see Figure 5.9, while the 1 Hz crack growth rate in PWR water was approximately 5 times faster than the argon data, and the air data resided slightly above the argon data (Figure 6.1). Data from the present study agrees well with McMinn's [66] 1 Hz ambient temperature PWR water data as well as Amzallag's [41] 1 Hz at 288°C PWR data, but is 2 times faster than Bulloch's [15] 1 Hz at 290°C PWR water data for a triangular waveform. Comparisons cannot be made with the ICCGR group data since most of their tests were conducted at 1 cpm and at 290°C. The main findings of their 1 cpm data was the existence of EAC plateau formation at much higher crack growth rates and ΔK levels.

Fractographic examination revealed that the effect of PWR water resulted in a significant amount of intergranular failure in the case of the 0.1 Hz test at initial ΔK levels (Figure 5.46). With increasing ΔK level the extent of intergranular failure decreased and at ΔK = 40MPa/m the failure mode was predominantly ductile striated growth within which were dispersed isolated "brittle" like fan-shapes (Figure 5.47). The existence of such intergranular failure at low ΔK levels caused the formation of the EAC growth rate plateau. In the case of the 1 Hz test the fracture mode was ductile striated growth with isolated fan-shaped regions of reduced ductility (Figures 5.35 and 5.41).

Thus the effect of PWR environment with reference to the air data can be explained in terms of the findings of Klemetti et al [20] who found that at ambient temperature and pressure some dissolution of MnS inclusions was observed already after only 20 hours. This was confirmed by the fractographic examination of the PWR specimens of the present study which showed partially dissolved MnS inclusions in the fracture surface (Figure 5.43). The dissolution of MnS inclusions in acid conditions is more pronounced when compared to neutral water conditions. On the other hand the hydrolysis of the metal ions lead to local acidification [24], which may provid conditions for chemical dissolution. It is therefore evident that MnS inclusions on the steel fracture surface can provide initiation sites for EAC growth. This is borne out by the presence on the fracture surface of fan-shaped regions of reduced ductility ahead of the inclusion clusters. Several workers [15,23,27,44] have also observed this phenomenon and have shown that a EAC plateau occurred as the area fraction of fan-shaped fracture abruptly increased. When considering a growing crack it is obvious that the MnS inclusions which are exposed to the environment inside the crack can dissolve. The dissolution is enhanced since the environment inside the crack is expected to become more acidic. The MnS inclusions inside the crack act as local cathodes and dissolve forming H_2S. Thus the dissolution of the MnS inclusion produces H_2S saturated water at the crack tip. The poisoning effect of the resulting H_2S retards the recombination of atomic hydrogen into molecular hydrogen and hydrogen absorption into the metal is enhanced. Also the hydrogen atom may be easily

dissociated from H_2S.

Beachem's model [27], see Figure 6.5, suggested that initially for an increasing K situation when the critical combination of hydrogen concentration for a given stress intensity is achieved intergranular failure can occur. In the 0.1 Hz test the crack front encountered a band of MnS inclusions which were dissolved by the PWR water resulting in H_2S production at the crack tip. This then led to greater hydrogen generation and diffusion into the metal matrix. The combination of this hydrogen concentration and the level of the initial stress intensity caused extensive intergranular failure (36%) during the early stages of the fatigue test.

The Harwell data [73], see Figure 6.6, which indicate only minor environmental influence, may be explained as resulting from the high flow rate (turbulent) of the recirculating water. This turbulent water flow may prevent the formation of the necessary crevice chemistry conditions inside the crack, which can decrease the rate of dissolution and subsequent hydrogen evolution reactions and result in a reduced environmental influence. The clear environmental influence in fatigue crack growth rates indicate that the dissolution of MnS inclusions occurs and favourable conditions for hydrogen evolution and absorption are created. Thus the development of the crevice chemistry inside the crack is of great importance.

The results of Amzallag [41], Bulloch and Buchanan [15] and McMinn [66] and the present study all indicate that hydrogen evolution and absorption while leading to enhanced crack growth is not sufficient to cause EAC plateau effects. This is probably due to the fact that at 1 Hz the crack velocity is still greater than the rate of hydrogen accumulation despite the high temperatures in some cases. The lower growth rate obtained by Bulloch and Buchanan [15] for triangular wave 1 Hz at 290°C in PWR water can be attributed firstly to, the relative cleanliness of the EPRI steel compared to the present steel and secondly to waveform effects. Bulloch and Buchanan [15] suggested that the lower growth rates found for triangular waveform compared with those of the sine wave could be explained in terms of crack tip

closure effects. The crack tip strain rate range of the sinusoidal waveform is much greater than that of the triangular waveform. This difference in crack tip strain rate behaviour at low values of ΔK_{eff} together with the fact that during sinusoidal waveform loading the crack tip is opened for a longer period, could prevent passive film formation and hence facilitate hydrogen absorption and thus environmentally enhance crack growth. Thus, despite the increase in temperature which would aid the MnS dissolution the greater preponderance of MnS inclusions found in the present steel can lead to more H_2S formation and thus greater hydrogen absorption. In the case of Amzallag's results it can only be surmised that the steel used was relatively clean and that the increased growth rate was due to waveform effects.

6.1.2 Frequency

The only significant effect of frequency was found in PWR water at a frequency of 0.1 Hz where a growth rate plateau and hence environmentally assisted cracking was observed (see Figure 6.6). It should be noted that the International Cyclic Crack Growth Rate (ICCGR) Round Robin data (1 cpm at 290°C) agrees well with the present data at ΔK levels of approximately 30 MPa$\sqrt{m}$. However, at ΔK levels above 30 MPa$\sqrt{m}$ the ICCGR band [74] exhibits growth rate values that are in some cases an order of magnitude greater than the present results. High flow rate data [73] (Harwell 1 cpm at 290°C) and Babcock Power Limited (BPL) data [15] (1 Hz at 290°C) shows good agreement with the present data inasmuch that these data also show little environmental assisted crack growth. McMinn's data [66] (0.1 Hz at ambient temperature PWR water) agrees well with 0.1 Hz data of the present study in that it also shows evidence of environmentally assisted crack growth starting at approximately 28 MPa$\sqrt{m}$. In the present study the growth rate plateau started forming at a ΔK level of 24 MPa$\sqrt{m}$ and the crack growth rate remained almost insensitive to ΔK values up to 40 MPa$\sqrt{m}$. For the Round Robin tests conducted by the ICCGR group, the majority of growth rate plateaux were formed at ΔK levels approaching 40 MPa$\sqrt{m}$.

Sulphur prints [1] taken from the steel used in the present study show the material to be prone to gross segregation and exhibited much evidence of MnS clusters while the Electric Power Research Institute (EPRI) steel, used in the ICCGR Round Robin test programme is reported [75] to be fairly clean. Since the stress intensity range at which the plateau formed, ΔK_{plat}, in the present study is much lower than that found in the ICCGR Round Robin tests, this would suggest that steel cleanliness could be dominant cause of the lower ΔK_{plat}.

However the present study was conducted at ambient temperature and hence a less aggressive environment in which MnS inclusions were only partially dissolved. Coupled with the lower ΔK_{plat} the present l n .ack growth data is approximately double the BPL data or EPRI steel growth rate. This would suggest that the inclusion content/cleanliness/segration effects can play a dominant role in EAC growth.

At the onset of plateau growth rate two fracture mechanisms were observed viz. transgranular ductile striated growth and intergranular failure. This can be seen in Figures 5.45 and 5.46 which show that 36% of the area at the start of EAC g owth (ΔK = 24MPa$\sqrt{m}$) consisted of intergranular failure (IGF). This fracture mode was transient and the area percentage of (IGF) decrea s with increasing ΔK level viz. 22% IGF at ΔK = 25 MPa $\sqrt{m}$ to 4% IGF at ΔK =26MPa$\sqrt{m}$. These percentages o intergranular failure agree well with the data portrayed by Cooke et al [76] for a medium carbon steel tested in air.

Beachem [27] in his model for Hydrogen-Assisted Cracking suggested that hydrogen diffusing into the lattice just ahead of the crack tip will aid whatever deformation process the matrix (microstructure) will allow (Figure 6.5). Such deformation processes also depend upon the stress intensity factor and the hydrogen concentration at the crack tip enclave. At slow crack growth rates IGF is an energetically more favourable process than the kinetically faster microvoid coalescence and quasi-cleavage processes. Thus, hydrogen will diffus further ahead of the crack tip permitting a hydrogen concentration at the grain boundaries and making the conditions for grain boundary

plasticity more favourable. Cooke et al [76] found that the transition from microstructure sensitive behaviour to microstructure insensitive behaviour occurred when the reversed plastic zone size approaches the relevant microstructural dimension, eg. the prior austenite grain size. Although this correlation is encouraging, the reversed plastic zone size was calculated to be 7.39×10^{-5} mm at the end of intergranular failure. This dimension is approximately four times larger than the reported grain size of 17 μm [77].

Fractographic observations support the Hydrogen Assisted Cracking (HAC) model as the fracture mechanism, since more non-metallic inclusion clusters were encountered by the advancing crack front in the 0.1 Hz test than in both the 1 and 10 Hz PWR water tests. In fact there was increasing evidence of inclusion clusters with decreasing frequency. This can be attributed to the increase in loading time in which liberated atomic hydrogen can diffuse through the lattice and embrittle the metal. Furthermore, hydrogen tends to accummulate at grain boundaries, inclusions, voids, dislocation arrays and solute atoms and thus the extent of HAC is controlled by those hydrogen accummulation sites that are most sensitive to fracture. From this it becomes clear that the the test frequency determines the rate of hydrogen supply which in turn leads to the various fracture mechanisms.

At the relatively high frequencies of 1 and 10 Hz the hydrogen supply is low and for low ΔK levels few inclusion sites are located in the area of maximum triaxial stress ahead of the crack tip which by nature are preferential sites for hydrogen trapping. However, for intermediate ΔK levels (increased plastic zone size) more sites are present and thus a larger accummulation of hydrogen can occur. Also, trapped hydrogen and the microcrack type behaviour of the inclusions together with the stress field ahead of the crack tip can cause hydrogen induced cracking around the inclusion. This leads to fan-shaped regions of reduced ductility just ahead of the MnS inclusion cluster as seen in Figures 5.28 and 5.35. At lower frequencies (i.e. 0.1 Hz), on the other hand there is a much greater hydrogen supply and yet for low ΔK levels still few inclusions are present in the forward

plastic zone, therefore the hydrogen accummlates at the grain boundaries. This then leads to environmentally assisted cracking (EAC) by intergranular failure as seen in Figures 5.45 and 5.46. As the ΔK level increases (with a corresponding increase in the plastic zone size) there is a greater likelihood that more inclusion clusters can be sampled; such clusters are preferential "hydrogen sinks" and this together with the faster crack velocity enhances the occurrence of quasi-cleavage fan-shaped EAC growth, see Figure 5.46.

Abrupt changes in crack growth rate establishing plateau regions in the fatigue crack curve have been related to an environmentally controlled phenomenon. At low values of ΔK, the effect of increasing K on both the stress and hydrogen at the crack tip combine to produce a rapid increase in the crack growth rate. As the crack extension rate accelerates it eventually reaches a velocity where the kinetics of hydrogen entering into the crack tip are not sufficiently fast enough to produce the hydrogen concentration needed for further accelerated growth. The fatigue crack growth then slows down to a rate determined by the rate of hydrogen accumulation, becoming only weakly dependent on ΔK.

The preponderance of MnS inclusions encountered in the present study not only explains the lower ΔK_{plat} observed but also the high crack growth rate of the 1 Hz data over that of the BPL data despite its higher testing temperature. The Harwell data while at a higher temperature (290°C) and a slower frequency (0.017 Hz) agrees well with the present 1 Hz data and exhibits no growth rate plateau. This could be due to the high flow rate of the circulating PWR water, prevalent within the Harwell testing facilities which could flush out the dissolved MnS environment from the crack into the bulk liquid and possibly slow down the rate of hydrogen entering the steel. The higher plateau formed by the IGCGR group data can be attributed to the lower frequency (0.0167 Hz) used for these tests and/or the higher temperature used, i.e. the lower frequency will lead to greater hydrogen accumulat. ; while the increased temperature will cause a faster dissolution rate of the MnS to produce an aggressive crack tip environment which in turn can lead to further hydrogen evolution.

6.1.3 Waveform

From a fractographic aspect waveform effects were negligible in all three enviroments, also similar fractographic details were observed for both waveforms tested in this study. For both the 1 and 10 Hz argon tests far fewer MnS inclusion clusters were encountered by the advancing crack front than in the air. The fracture mode was ductile striated growth (Figure 5.23) and in the few instances where the growing crack front cut through an inclusion cluster, each individual inclusion was separated from the matrix by voids formed through differential thermal contraction during cooling as in Figure 5.26. The tests conducted in PWR water showed more evidence of MnS inclusions being encountered by the growing crack front than for both the air and argon tests. A decrease in frequency from 10 Hz to 1 Hz increased the incidence of MnS inclusions encountered by the crack front and hence the incidence of brittle "fan shapes" extending ahead of the inclusion clusters (Figure 5.35), furthermore, the inclusions were partially dissolved and many could still be seen in their sites (Figure 5.36).

Positive sawtooth waveform consistently gave faster crack growth rates than sine wave although the extent varied depending on the environment and in some instances frequency. However, the fastest crack growth rates for both waveforms was observed at the slowest frequency in PWR water. Two difficulties arise with the interpretation of these results. Firstly, an accurate comparison of the various waveforms should be on the basis that the transient stresses are equal in rate and duration. Secondly, most of the work done in corrosion fatigue of RPV steels in PWR water was done at 290°C using sine or triangular waveforms thus there is very little suitable data with which to compare. For these reasons comparisons will only be made between the two waveforms used in this investigation.

For the tests done in argon there was little difference in both the 1 Hz and 10 Hz crack growth data for both waveforms.

In air the corresponding crack growth rates for the various waveforms are higher than those in argon and the difference in the crack growth rates for the two waveforms also increased. The fact that at 1 Hz the crack growth rates are essentially the same as for 10 Hz indicate that there is little effect of frequency and that the difference is mainly the result of waveform effects. The significant oxygen and moisture contents prevalent in the air result in the rapid formation of an oxide layer that will in turn lead to a faster dislocation pile up giving faster crack growth rates in air for positive sawtooth loading.

For the PWR environment a similar trend is observed i.e. individual crack growth rates are higher. However, as the frequency is reduced the crack growth rates increase which is the result of an increase in the environmental component. A greater loading period, such as that prevalent in the positive sawtooth tests, causes more hydrogen to diffuse into the metal and to the region of greatest stress triaxiality where it will accumulate and cause embrittlement. Further, not only does hydrogen diffuse rapidly through the lattice because of its small size but potentially of greater significance is the fact that hydrogen transport rates in association with dislocation motion can be several orders of magnitude greater than that associated with lattice diffusion Beachem's model [27] suggested that hydrogen does not lock dislocations in place but rather unlocks them and allows them to multiply or move at reduced stresses. Thus the dissolved hydrogren lowers the true fracture strength of the lattice. During the rapid loading period, as in the sine wave, embrittlement does not occur during the loading cycle since the hydrogen does not have time to diffuse to the crack tip. At large ΔK values the strain rate dependence diminishes since the large K_{max} value provides sufficient driving force for both the mechanical and hydrogen diffusion mechanisms and hence the sinusoidal and positive sawtooth data tend to merge at high ΔK values.

6.1.4 High R-Ratio Tests

Argon Tests

The present constant amplitude argon data together with that reported for Ducol steel by Bulloch and Buchanan [64] represent near-threshold growth data at R=0.9 and a smooth continuous extrapolation from this low growth rate data to intermediate ΔK levels seems reasonable. It is also reasonable to assume that A508 cl III and Ducol steel will have similar threshold characteristics because they are both low alloy ferritic pressure vessel steels with very similar strength properties.

Load ratio and microstructure are considered to be major variables which affect the fatigue crack growth rate behaviour at both the near-threshold and high ΔK levels. However, in the intermediate growth rate regime load ratio and microstructure do not have nearly such a pronounced effect on fatigue crack propagation and indeed fatigue crack propagation at intermediate ΔK levels is relatively microstructure insensitive. In almost every case, the transition from microstructure-sensitive to microstructure insensitive crack growth behaviour is associated with a concomitant transition in fracture mode [78]. These fractographic observations strongly suggest the role of microstructural influences on the determination of the operative micromechanisms of fracture.

It was apparent, however, from the work done by Bulloch and Buchanan [64] and from the fractographic evidence of the present study (Figures 5.51 and 5.52) that the growth rate in argon was unaffected by R-ratio and the fracture mode remained microstructure insensitive. These facts, particularly the latter, suggest that a continuum type mechanism (plastic blunting [67] or shear band decohesion [69]) may be the fundamental mechanism of crack growth. Thus the absence of a relatively benign environment (in the case of the R=0.9) resulted in a reduced crack growth rate because the absence of a hydrogen producing species prevented any hydrogen assisted cracking.

It is interesting to note that in the region of the crack that was precracked in air the striations are more distinct when compared to the striations formed in argon. (Figur [illegible]). These results are in good agreement with the findings of [illegible] et al [76] for vacuum tests and tend to support Pe[illegible]'s [69] findings.

Suresh et al [54], however, found that both hydrogen and dry argon gave accelerated near-threshold fatigue crack growth rates relative to air. In explaining this enhanced growth rate they noted that fatigue testing in air creates an oxide layer on the fracture surface that thickens in the threshold regime as a result of closure-induced fretting. Similar oxide layers in the threshold regime have been reported by Cooke et al [76]. The thicker oxide layer, would increase the crack opening stress intensity, K_{op}, and bring about a corresponding decrease in the effective stress intensity range, ΔK_{eff}, thereby leading to lower crack growth rates at a given applied ΔK. While at a first glance this may appear to contradict the results found in the present study it must be borne in mind that Suresh's findings apply to low R-ratio tests. For high R-ratio tests there is little chance of crack closure, this resulted in no thickening of the oxide layer and no increase in the crack opening stress intensity. Thus the crack growth rate for a high R-ratio test in air should be greater than that of a low R-ratio test.

PWR Water Test

The most significant effect was that of frequency on the Ripples (R=0.9) loading sequence; in which decreasing the frequency from 3 Hz to 0.3 Hz resulted in increased the crack extension from 0.50 to .20 mm. This corresponded to a 65% as opposed to a 23% contribution to the spectrum crack extension. Therefore at high frequencies despite the fact that the R=0.9 loading sequence constituted the most cycles, its contribution to crack extension was small (23%) whereas at lower frequencies this R-ratio became a dominant contributing factor in spectrum loading crack extension. This was due to enhanced growth rates that resulted from the occurrence of a significant amount of intergranular

failure on the fatigue fracture surface.

Fractographic examination of the 3 Hz R = 0.9 test showed that the dominant fracture mode was ductile striated growth (Figure 5.53). However, small isolated intergranular facets were also found in the fracture surface (Figure 5.54). In the fast failure region the fracture mode was microvoid coalescence (Figure 5.55). The 0.3 Hz R = 0.9 test showed that at the start of the fatigue test a mixed fracture mode of intergranular failure and ductile striations was operative. With increase in ΔK level the percentage of intergranular failure decreased from 18% to < 1% at ΔK = 6.8 MPa√m (Figures 5.56 - 5.59). Once again in the fast failure region the fracture mode was microvoid coalescence (Figure 5.61) with microvoids of about 10 um in size.

The environmental enhancement factor, in PWR water after 500 blocks, for relatively high frequency (3 Hz) ranged between 3 and 4 while that for lower frequency (0.3 Hz) was greater than sixteen. Both these enhancements can be described by the hydrogen assisted cracking model. The "high" frequency results can be explained as described in section 6.1.1.2 above, while the "low" frequency results can be described by two hydrogen models proposed by Irving and Kurzfeld [79] and Beachem [27] described below.

Irving and Kurzfeld [79] suggested that the crack velocity in a moisture containing environment was the parameter which determines the proportion of intergranular failure. Hydrogen which formed at the crack tip on each load cycle diffused into the plastic zone and caused local reduction of cohesive strength of the grain boundaries. The critical areas would be the region of maximum hydrostatic stress, as tensile stresses normal to the crack plane would also be a maximum in this region. The operation of such a mechanism would be limited by the rate of supply of hydrogen. At high crack velocities (Figure 6.7) there would be insufficient time for hydrogen to diffuse to the region of maximum triaxial stress and intergranular failure would decline. At low crack velocities the rate of hydrogen production at the crack tip will be insufficient to promote grain boundary decohesion, and intergranular failure will again be reduced.

Clearly loading rate will change the transient rate of hydrogen supply to the region of maximum triaxial stress since only time under load and the crack growth increment will influence the average rate of hydrogen supply. The concentration of hydrogen at the crack tip does not matter whereas the concentration in the region of maximum triaxiality is important. Transient fluctuations in hydrogen production will tend to be smoothed in the diffusion process.

Rice and Johnson [80] on the basis of an elastic-plastic analysis of crack-tip stress fields have suggested that the distance of δ_t from the crack tip to the point of maximum triaxiality is,

$$\delta_t = \frac{K^2}{2 \sigma_y E}$$

where E is the elastic modulus and σ_y is the yield strength of the steel. This expression implies that δ_t will increase with increasing K level. The analysis also suggested that the stresses in the triaxial region did not continue to increase with increasing K, but instead extended over a larger distance ahead of the tip while remaining of the same size. This behaviour they suggested could account for the decrease in intergranular fracture observed at high values of R or of mean stress. It therefore follows that as the distance over which the hydrogen has to diffuse increases, the maximum achievable hydrogen concentration declines. In the absence of any additional tensile stress, intergranular fracture will also decline, and this is observed in tests on high purity macerial at high mean loads, or high R values.

Another model for Hydrogen-Assisted Cracking forwarded by Beachem [27] in fact agrees in many important aspects with the previous model. Namely; 1) hydrogen is evolved and enters the metal matrix at growing crack tips in aqueous environments, 2) pure molecular hydrogen gas dissociates at clean deforming surfaces and enters the metal matrix, 3) hydrogen migrates to regions of higher triaxial tensile stresses in the metal matrix, and 4) the presence of hydrogen dissolved in the ferrite matrix aids the

deformation of the matrix.

Beachem's model suggests that hydrogen diffuses into the lattice just ahead of the crack tip and aids whatever deformation processes the matrix will allow. Microvoid coalescence, quasi-cleavage or intergranular fracture are postulated to occur by these deformation processes, depending upon the stress intensity factor and the concentration of the hydrogen ahead of the crack tip. It is important to note that the model relates primarily to plasticity. The model predicts that at low K values the most energetically favourable fracture process is intergranular failure as opposed to the kinetically faster microvoid coalescence or quasi-cleavage, since these slower cracking rates permit hydrogen diffusion further ahead of the crack tip, giving rise to hydrogen concentration at the grain boundaries and making the conditions for intergranular failure more favourable. At intermediate ΔK levels the plastic zone which can be developed is not large enough to include large numbers of inclusions. Thus the K level is sufficient to drive the plastic deformation required in quasi-cleavage. At high ΔK levels large volumes of material are plastically deformed at the crack tip thus the resultant plastic zone can encompass numerous inclusions that act as void nuclei, the fracture process which develops is microvoid coalescence.

Cooke et al [76] found that in an air environment a new microstructure sensitive mechanism began to replace the vacuum mechanism when crack tip plasticity was confined to within microstructural dimensions. Using the continuum relationships developed by Rice [80], the maximum and reversed plane strain plastic zone sizes were calculated.

$$\text{Maximum plastic zone size} = \frac{1}{3\pi}\left[\frac{K_{max}}{\sigma_y}\right]^2$$

$$\text{Reverse plastic zone size} = \frac{1}{3\pi}\left[\frac{\Delta K}{2\,\sigma_y}\right]^2$$

Thus a two component mechanism was proposed to explain crack extension at low ΔK values in moist air environment. One component involved the creation of the intergranular facets by a ΔK controlled process and the second, a facet interconnection by a tensile tearing process i.e. K_{max} controlled.

The main differences between these two models are that firstly Beachem's model attempts to explain hydrogen assisted crack over the complete range of stress intensity from near-threshold to stage III crack growth while the other is a model for near threshold behaviour only. Secondly the Irving model predicts that at high crack velocities there is insufficient time for hydrogen to diffuse to the region of maximum triaxiality resulting in a decline in intergranular failure. Cooke et al [76] however found that when the reversed plastic zone size approaches the prior austenite grain size there is a transition from crystalline to non-crystalline failure i.e. at reverse plastic zone sizes large than the prior austenite grain size there will not be any intergranular failure. Beachem's model, however, suggests that hydrogen is in fact responsible for all the various fracture modes and that the failure mode depends on the complex interplay between hydrogen concentration at the crack tip, stress intensity factor and the microstructure.

The results of the present study can be explained in terms of the above models although certain contradictions exist, thus further research is necessary so that a model may be developed that may be applicable to all conditions. The contradictions were as follows;

(a) while both the 0.3 Hz, R = 0.9 test and the 0.1 Hz, R = 0.2 test showed that the crack extension was microstructure sensitive in that intergranular failure was the fracture mode (Figures 5.46 and 5.60) the transition from microstructure sensitive to microstructure insensitive fracture did not always occur at the predicted point inasmuch that,

(i) while for the 0.3 Hz R = 0.9 test at the point where the percentage of intergranular failure was < 1% (at ΔK=6.8 MPa$\sqrt{m}$ Figure 5.59) the reverse plastic zone size (~5 μm) was smaller than the prior austenite grain size, and the plastic zone was contained within it at lower ΔK values.

(ii) In the case of the 0.2 R-ratio test the point where 4% intergranular failure was present (at ΔK=26 MPa$\sqrt{m}$) the reverse plastic zone size (~74.2 μm) was larger than the prior austenite grain size of ~17μm [77].

(b) the crack velocities of both the R=0.9 and R=0.2 tests were below the level found by Irving to be too low for hydrogen production for hydrogen assisted cracking inasmuch that

(i) for the R=0.9 test the initial crack velocity of 5.4×10^{-7} mm/sec gave 18% intergranular failure while a velocity of 1.5×10^{-6} mm/sec gave < 1% intergranular failure and

(ii) for the R=0.2 the initial crack velocity of 3.59×10^{-5} mm/sec gave 36% intergranular failure while a velocity of 5×10^{-5} mm/sec gave 4% intergranular failure. Irving's data however predicted < 4% intergranular failure at crack velocities of 5×10^{-5} mm/sec and 35% intergranular failure at a velocity of 1.5×10^{-3} mm/sec.

This possibly suggests firstly that in an aqueous environment where hydrogen is more freely available, the range of crack velocities over which intergranular failure may occur is much lower than for those in a humid air environment. Secondly the hydrogen concentration required for the promotion of intergranular failure in this material is less than for the material Irving used and thus the corresponding crack tip velocity is reduced

Despite these inconsistencies these results show excellent agreement with Beachem's [27] model in that it predicted both the intergranular failure and the microvoid coalesence failure mode for the R=0.9 test. This once again points to the hydrogen assisted model since microvoids could not have been formed directly by anodic dissolution models.

For the 3 Hz test the short loading period was not enough to allow hydrogen to be transported to the grain boundaries. This prevented sufficient hydrogen build-up to cause large scale intergranular failure. However, sufficient hydrogen build-up did occur in a few isolated cases giving rise to isolated intergranular facets (Figure 5.54). The resulting slow crack growth rate does not supply sufficient bare metal for hydrogen production, thus hydrogen assiste cracking cannot take place. Initially hydrogen concentration at the crack tip and hydrogen transport to the region of maximum stress triaxiallity were the limiting factors. However as the crack growth rate increased hydrogen concentration at the crack tip no longer was a limiting factor. The faster loading rate did not allow sufficient time for hydrogen transport by dislocation motion. At longer crack lengths and large K levels large areas were then plastically deformed which activated the dislocation sweeping mechanism allowing a greater hydrogen build-up at inclusion sites. This then led to a change in fracture mode to microvoid coalescence (Figure 5.55).

In the case of the 0.3 Hz test the loading cycle was long enough to permit hydrogen diffusion combined with dislocation sweeping of hydrogen to the grain boundaries. The build-up of hydrogen at the grain boundaries led to hydrogen assisted cracking in the form of intergranular failure (Figure 5.56). This increased crack growth rate thus supplied more reactive surface area for the production of hydrogen thereby maintaining the increased crack growth rate. However, the crack velocity started to exceed the rate of hydrogen transport leading to a decrease in the hydrogen concentration at the crack tip and thus reduced intergranular failure occurs. The reversed plastic zone size then approached the prior austenite grain size and caused

transition from intergranular failure to ductile striated growth (Figure 5.59). This transition occurred at the knee of the crack growth curve (Figure 5.21) and from this point the crack propagated at a slower rate and thus allowed hydrogen build-up in the matrix until at some critical concentration combined with the large K value resulted in microvoid coalescence (Figure 5.62). This transition occurred at the second bend in the crack growth rate curve (Figure 5.21).

6.2 Variable Amplitude Loading

The Spectrum loading sequence suggested at the 1983 ICCGR meeting [63] was used in these tests in which the frequency was increased from 1 Hz to 3 Hz to give a much less time consuming experiment. To facilitate the interpretation of the results in terms of the effect of the various R-ratios on the overall crack growth rate three different loading sequences were designed viz. Ripples, Peaks and Trapezoidals (Figure 4.5). These loading sequences consisted of one or two of the R-ratios in the same proportion as used in the spectrum loading sequence.

6.2.1 Argon Tests

The crack growth rates after 500 blocks for Trapezoidal, Peaks and Spectrum loading sequences were greater than that found for the high R-ratio (Ripples) test. Thus since all these tests were conducted in the same environment the increased crack growth rates must be due to the load interaction effects. Also since increased crack growth rates were observed, little or no crack growth retardation could have occurred as a result of peak overloading. This was borne out by fractographic observations (Figures 5.63 - 5.70) which showed no plasticity effects i.e. increased striation spacing due to ov[illegible] McMillan and Pelloux [81] showed that althou[illegible]ccelerations or retardations of crack growth can ha[illegible]served from crack growth curves striations indeed can reve[illegible]uch effects.

The lack of retardation or delayed retardation of the fatigue crack growth, as well as the lack of fractographic evidence of this, is due to a number of factors. These will be discussed separately for each of the load sequences. For the Peaks loading sequence, several workers [45,47,78,82] have shown that longer crack growth delays are obtained by increasing the magnitude of the overload with large delays being recorded for peak loads which were 100 percent greater than the maximum load just prior to overload application. Despite the fact that the magnitude of the overload peaks used in the present study were 100 percent greater than the maximum load before overload application no retardation or delayed retardation of the fatigue crack growth was observed.

Both retardation and acceleration can be explained in terms of crack closure. Elber [53] pointed out that crack growth retardation did not occur immediately after an overload. The crack had to penetrate into the plastic zone created by the overload before crack closure could become effective (delayed retardation). Measurements of the crack opening stress, S_{op} (i.e., the stress at which crack closure is removed) showed that $S_{op} < S_{min}$ before the overload is applied [82] (Figure 6.8). Immediately after the overload, S_{op} is reduced still further. This would allow an accelerated growth for a small number of cycles, however, shortly afterwards, S_{op} is significantly raised to beyond S_{min}. Later, S_{op} again decreases and S_{eff} (S_{max} - S_{op}) increases, when $S_{op} = S_{min}$ the retardation of the crack growth has vanished.

It was also shown [82,83] that specimen thickness had an effect on the amount of delay in fatigue crack growth with longer delays being obtained for the thinner specimens. In both cases tests were done on specimens ranging from 2 - 10 mm in thickness with Schijve [78] measuring a 80% reduction in S_{op} with increase in thickness and Shih [83] measuring a 50% reduction in the number of cycles between the abnormally low rate of fatigue crack growth to the crack growth rate prevailing before the application of overload. This reduction in delay with thickness is thought to be due to the plastic zone size in the thicker

specimen being smaller (approximately plane strain) than in the thinner specimen (approximately plane stress). In the present study the specimens were 25 mm thick, thus the delay would be still further reduced, if not non-existent. Further, Rice and Stephens [47] showed that as the number of cycles between overloads were reduced so to did the amount of retardation. In the present study the number of cycles between each tensile overload was only 50, much less than the 1000 used by these workers [47].

Whereas tensile loads temporarily slow down the rate of crack growth or arrest altogether its advance, compressive overloads tend to accelerate crack growth [78,82]. Furthermore, if a tensile overload is followed immediately by a compressive overload, the beneficial effect of the tensile load may be significantly reduced [78,82]. Also low-high sequences cause an initial acceleration of the crack propagation at the high stress level which rapidly stabilizes [81]. The transient increase in crack growth rates associated with compressive overloads and low-high block loading sequences may be explained with the aid of the closure model. Here, during the first few cycles of the high load block or the compressive overload, the material experiences a low opening stress intensity level and hence a greater ΔK_{eff}. Once these large displacements begin to interfere in the wake of the crack front, the opening level begins to rise and eventually reaches its new equilibrium value. Indeed this is what happens in the case of the Trapezoidal loading sequence and leads to the faster observed and growth rates and explains the lack of fractographic evidence of plasticity effects.

All the above mentioned factors which explain the increased crack growth rates for the Peaks and Trapezoidal loading sequences also apply to the Spectrum loading sequences. This is once again confirmed by the fractography (Figures 5.74 - 5.76) which clearly show ductile striated growth without arrest marks at the overload positions. This is further supported by the fact that when the separate transient crack growth contributions are added together the sum agrees well with the measured crack extension of the spectrum loading (Table 5.1).

6.2.2 PWR Water Tests

The discussion on retardation and delayed retardation of the fatigue crack growth for the variable amplitud loading sequences in an argon environment also applies to the tests performed in PWR water. The increased crack growth rates for the different loading sequences when compared to the argon tests were due to the environmental effect. The different models for environmental assisted cracking discussed in the effect of PWR water environment on high R-ratio tests still applies to the variable loading sequences. Once again the greatest environmental effect was found at the lowest frequency, inasmuch that decreasing the frequency from 3 Hz to 0.3 Hz increased the measured crack extension from 2.56 to 3.36 mm.

he individual transient crack extension data when added together represent 2.05 mm of crack growth whereas the actual spectrum loadi crack growth was 2.56 mm. This difference can be explained by (a) crack extension in the spectrum loading test was much greater than that of the individual tests and hence there was a greater likelihood of the crack encountering more inclusion clusters and thereby creating the "right" crack tip chemistry thus generating a greater environmental component, (b) as a result of the larger crack length and hence ΔK range tested in the case of the spectrum loading test the individual contributions from each transient will be slightly more because growth rate is a function of ΔK level and (c) a synergistic effect resulting from the various mechanical loading conditions. The fact that the argon tests, which were essentially "non environmental" in nature, did not exhibit any synergistic mechanical effects suggests that the difference between the added transient growth contributions and the spectrum loading is probably a result of some combination of (a) and (b).

Fractographic evidence of the 0.3 Hz Spectrum loading specimens supported the above argument inasmuch that while the dominant fracture mode was ductile striated growth there was evidence of numerous flat featureless regions (Figures 5.78 - 5.80). In some cases these regions appeared to have been initiated from a large

carbide or more probably a non-metallic inclusion (Figures 5.79 & 5.80). The river type lines emanating from the initiation point suggested that a cleavage fracture started at this point and spread out toward the front and side of it. This can be explained in terms of Beachem's model where at intermediate ΔK levels quasi-cleavage was the prevalent hydrogen assisted fracture mode.

The crack growth rates obtained for the 3 Hz Peaks, Trapezoidal loading sequences showed good agreement with the 3 Hz R = 0.9 data while the Spectrum loading growth rate was about twice that of the 3 Hz R = 0.9 data. The crack growth rates obtained for the 0.3 Hz Spectrum loading sequence showed excellent agreement with the 0.3 Hz R = 0.9 crack growth curve (Figure 5.20). This increasing agreement between the R = 0.9 and the Spectrum loading with decreasing frequency indicates the increasing role played by the R = 0.9 growth rate component in the Spectrum loading crack growth rate behaviour.

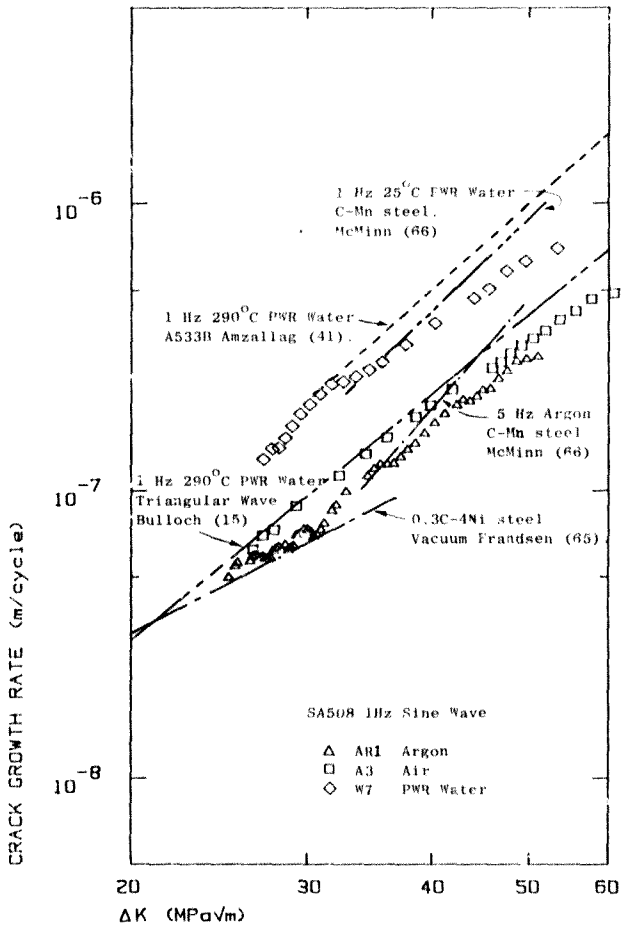

Figure 6.1: Effect of Environment using 1 Hz sine wave. Comparison of present data with other worker's data.

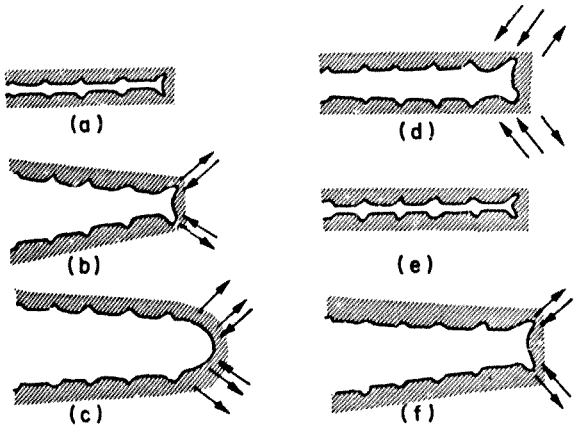

Figure 6.2: The plastic blunting process of fatigue crack propagation on the stage II mode: (a) zero load, (b) small tensile load, (c) maximum tensile load, (d) small compressive load, and (f) small tensile load. The double arrowheads in (c) and (d) signify the greater width of slip bands at the crack in these stages of the process. The stress axis is vertical. Laird [ ].

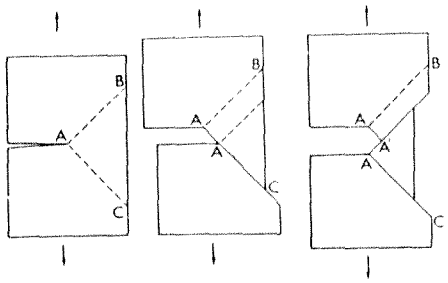

Figure 6.3: Crack extension by alternating shear in a singly grooved tensile specimen. Pelloux [83].

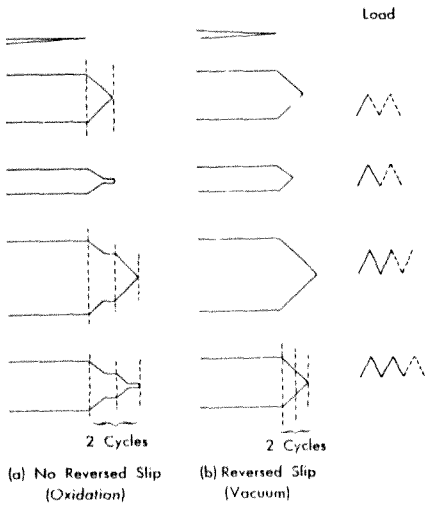

Figure 6.4: Model comparing crack tip extension after two load cycles in air and in vacuum. Pelloux [83].

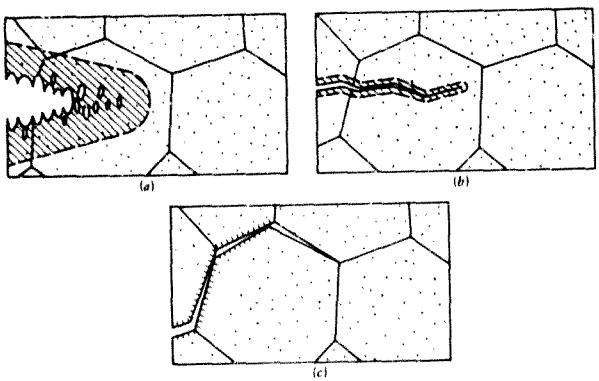

Figure 6.5: Schematic representation of different hydrogen induced fracture paths as a function of stress level.
(a) High K level generates microvoid coalescence;
(b) intermediate K level generates transgranular fracture by a quasi-cleavage mechanism; (c) low K level leads to intergranular fracture path. Beachem [27].

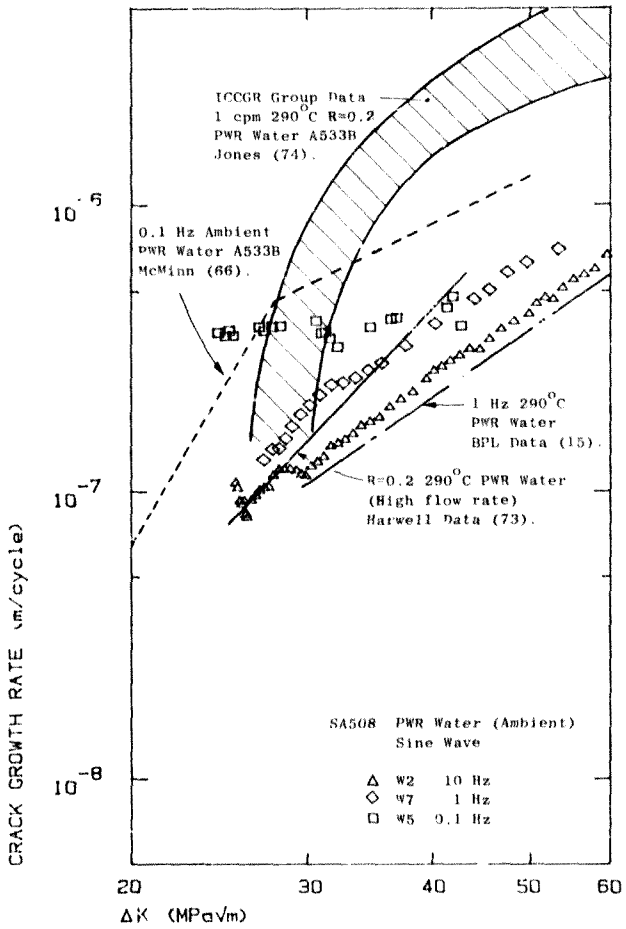

Figure 6.6: Effect of Frequency in PWR water. Comparison of present data with other worker's.

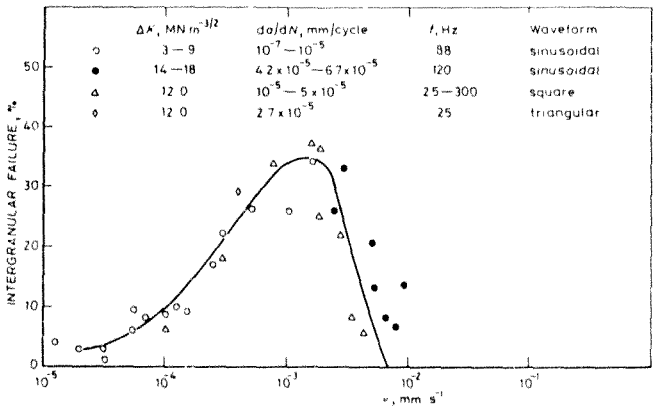

Figure 6.7: Effect of crack velocity on proportion of intergranular failure for SAE 4340 steel tempered at 200 C and tested in laboratory air at R = 0.35. Irving and Kurzfeld [68].

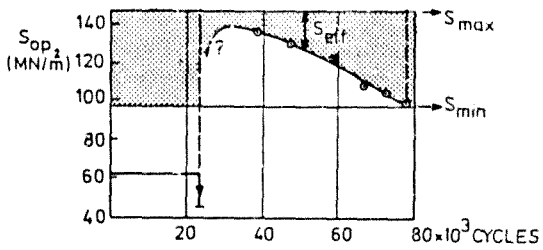

Figure 6.8: Crack opening stress before and during delay period. Schijve [89].

7 CONCLUSIONS

A series of tests were conducted on A508 cl III RPV steel to determine the effects of environment, frequency, waveform, and variable loading sequences on the fatigue crack growth behaviour. The following conclusions were arrived at:

7.1 Constant Amplitude Loading

7.1.1 Environment

(i) Striations were found in the fracture surfaces of specimens tested in argon.

(ii) These striations resulted from the fact that while 99.95% pure argon was used this represents a rather poor vacuum of 10^{-3} Torr thus sufficient active components may be present to form a monolayer of oxide (or indeed a monolayer of argon could be adsorbed onto the fracture surface).

(iii) The effect of an aqueous environment is directly related to the frequency of the test. The slower the frequency the greater the environmental effect.

(iv) The effect of the PWR water was to partially dissolve the MnS inclusions producing H_2S which retards the recombination of atomic hydrogen and thus hydrogen absorption into the metal is enhanced.

7.1.2 Frequency

(i) No effect of frequency was found in both air and argon environments for both waveforms tested.

(ii) The 1 Hz PWR water test showed some increase in crack growth rate compared to the 10 Hz PWR water test but no environmentally assisted crack (EAC) growth which agrees well with other reported data.

(iii) The 0.1 Hz PWR water test exhibited classic characteristic EAC growth i.e. plateau growth behaviour. This was manifested fractographically as intergranular failure.

(iv) The onset of plateau growth occurred at lower ΔK levels than similar ICCGR Round Robin data and was due to the preponderance of MnS inclusions encountered in the steel used for the present study.

(v) Plateau rates found in the present study were lower than those found in the ICCGR Round Robin data and this was attributed to the faster frequency (0.1 Hz as opposed to 1 cpm (0.01667 Hz)) used for this test and/or the lower temperature used (25°C as opposed to 290°C).

7.1.3 Waveform

(i) An accurate comparison of the various waveforms could not be made since the loading cycles of positive sawtooth and sine wave should be equal in rate and duration.

(ii) Positive sawtooth waveform consistently gave faster crack growth rates than sine wave although the amount varied depending on the environment and in some cases frequency.

(iii) The present study showed little effect of waveform and frequency in an argon environment.

(iv) The differences in crack growth rates observed in air and PWR water when compared to argon can best be explained in terms of the presence of a "hydrogen producing" species which caused embrittlement.

(v) In PWR water the increased crack growth rate of the 1 Hz test relative to the 10 Hz test was due to the fact that the longer loading time allowed dislocations to sweep hydrogen into the matrix thus increasing hydrogen transport rates to the region of greatest triaxial stress. This led to a larger environmental component for the positive sawtooth at a frequency of 1 Hz.

7.1.4 High R-Ratio Tests

(i) The present R = 0.9 argon data represents near-threshold growth rate and agrees well with the data reported.

(ii) The fracture mode for the argon data remained microstructure insensitive.

(iii) Crack growth rates in air were faster than those in argon and no evidence of closure induced fretting was found.

(iv) Once again the most significant environmental effect was found in PWR water at low frequency in which the environmental enhancement factor after 500 blocks for 0.3 Hz PWR water versus 3 Hz argon was 16.2 as opposed to the 10 Hz PWR water which was 3.3.

(v) The fracture mode for the 0.3 Hz test was microstructure sensitive (i.e. intergranular failure) also the transition from microstructure sensitive to microstructure insensitive occurred when the reversal plastic zone size was smaller (~5μm) than the prior austenite grain size (~17μm).

(vi) The crack velocities were below that predicted by Irving and Kurzfeld for the respective percentage of intergranular failure.

(vii) Two hydrogen assisted fracture modes as predicted by Beachem's model were found in the 0.3 Hz test viz. intergranular failure at low crack growth rates and

microvoid coalescence at high crack growth rates.

7.2 Variable Amplitude Loading

7.2.1 Argon Tests

(i) No fractographic evidence of retardation or delayed retardation of the fatigue crack growth was found.

(ii) The lack of retardation or delayed retardation was due to lack of closure effects due to high R-ratio testing, thickness effects and relative closeness of the subsequent overloads. This also led to faster growth rates.

(iii) Compressive overloads tend to accelerate crack growth due to the lower crack opening stress intensity of the compressive overload and hence a greater ΔK_{eff}. This led to greater crack growth rate for the Trapezoidal load sequence when compared to the Ripples load sequence.

(iv) The separate argon transient crack growth contributions, when added together, approximate the Spectrum crack extension very closely.

7.2.2 PWR Water Tests

(i) The increased crack growth rates for the different loading sequences when compared to the argon test was due to the environmental effect.

(ii) Once again the reduction of frequency caused the most significant environmental effect.

(iii) Fractographic examination of 0.3 Hz Spectrum test showed evidence of flat brittle fan-shapes which initiated from large carbides or inclusions.

(iv) Excellent agreement of the 0.3 Hz Spectrum data points with the 0.3 Hz R = 0.9 crack growth curve indicates that the R = 0.9 crack growth component of the Spectrum loading sequence plays a dominant role.

7.3 Mechanisms

(i) Hydrogen assisted cracking was shown to be the most acceptable model for explaining both the crack growth behaviour as well as the fractographic observations found in all the tests conducted in this study.

8 RECOMMENDATIONS

Phenomenological Aspects

The results obtained for corrosion fatigue crack growth rates in the present study show good agreement with other data reported in the literature. It is therefore suggested that further frequency tests be conducted at the frequency and temperature of most interest, viz., 1 cpm and 290°C respectively in PWR water.

To clarify the position with regard to waveforms further tests using sine, positive and negative sawtooth waveforms should be conducted being careful to keep the loading or unloading periods the same for all the waveforms.

A recent study was conducted to determine what accidental deteriorations of the high purity water used in reactors can occur and what effect these conditions had on the crack propagation. High chloride and oxygen levels were found to give greater crack growth rates. Since this further simulates realistic water chemistry conditions in reactors such worst case conditions should be investigated.

In view of the results obtained for the variable loading further work should be conducted with special reference to the effects of R-ratio, in the near threshold regime but spanning a larger ΔK range. Once again a decrease in frequency to 1 cpm and increase in temperature to 290°C should yield useful information.

Subsequent fractographical analysis should yield more information regarding the fracture mechanism/mechanisms.

Mechanistic Studies

Because of the complexity of the Spectrum loading sequence more work should be done to clarify the effect of single overloads and

underloads at high R-ratio in argon and aqueous environments.

Further contributions are still required to improve our understanding of the mechanism/s of environmentally assisted cracking. To this end a study should be made of the plastically deformed area ahead of the crack front once EAC growth has been achieved. This area should contain information regarding the operating mechanism.

Also the transition from microstructure sensitive to microstucture insensitive behaviour is thought to be due to the reversed plastic zone size being of the order of the prior austenite grain size. Thus measurements should be made of the plastic zone sizes of various crack lengths at the onset of EAC. This can be done by a recrystallization technique.

However, new areas of investigation could include a study of the crack growth retardation and/or crack closure phenomena. Also further knowledge of the hydrogen embrittlement mechanism could be obtained by conducting tests in various hydrogen containing or hydrogen producing environments. A fractographical study of the resulting fatigue fracture surfaces will greatly aid in the understanding of environmentally assisted crack growth and hopefully yield a working mechanistic rationale for such processes.

REFERENCES

1. P D HICKS "Corrosion Fatigue Studies on a Nuclear Pressure Vessel Steel in Simulated Pressurized Water Reactor Environments" An M.Sc. (Eng) dissertation at the University of the Witwatersrand, Johannesburg, South Africa, January 1985.

2. R O RITCHIE "Near Threshold Fatigue Crack Propagation in Steels" Int. Metals Review 1979.

3. P PARIS and F ERDOGAN "A critical analysis of Crack Propagation Laws" Journal of Basic Engineering, 1963.

4. J H BARSOM "Corrosion Fatigue Crack Propagation Below K_{Iscc}" Eng. Fracture Mechanics Vol. 3 1971.

5. J P GALLAGHER "Corrosion Fatigue Crack Growth rate Behaviour above and below K_{Iscc}" Journal of Matls Vol. 6 1971.

6. M O SPEIDEL et al. "Corrosion Fatigue and Stress Corrosion Crack growth in High Strength Aluminium alloys, Magnesium Alloys and Titanium alloys exposed to Aqueous Environments" Corrosion Fatigue-Chemistry, Mechanics and Microstructure, University of Connecticut (NACE) 1971.

7. D A MEYN. "An Analysis of Frequency and Amplitude Effects on Corrosion Fatigue Crack Propagation in Ti-8Al-1Mo-1V" Met. Trans. Vol. 2 1971.

8. I M AUSTEN and E F WALKER "Quantitative understanding of the Effects of Mechanical and Environmental variables on Corrosion Fatigue Crack Growth Behaviour" in Influence of Environment on Fatigue, Conf. Inst. Mech. Engrs. 1977.

9. G A MILLER, S J HUDAK and R P WEI "The Influence of Loading Variables on Environment Enhanced Fatigue Crack Growth in High Strength Steels." JTEVA Vol. 1 1973.

10. T D ATKINSON and T C LINDLEY "The Effect of Frequency and Temperature on Environmentally Assisted Fatigue Crack Growth Below K_{Iscc} in Steels" In Influence of Environment on Fatigue, Cont. Inst. Mech. Engrs. 1977.

11. D S KEMSLEY "The Fatigue Behaviour of an Ultra-High Strength Steel as Influenced by the Water Vapour Content and Temperature of an Air Environment" EFM Vol. 1978.

12. G C SALIVAR et al "Effect of Frequency and Environment on Fatigue Crack Propagation of SA533B-1 Steel" EFM Vol. 14 1981.

13. S SURESH and R O RITCHIE "On the Influence of Environment on the Load Ratio Dependence of Fatigue Thresholds in Pressure Vessel Steel" EFM Vol. 18 1983

14. T L GERBER, J D HEALD and E KISS "Fatigue Crack Growth in SA508-CL2 steel in the high temperature, High Purity Water Environment" Journal Eng. Mat. Tech. 1974

15. J H BULLOCH and I. W BUCHANAN "Fatigue Crack Growth Behaviour of A533B Steel in Simulated P W R Water" Corrosion Science Vol. 24 1984.

16. G CABETTA "A Method of measuring Electrochemical Potential at the Tip of a Growing Crack during an Environmental Fatigue Test". Fatigue of Eng. Matls and Structures Vol. 5 1982.

17. J DUFRESNE and J B RIEUNIER "Probablistic Evaluation of Fatigue Crack Growth in SA508 and SA533 B Steel" Pressure Vessel and Piping Division of ASME.

18. F P FORD "Mechanisms of Environmental Cracking Systems Peculiar to the Power Industry" General Electric co. Research Project No. 1332-1 Sept. 1982.

19. P DOIG and P E J FLEWITT "Mechanisms and Fractography of Environmentally Assisted Cracking in Electrical Power Generating Plant Components" Central Electricity Generating Board. U K

20. K KLEMETTI et al "On the Role of Inclusions in Environment sensitive cracking of Reactor Pressure Vessel Steels" Int. Symposium on Environmental Degradation of Materials in Nuclear Power Systems. Myrtle Beach U S A 1983.

21. K TORRENEN et al "Proceedings of I A E A. Specialists Meeting on Subcritical Crack Growth" Frieburg 1981.

22. K TORRENEN and M KEMPPAINEN "A Fractographic study of the effects of varying dissolved oxygen level on the Cyclic Crack Growth of SA533 B Steel in High Temperature Reactor Grade Water" Technical Research Centre, Finland. 1981.

23. B D CRAIG "A Fracture Topographical Feature Characteristic of Hydrogen Embrittlement" Corrosion NACE 1981.

24. G WRANGLEN "Electrochemical Properties of Sulphides in Steels and the Role of Sulphides in the Inhibition of Corrosion" Poc. Int. Symp. Sulphide Inclusions in Steels, New York 1974.

25. A D WILSON "Fatigue Crack Propagation in SA533 B Steels" ASME Trans. J Pressure Vessel Tech. 1977.

26. W H BAMFORD, D M MOON and L J CESCHINI "Environmentally Assisted Crack Growth in Light Water Reactor Materials" Annual Technical Progress Report Fiscal Year 1981. Westinghouse Electric Corporation.

27. C D BEACHEM "A New Model of Hydrogen Assisted Cracking (Hydrogen Embrittlement)" Metallurgical Transactions. February, 1972.

28. O VOSIKOVISKY "Frequency, Stress Ratio and Potential Effects on Fatigue Crack Growth of HY 130 steel in Salt Water" JTEVA Vol. 6 1978.

29. B F JONES "The Influence of Environment and Stress Ratio on the low Frequency Fatigue Crack Growth Behaviour of two medium-strength Quenched and Tempered steels". Int Journal Fatigue Vol. 6 1984.

30. W H BAMFORD "The Effect of Pressurized Water Reactor Environment on Fatigue Crack Propagation of Pressure Vessel Steels" in Influence of Environment on Fatigue, Conf. Inst. Mech. Engrs. 1977.

31. T YOKOBORI and K SATO "The Effect of Frequency on Fatigue Crack Propagation rate and Striation spacing in 2024-73 Aluminium Alloy and SM-50 steel. EFM Vol. 8 1976.

32. L A JAMES "The Effect of Frequency upon Fatigue Crack Growth of Type 304 Stainless Steel at 1000'F" ASTM STP 513 1972.

33. W H BAMFORD "Application of Corrosion Fatigue Crack Growth Rate Data to Integrity analyses of Nuclear Reactor Vessels" Jnl Eng. Matls. and Tech. Vol. 101 1979.

34. P C PARIS et al. "An Extensive Study on Low Fatigue Crack Growth Rates in A533 and A508 Steels " ASTM STP 513 1971.

35. J M BARSOM "Fatigue Behaviour of Pressure Vessel Steels" Welding Research Council Bulletin 194 1974.

36. BUCCI and DONALD "Fatigue and Fracture Investigation of a 200-grade Maraging Steel Forging" Del Research Corp. Report, Hellertown Pa. 1972.

37. S T ROLFE and J M BARSOM "Fracture and Fatigue Control in Structures. Applications of Fracture Mechanics" Prentice - Hall 1977

38. R P WEI and J D LANDES "Correlation Between Sustained-Load and Fatigue Crack Growth in High Strength Steels" *Materials Research and Standards* MTRSA, 9, No. 7, 1969.

39. J M BARSOM "Effect of Cyclic Stress Form on Corrosion Fatigue Crack Propagation Below K_{Iscc} in a High Yield Strength Steel." *Corrosion Fatigue* NACE -2 Connecticut 1971.

40. T KAWAKULBO et al "Crack Growth Behaviour of Type 304 Stainless Steel in Oxygenated 290°C Pure Water under Low Frequency Cyclic Loading." *Corrosion* NACE 1980.

41. C AMZALLAG et al "Effect of Loading and Metallurgical Parameters on the Fatigue Crack Growth Rates of Pressure Vessel Steels in Pressurized Water Reactor Environment" *Int. Symp.* on Environmental Degradation of Materials on Nuclear Power Systems. Myrtle Beach, USA 1983.

42. R J SELINES and R M PELLOUX "Effect of Cyclic Stress Waveform on *Corrosion Fatigue* Crack Propagation in Al-Zn-Mg Alloys" Dept of Metallurgy and Material Science Report. Massachusetts Institute of Technology Cambridge Mass. 1972.

43. S J HUDAK and R P WEI" Comments on paper by J M Barsom Effect of Cyclic Stress form on Corrosion Fatigue Crack Below K_{Iscc} in a High Yield Strength Steel" corrosion Fatigue. NACE -2 Connecticut, 1971.

44. T V VENKALASUBRAMANIAM and T J BAKER "The Role of Non-Metallic Inclusions in Hydrogen Assisted Cracking of Steel".

45. R E JONES "Fatigue Crack Growth Retardation after Single Cycle Peak Overload in Ti-6Al-4V Titanium Alloys" EFM 1973.

46. S MATSUOKA and K TANAKA "Delayed Retardation Phenomena of Fatigue Crack Growth Resulting from a Single Application of Overload" EFM 1978.

47. R C RICE and R J STEPHENS "Overload Effects on Subcritical Crack Growth in Austenitic Manganese Steel" ASTM STP 536 1972.

48. V W TREBULES et at. "Effect of Multiple Overloads on Fatigue Crack Propagation in 2024-T3 Aluminium Alloy" ASTM STP 536 1972.

49. D N CORBLY and PACKMAN "On the influence of single and multiple Peak Overloads on Fatigue Crack Propagation in 7075-T6511 Aluminium" EFM 1973.

50. S MATSUOKA et al "The Retardation Phenomenon of Fatigue Crack Growth in HT 80 Steel" EFM 1976.

51. F H GARDNER and R I STEPHENS "Subcritical Crack Growth under single and multiple Periodic Overloads in Cold Rolled Steel" ASTM STP 559 1974.

52. O E WHEELER "Spectrum Loading and Crack Growth" Jnl. Basic Engineering 1972.

53. W ELBER "The Significance of Fatigue Crack Closure" ASTM STP 486 1970.

54. S SURESH, G F ZAMISKI and R O RITCHIE "Metallurgical Transactions A" 1981.

55. N J I ADAMS. "Fatigue Crack Closure at Positive Stresses" EFM 1972.

56. J SCHIJVE "The Effect of Prestrain on Fatigue Crack Growth and Crack Closure" EFM 1976.

57. V BACHMANN and D MUNZ "Fatigue Crack Closure Evaluation with the Potential Method" EFM 1979.

58. D GAN and J WEERTMAN "Fatigue Crack Closure after Overload" EFM Vol. 18 198..

59. D GAN and J WEERTMAN "Crack Closure and Crack Propagation rates in 7050 Aluminium" EFM 1981.

60. R A SCHMIDT and P C PARIS "Threshold for Fatigue Crack Propagation and the Effects of Load Ratio and Frequency" ASTM STP 536 1972.

61. R O RITCHIE "Fatigue Crack Growth: Mechanics and Fatigue Mechanisms" "Encyclopedia of Materials Science and Engineering" Pergamon Press 1983

62. H H JOHNSON "Calibrating the Electric Potential Method for Studying Slow Crack Growth" Materials Research and Standards. September 1965.

63. P M SCOTT "Proposed High Frequency Spectrum Load Experiment" ICCGR Meeting Schenectrady NY October 1983.

64. J H BULLOCH and L W BUCHANAN "The Influence of Environment and Temperature on the Fatigue Crack Growth Behaviour of a Pressure Vessel Steel" to be published in Res Mechanica.

65. J D FRANDSEN and H L MARCUS "Correlation between graph size and plastic zone size for Environmental Hydrogen Assisted Fatigue Crack Propagation" Scripta Metallurgica Vol 9 1975.

66. McMINN "Corrosion Fatigue Studies on SA533 B, C-Mn and Ducol W 30 pressure vessel steels at ambient temperature and pressure in aqueous environments" UKAEA Report ND-R-435 (3) June, 1981.

67. C LAIRD "The Influence of Metallurgical Structure on the Mechanisms of Fatigue Crack Propagation" ASTM STP 415 1967.

68. R W HERTZBERG " Fatigue Fracture Surface Appearance" ASTM STP 415 1967.

69. R M N PELLOUX "Mechanisms of Formation of Ductile Fatigue Striations" Transactions of the ASM 1969.

70. D A MEYN Transactions of the ASM 1968.

71. J LANKFORD and D L DAVIDSON "Fatigue Crack Micromechanisms in Ingot and Powder Metallurgy 7XXX Aluminium Alloys in Air and Vacuum" Acta Metall. Vol 31, No. 8.

72. J M KENDALL and J F KNOTT "Near-Threshold fatigue Crack Growth in Air and Vacuum". Basic Questions in Fatigue Proc. ASTM-NBS International Workshop & Symposium, October 1984.

73. P M SCOTT and A E TRUSWELL "The Influence of Water chemistry on Fatigue Crack Propagation in LWR Pressure Vessel Steels". UKAEA Report, AERE-R-10201, June 1981.

74. R L JONES "Recent Advances in Corrosion-Assisted Crack Growth Research" SMIRT Post-Conference Seminar California, 1983

75. J H BULLOCH Private Communication.

76. R J COOKE et al "The Slow Fatigue Crack Growth and Threshold Behaviour of a Medium Carbon Alloy Steel in Air and Vacuum" Eng. Fracture Mechanics Vol 7 1975.

77. J H BULLOCH Ph D Thesis University of Strathclyde 1980.

78. R W HERTZBERG "Deformation and Fracture Mechanics of Engineering Materials John Wiley 1983.

79. P E IRVING and A KURZELD "Measurements of Intergranular Failure produced during Fatigue Crack Growth in Quenched and Tempered Steels" Metals Science, 1978.

80. J R RICE and JOHNSON "Inelastic behaviour of Solids" 1970 New York (McGraw - Hill).

81. J C McMILLAN and R M N PELLOUX "Fatigue Crack Propagation under Program and Random Loads" ASTM STP 415 1965.

82. J SCHIJVE "Observation on the Production of Fatigue Crack Growth Propagation Under Variable Amplitude Loading" ASTM STP 595 1976.

83. T T SHIH and R P WEI "Effect of Specimen Thickness on Delay in Fatigue Crack Growth" JTEVA 1975.

APPENDIX

COMPUTER PROGRAMMES FOR FATIGUE TESTING AND DATA REDUCTIONS

Programme for low frequency testing

```
[illegible]

[illegible]

 [illegible]
 REM [illegible] FUNCTIONS
 PI = 3.14159265#
 DEF FNCOS(X)=COS(X)+EXP(X)
 DEF FNSIN(X)=SIN(X)+EXP(X)
 DEF FNLOG(X)=LOG(X+SQR(X*X+1))
 [illegible]
 ON ERROR GOTO 60000 :REM INITIALISE ERROR ROUTINE
 ON KEY(8) GOSUB 62000 :REM SET OUTPUT TO LPT1
 INPUT"TEST DESCRIPTION ";TD$:LPRINT TD$
 INPUT"TEST DATE AND TIME ";X$
 DIM A(1000)
 FOR I=0 TO 600
 A(I)=0.4
 IF INKEY$="" THEN [illegible]
 CLS
 INPUT "FILENAME FOR Data";FN$
 OPEN FN$,#1,0,0
 IF A(0)=19 THEN PRINT "Press Return to [illegible]
 FOR I=1 TO 2:PRINT #I,TD$:PRINT #I,TIME$:NEXT
 PRINT #4,"Max Load=";MX
 PRINT #4,"K Ratio=";KR
 PRINT #4,"STOP GROWING CRACK [illegible]
 PRINT #4,"NUMBER OF CYCLES RECORDED";I
 ON ERROR GOTO 0
 CLS:PRINT "FATIGUING PROCESS ";TD$:PRINT
 PRINT "        CONTROL USING MENU OR KEYBOARD ";
 IF CHR$(A(0))="S" THEN END
 IF CHR$(A(0))="I" THEN [illegible]
 IF CHR$(A(0))="D" THEN [illegible]
 IF A(0)=19 THEN [illegible]
 IF A(0)=0 THEN 360
 IF A(0)=1 THEN 360
 IF A(0)=2 THEN 360
 IF A(0)=3 THEN 360
 IF A(0)=4 THEN 360
 IF A(0)=5 THEN 360
 IF A(0)=6 THEN 360
 IF A(0)=7 THEN 360
 IF A(0)=8 THEN 360
 IF A(0)=9 THEN 360
 IF
```

```
[illegible]
[illegible]
[illegible]
```

Programme for positive *sawtooth* waveform

```
MASTER.BAS

READY.

 10 CLS:?
 11 REM FUNCTIONS ---------
 12 PI = 3.141592654
 13 DEF FNATN(X)=ATN(X/SQR(-X*X+1))+PI/2
 14 DEF FNEXP(X)=(EXP(X)+EXP(-X))/2
 15 DEF FNLOG(X)=LOG(X)/LOG(X*0+10)
 17 SP$="                                        "
 20 GOSUB 10000 :REM INITIALISE VARIABLES
 30 GOSUB 11000 :REM SET OUTPUT TO ZERO
 50 INPUT"TEST DESCRIPTION ( 25 CHARS.)";DE$:DE$=LEFT$(DE$+SP$,25)
 60 INPUT"TEST DATE  AND TIME :";X$
 100 GOSUB  1000
 110 GOSUB 600
 130 OPEN 4,4
 140 PRINT#4:IF DS<>0 THEN PRINT"  EXIT PRINTER ON LINE ":GOTO 140
 150 PRINT #
 160 INPUT " ( FILENAME FOR DATA";N$
 170 DOPEN#1,(N$),W
   IF DS<>0 THEN PRINT DS$:CLOSE 1:GOTO 160
 180 PRINT#4,CHR$(14);X$:PRINT#4,CHR$(14);X$
 190 PRINT#4:PRINT#4,"DATA STORED ON FILE ";N$
 195 PRINT#4,"MAX LOAD=";BIG
 200 PRINT#4,"R RATIO=";RAT
 205 PRINT#4,"STOP GROWING CRACK AT ";DELR;" MM"
 210 PRINT#4,"NUMBER OF CYCLES TO BUILD UP";CYCLES
 220 GOSUB 500
 270 PRINT "PAIRGUTING  PRESS 'S' TO STOP"
 280 GOTO ------ CONTROL USING MAIN GOTO NO. OF CYCLES
 300 IF ABS(DIG)    50 THEN ERR=1 : GOSUB 20000  :GOTO 1000 CHECK ERRORS
 302 IF ABS(MEAN)    1 THEN ERR=2 : GOSUB 20000
 303 IF ABS(FREQ)    10 THEN ERR=3 : GOSUB 20000
 315 IF  CYCLES<=1E380 OR CYCLES>0  THEN ERR=4
 320 IF  (FREQ=100 AND (RAT=.2  THEN GOTO 351
 330 IF  (FREQ=10) AND (RAT=.2  THEN GOTO 352
 340 IF  (FREQ=1) AND (RAT=.2  THEN GOTO 353
 350 IF  (FREQ=1) AND (RAT=.5  THEN GOTO 354
 351 D=.1 : GOTO 360
  352 D=.01 : GOTO 360
 353 D=.01 : GOTO 360
 354 D=.001 : GOTO 360
 360 LOW=BIG#RAT
 362 HI=BIG/50#.256
 363 LO=LOW/50#.256
 370 FOR  ---SAMPLING TO PMAX
 380 FOR L=0 TO HI : POKE 409+6,L
 390 GOSUB 4000
 400 GOTO 440
 410 REM     -CHANGE TO FAIRGUTOUR CURRENTURES
 420 GOSUB 670
 430 PRINT "PAIRGUTING  PRESS 'S' TO STOP"
 440 REM ---POSITIVE SAWTOOTH --       --
 450 NEXT
 460 L=LO : POKE 409+6,L
 470 FOR L=LO TO HI : POKE 409+6,L
```

```
480 FOR A = 1 TO 2:NEXT A:NEXT I
490 INPUT"HIT RETURN TO CONTINUE";A$
500 IF A$ = "S" THEN RESTORE:GOTO 430
520 GOSUB 5000
530 IF CU CYCLES THEN GOTO 450
535 PRINT "                "
536 PRINT "LL = "LL,"CU="CU:INPUT "ENTER NEW LOADING ";LL
537 IF A$="S" THEN GOTO 420
538 IF A$ = "N" THEN GOTO 536
540 GOTO 20000
550 CLOSE 1 :CLOSE 4
560 END
600 PRINT "
610 INPUT "MAX LOAD LEVEL  (1 TO 5)";LOADLEVEL
620 INPUT "R RATIO = ";RA
630 INPUT "FREQUENCY (HZ)..";HERTZ:HERTZ = HERTZ*10
640 CL = 0.0270*HERTZ :W=50:BW=25
650 INPUT "DISTANCE BETWEEN PEAKS IN MM. ";
660 INPUT "INITIAL CRACK LENGTH IN MM.";CO
670 INPUT "MAX NUMBER OF CYCLES..";CU
680 INPUT "NUMBER OF CYCLES BETWEEN CRACK LENGTH OUTPUT ";CU1
690 INPUT "AT WHAT CRACK LENGTH TO STOP (APPROX.) ";MLNG
710 RETURN
900 REM OUTPUT FILE -
910 MEAN=(HIG+LOW)/2
951 PRINT#4,"
953 PRINT#4," CYCLES         VOLTAGE          CRACK LENGTH"
954 PRINT#4,"                  HIGH                  HIGH"
955 PRINT#4,"
960 RETURN
  999 REM INITIALIZE FILE -
1010 PRINT"INITIALIZING FILE"
1020 OPEN10,10
1030 PRINT#10,"#  12"
1040 CLOSE10:RETURN
2000 REM   READ VOLTAGE FROM FILE AND CONVERT TO CRACK LENGTH
2010 RJ=FRE(0):OPEN 10,10
2013 CH=0
2015 FOR A=1 TO 5
2020 PRINT#10,"?"
2024 FOR B=1 TO 400:NEXT
2030 INPUT#10,CL$
2035 VV =VAL(CL$):IF  VV <0 THEN CH=VV
2037 NEXT
2040 IF CH=0 GOTO 2020
2050 IF B <0 THEN B=CH
2110 IF B=0  THEN GOSUB 4000
2120 PI=(2*W)/PI
2130 C=SIN(CH/(PI*B))/(2*W))
  40 C=SIN(CH/(PI*B))/(2*W))-(C^3/(3*(PI*B)^3))+(2*C^5/(5*(PI*B)^5))
2150 CL=CL*FNIC(C2/C3)
2160 CH=B  10
2170 PRINT "CRACK LENGTH";(INT(CL*100000))/100000
2180 PRINT "    MEAN LOAD=";MEAN
2190 PRINT "    NO. OF CYCLES RECORDED AND COMPLETED";CU:CYCLES=CU
2200 PRINT#1,CL;",";CU
2210 CH$=STR$(CH*1000):CH$=CH$(LEFT$(CH$,15-LEN(CH$))
2220 CL$=STR$((INT(CL*10000)-(10000)):CL$=CL$+LEFT$(SP$,15-LEN(CL$))
2230 PRINT#4,CU,CH$,CL$
2235 IF CH*1000> MLNG THEN GOTO 5%
2240 RETURN
```

```
 4000 REM GET INITIAL LOADING
 4005 RESTORE(0):OPEN #0,10
 4010 FOR J=1 TO 5
 4020 PRINTED10,"5"
 4021 FOR K=1 TO 400:NEXT
 4025 INPUTED10,D0$
 4030 Z=VAL(VAL(D0$)):D=Z-100*INT(Z/100)
 4040 NEXT
 4050 IF D0=1 THEN D=1:CLOSE #0:RETURN
10000 REM ~~~
```

Programme for spectrum loading

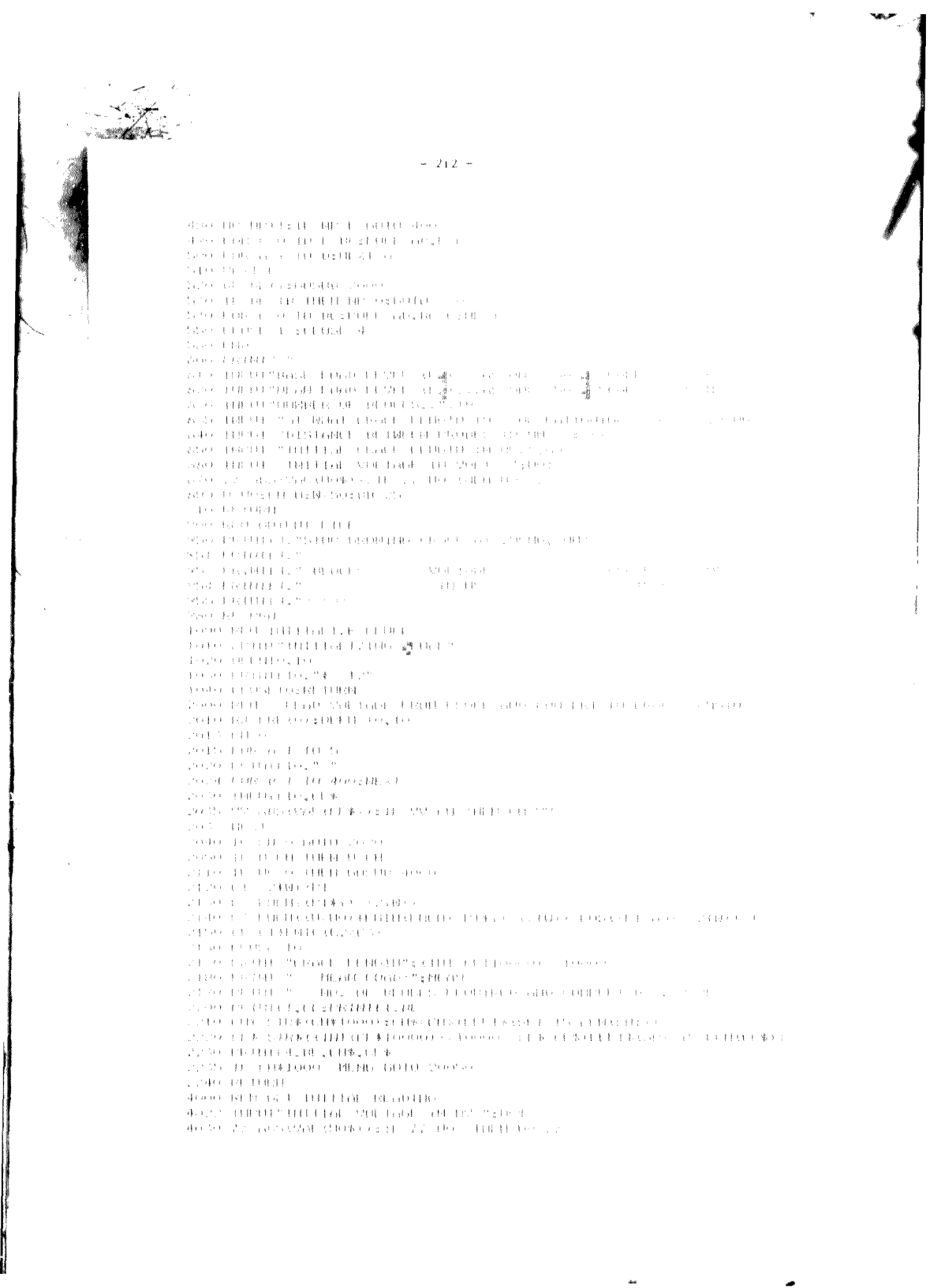

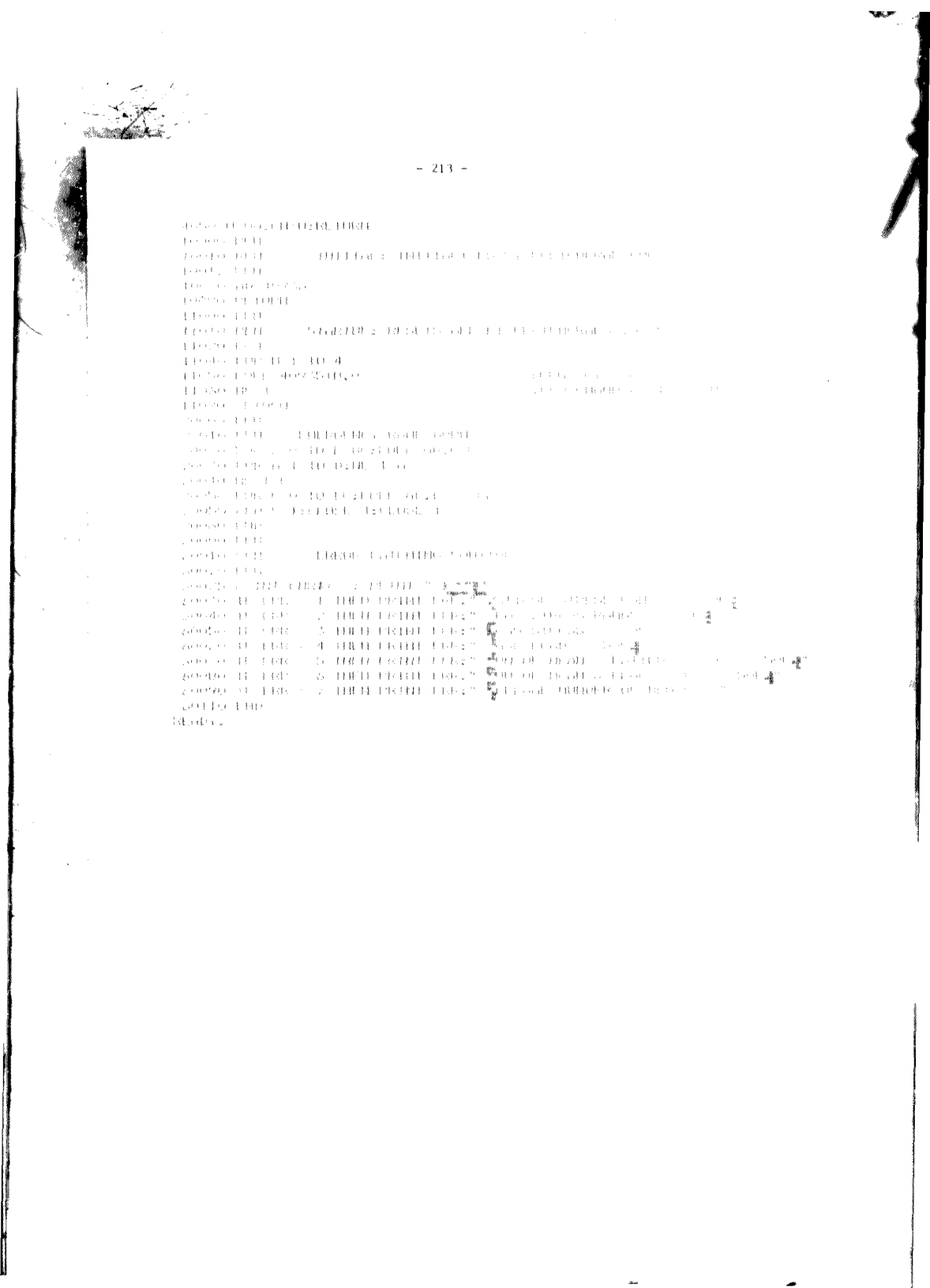

Programme for data reduction

```
[illegible]

[illegible]

 10 [illegible]
 11 [illegible]
 20 [illegible]"[illegible] [illegible] USES THE 2 POINT [illegible] [illegible] [illegible] [illegible] [illegible]"
 21 [illegible]"COMPUTE DO-D4 VELOCITIES [illegible] [illegible] [illegible] [illegible] [illegible]"
 22 [illegible]"[illegible] SPECIMEN."
 30 [illegible]"[illegible] [illegible] [illegible] [illegible] [
```

```
420 DIM
430 OPEN
440 CLS
450 LIST
460 '
470 '
480 '
490 '
500 '
510 '
520 '
530 '
540 '
550 '
560 '
570 '
580 '
590 '
600 '
610 '
620 '
630 '
640 '
650 '
660 '
2000 REM       READ DATA
2005 PRINT"":PRINT:PRINT
2010 INPUT "FILE NAME";NM$
2020 DOPEN#1,(NM$)
2030 INPUT#1,
2040 FOR I=1 TO 11
2050 INPUT#1,A(I):INPUT#1,
2060 NEXT I
2070 CLOSE 1
2080 PRINT"":PRINT    I "Data EDITED COMPLETE ! ";A(8);"
2090 GOTO 2
5000 REM                ROUTINE  TO Draw AXES
5010 X=4:GOSUB5000:X=
5020 GOSUB
5030 ST$="TH;SP1;":GOSUB1000
5040 ST$="SP"+STR$(XL)+","+STR$(YB)+","+ST$+","+STR$(YT)+","+STR$(YB)+";":GOSUB1000
5100 ST$="PD,":GOSUB1000
5110 ST$="PA,PD,"+STR$(XR)+","+ST$+STR$(YL)+";":GOSUB1000
5120 ST$="PA,PD,"+STR$(XR)+","+STR$(YB)+";":GOSUB1000
5130 ST$="PA,PD,"+STR$(XL)+","+STR$(YB)+";":GOSUB1000
5140 ST$="PA,PD,"+STR$(XR)+","+ST$+STR$(YH)+";":GOSUB1000
5150 ST$="PA,PD,"+STR$(XR)+","+STR$(YB)+";":GOSUB1000
5160 A=
5170 A=
5180 A=
5190 A=
```

```
5x200 FOR I=0 TO 4:GOSUB 1200
5x210 FOR I=1 TO 5:GOSUB 1300
5x220 FOR I=2 TO 6:GOSUB 1300
5x230 FOR I=3 TO 7:GOSUB 1300
5x240 SET "I=0":SET "I=1":SET "I=2":SET "I=3":SET "I=4":SET "I=5":SET "I=6":SET "I=7":SET "I=8":SET "I=9":SET "I=10":SET "I=11":SET "I=12":SET "I=13":SET "I=14":SET "I=15":SET "I=16":SET "I=17":SET "I=18":SET "I=19":SET "I=20":SET "I=21":SET "I=22":SET "I=23":SET "I=24":SET "I=25":SET "I=26":SET "I=27":SET "I=28":SET "I=29":SET "I=30":SET "I=31":SET "I=32":SET "I=33":SET "I=34":SET "I=35":SET "I=36":SET "I=37":SET "I=38":SET "I=39":SET
```

```
```

Author Achilles Roy Derrick
Name of thesis Corrosion Fatigue Crack Propagation In Pressure Vessel Steels. 1986

PUBLISHER:
University of the Witwatersrand, Johannesburg
©2013

LEGAL NOTICES:

Copyright Notice: All materials on the University of the Witwatersrand, Johannesburg Library website are protected by South African copyright law and may not be distributed, transmitted, displayed, or otherwise published in any format, without the prior written permission of the copyright owner.

Disclaimer and Terms of Use: Provided that you maintain all copyright and other notices contained therein, you may download material (one machine readable copy and one print copy per page) for your personal and/or educational non-commercial use only.

The University of the Witwatersrand, Johannesburg, is not responsible for any errors or omissions and excludes any and all liability for any errors in or omissions from the information on the Library website.